ON THE RESPONSE OF COMPOSITE-METAL HYBRID PANELS SUBJECTED TO HIGH PRESSURE SHOCK LOAD

By

Evan G. Patton

A DISSERTATION

Submitted to
Michigan State University
in partial fulfillment of the requirements
for the degree of

Mechanical Engineering – Doctor in Philosophy
Civil Engineering – Dual Major

2021

ABSTRACT

ON THE RESPONSE OF COMPOSITE-METAL HYBRID PANELS SUBJECTED TO HIGH PRESSURE SHOCK LOAD

By

Evan G. Patton

Structural light weighting is driving material innovation across automotive, defense and aerospace industries. In the case of defense and aerospace applications, structural lightweight materials increases the mobility of the military by allowing easier transportation to a particular destination as well as the transit around that destination. Integration of lightweight materials in the defense and aerospace industries requires the ballistic and blast capacities of a material to compete with traditional structural materials.

Fiber reinforced plastics have low density and high strength, which make them ideal structural light weighting materials. Under high strain rate loadings, complex damage mechanisms occur within the composite allowing for large amounts of energy absorption. However, these complex damage mechanisms can also lead to undesirable structural characteristics. To improve the overall design of traditional composites, attempts have been made to leverage the benefits of both composite materials and metal alloys, while minimizing the weaknesses of each constituent. By incorporating both composite and metal materials in a single hybrid system the collective blast capacity in a joint material system can be improved.

In this work, a free piston shock tube is tailored to create a quasi-Friedlander pressure form to simulate blast loading on a single interfaced, glass fiber reinforced thermoplastic composite metal hybrid panel. Damage and deflection characteristics are obtained for the hybrid material system. Damage is assessed by nondestructive evaluation (NDE) methods and dynamic deflection characteristics are obtained by an optical fringe projection method. Both damage and

deflection observations are then correlated to an LS Dyna multi-material model where further observations and insights are drawn about the behavior of composite metal hybrid panels.

ACKNOWLEDGMENTS

Graduate school has not been nearly how I initially expected it as a bright eyed and bushy tailed senior freshly graduating with my bachelors. The support system I've gotten from friends, family, and MSU faculty and staff has been amazing and I could not have done it without them.

I would like to first thank my parents for their continuous support throughout my undergraduate and graduate education and letting my venture on the career path that I love without judgment or challenge. I would like to thank my girlfriend Maddy, for being by my side throughout my entire tenure at Michigan State University. Having going through her Doctorate in Physical Therapy concurrently, she knew exactly how and when to give the support I needed. I would also like to thank my good friend and CVRC (Composite Vehicle Research Center) lab manager, Erik Stitt for guiding me in the right direction in my studies and career as I am following in his footsteps as we both complete our degrees. I would like to thank my committee members Dr. Robert Hart, Dr. Ricardo Mejia-Alvarez, Dr. Mahmood Haq, and Dr. Thomas Pence for their time and generous support. Dr. Hart provided me with the support, insight and guidance that was critical for my research to remain on track in a logical and concise manner. His time was invaluable and allowed me to graduate with the research, knowledge and tools, I am truly proud of, that will transcend into my career post graduation. Dr.'s Alvarez and Dr. Haq both provided me with the laboratory equipment, space and time to let my research really take off. Their hands off approach allowed space for me to grow as a better problem solver and engineer, but when I got stuck, they were there when I needed an extra push. I would like to note, this work and my graduate education would not be possible without the support from my SMART Scholarship sponsoring facility, US Army CCDC GVSC as they stimulated and encouraged my creativity on selecting a topic of interest of interest. Dan Schleh, Demetrios

Tezelopis, Andrew Smail, and many other research engineers at GVSC have all made huge impacts on the success in this research and my further education.

Dr. Katy Colby, Laura Post, and Jessica Pung worked wonders with providing the resources and administrative support ensuring a smooth transition from undergrad, to my masters, to my doctorate. The support system throughout my studies have been immense and I;ve developed a whole community of amazing people in my time here and I cannot possibly list all that helped me through. This last thank you is for all that have helped me through and given the support that I couldn't mention (You know who you are!) Lastly, Go green!

TABLE OF CONTENTS

LIST OF TABLES

LIST OF FIGURES

Chapter 1 Introduction

1.1 Introduction

The Oklahoma City, World Trade Center and Boston bombings are all examples of an unfortunate reality facing our nation. Terrorists, both domestic and international seek to cause mass destruction and harm through means of explosive events. However, catastrophic explosions are not limited to acts of terrorism. Accidental explosions are always an underlying concern in buildings dealing with manufacturing, power production, and other combustible consumer products. Flammable and compressed materials can be just as destructive as a deliberate act of terrorism. Most recently, in August of 2020 in the City of Beirut, Lebanon, nearly 2,700 tons of stored ammonium nitrate was unintentionally detonated resulting in a massive explosion claiming at least 220 lives [1]. The explosion was a clear example of how energetic materials can unexpectedly cause catastrophic destruction. Realizing the risks associated with manufacturing, production of consumer products and power generation, highly engineered facilities and armor systems are needed to protect the structure in which these energetic events are housed in, as well as protecting the surrounding areas.

Commonly, civilian structures are fortified with reinforced concrete and metal walls. Heavy blast resistant designs lead to massive supporting foundations and marvel construction feats to support the weight of the structures. The challenges in engineering blast resilient structures are even more amplified in automotive applications, such as military ground vehicles where being lightweight is vital in the effectivity of the vehicle system.

Historically, military vehicles have been fortified with thick slabs of aluminum, steel and even titanium. With growing lethality of energetic devices, increased demand in the performance of armor is needed to withstand the event. Unfortunately, this is commonly approached by simply increasing the thickness of the material originally being used. This not only comes with increased to weight but also decreased mobility. With futuristic warfare demanding highly mobile land systems, these vehicles must be designed with the concept of structural light weighting. Although engineers cannot readily prevent blast events from occurring, they can mitigate the effects of the blast event and reduce the risk and severity of injuries to the occupants. Understanding the kinematics of an explosion and the potential blast resistance and response of a building or vehicle structure, engineers can better design for these potential catastrophes and save lives.

Light weight structural materials are highly desired in automotive, aerospace, and military applications. In the case of defense applications, structural lightweight materials must maintain ballistic and blast capacities of traditional armor solutions at overall lower mass. A lighter vehicle fleet increases the mobility of the military by allowing easier transportation to a particular destination as well as the transit around that destination. Fiber reinforced plastics have low density and high strength, which make them ideal structural light weighting materials. However, the inherent multi-phase nature of the fiber-matrix construction results in more complex damage mechanisms than traditional armor metal alloys. To improve the overall design, attempts have been made to leverage the benefits of both composite materials and metal alloys, while minimizing the weaknesses of each constituent. By incorporating both composite and metal materials in a single hybrid system the collective blast capacity in a joint material system can be improved. Fiber metal laminates, or FML’s are examples of a composite system designed to exploit the advantages of both constituent materials.

Fiber metal laminates are a composite system that typically contain a fiber reinforced polymer (FRP) and metal alternating in a laminated stack. The FML exploits the high stiffness and ductility of metal materials with the higher ultimate strength and low density of an FRP to produce a high performance structural composite system that is optimally balanced for light weight strength. By understanding blast kinematics and how each material system interacts, engineers can exploit each materials inherent blast behavior and characteristics together in a composite system and develop an optimally designed structure that is light weight and practically thick while maintaining or exceeding blast resistance of a traditional monolithic plate of aluminum.

Preliminary research has shown fiber metal laminates increase blast resistance of a composite [2]–[4]. Furthermore, blast resistance thresholding was benchmarked by varying composition and thicknesses of the constituent materials [5]. The scope of this research sought to analyze the fiber metal laminate but at a single ply level (one interface) to investigate the fundamentals of how these materials interact with each other under blast loading and the effects on damage and deflections both permanent and dynamic. Finite element simulations were created to validate the experimental findings and help portray the dynamic events.

1.2 Literature Review

1.2.1 What is a Composite?

A composite utilizes and exploits properties of more than one type of material to enhance a certain behavior of a single bulk material system. Composites have been engineered to improve mechanical, electrical and chemical properties by tailoring their respective system. Examples include enhancing strength, thermal conductivity, or inhibiting electrical conductivity [6]. In the general case of a structural composite, reinforcing fibers or particles are added to a supporting matrix structure. The result is a light weight material system that is competitive with a traditional homogenous material [7]. The reinforcing fibers are extremely tailorable to a composite system. Fiber functions and properties are seemingly limitless as fibers can be utilized for their electrical and thermal conductivity, strength characteristics, and more [8], [9].

Although a matrix can be made of a variety of materials both organic and inorganic, the most widely used are organic polymer matrices [10]. A polymer matrix is composed of polymer macromolecules consisting of carbon, hydrogen, oxygen, and nitrogen atoms. These polymer chains vary in composition and directly affect the materials mechanical and chemical properties. The chemical composition of a polymer chain defines how the material concatenates. Most commonly, polymeric structures concatenate by becoming branched or crosslinked [11].

1.2.2 Thermoplastic Resin Vs. Thermoset Resin

Polymer matrices can be split into two characterizations, a thermoplastic, and a thermoset. A thermoplastic material has a melting point at which the material's intermolecular bonding weakens and allows it to become a viscous fluid that readily flows until the temperature drops below the melting point and the intermolecular forces strengthen. This is advantageous as it allows a thermoplastic to be formed, reheated, and cooled in a streamlined process. The result is a recyclable material system that is easily manufactured [12].

Thermoplastics can be broken into two general categories, semicrystalline and amorphous. Semicrystalline polymers have high orders of crystalline microstructure leading to a more ridged and brittle thermoplastic. Semicrystalline polymers have a very definite melting point where they abruptly become liquid. Examples of semi crystalline polymers are PPS, PEEK, PEK, and TPI. Contrarily, an amorphous thermoplastic is just the opposite. Amorphous material has a low order of microstructure and thus, leads to an elastic and ductile thermoplastic. These thermoplastics have an obscure melting temperature and tend to melt over a series of glass transition phases. A glass transition phase is when a polymer becomes soft and flexible rather than a viscous liquid. During the glass transition phase, the microstructure has changed, but the material has not melted and undergone a complete phase change. Examples of an amorphous material are polycarbonate, PETG, and ABS.

The polymer's organic composition defines whether the thermoplastic behaves crystalline or amorphous. However, a thermoplastic can be either amorphous or crystalline depending on its cooling cycle during the manufacturing process. If a thermoplastic polymer is heated and held above its glass transition temperature and not cooled quickly, its degree of crystallinity increases as its polymer chains have more time to flow into an ordered structure. The degree of crystallinity drastically effects the mechanical properties of the thermoplastic. Studies have shown that mechanical properties (strength/stiffness) increase with increasing degrees of crystallization [13], [14].

Thermoplastics are prone to organic solvent degradation [15]. This is one method of how a composite can become recyclable. Alternatively, it can also degrade the composite when organic solvents are used (I.e., brake cleaners and other automotive solvents). Usage in settings where heavy degreasing solvents are used, design considerations must be followed to determine if a certain thermoplastic is suitable for the application.

On the other hand, a thermoset develops a permanent chemical bond when cured. This chemical bond is irreversible and thus, the material cannot melt and be reformed or recycled without destroying the system [16]. Thermoset resin composites typically, but are not limited to, two-part epoxy systems composed of a rein identified as part A and a hardener identified as part B. These two parts are kept separate until mixing for application. Different mixing ratios of parts A and B are combined to initiate the hardening sequence. Thermoset's curing can also be catalyzed by simple heating, moisture addition, or UV light to trigger a chemical reaction to begin the hardening process. Cure times vary with organic compositions but behave similarly in their strength gain vs cure time history (Figure 1). Generally, epoxy's strength gains are logarithmic with quick initial strength gains followed by marginal gains for longer periods of time. This is expected as the thermoset's polymer structure is disordered and more easily arranged until the cure schedule starts to create more order in the microstructure making it more difficult to crosslink the polymer chains.

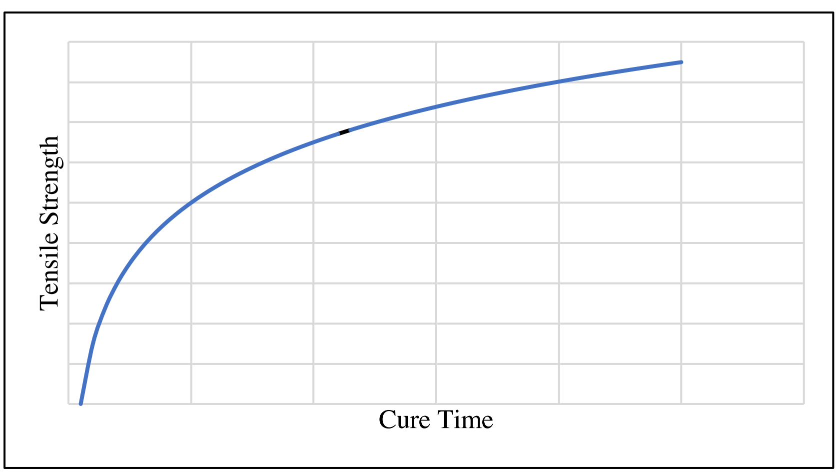

Figure 1 Epoxy Resin Curing Schedule

1.2.3 Thermoplastic Composites Vs. Thermoset Composites

When the polymer matrix is combined with a reinforcing material, the resulting material system now is classified as a composite. Thermoplastic and thermoset composites behave differently in their chemical, mechanical and manufacturing properties. Nishida et al. [17] drew comparisons of thermoset and thermoplastic resins using the same carbon fiber plain weave fabric at similar volume fractions. From the study, the authors found that thermoplastics and thermosets behave somewhat similarly in interfacial shear strength and quasi-static tensile properties, however, thermoplastics outperformed thermosets with both mode 1 and 2 inter-lamina fracture toughness as well as interlaminar shear strength and Izod impact strength.

Dry fabric for both thermoset and thermoplastic composites can be infused with resin via VARTM (Vacuum assisted resin transport method). A VARTM system is composed of a sequence of impermeable and permeable layers to create a vacuum bag around a formed shape of dry resin. Bleeder cloth is placed strategically around the dry fabric to ensure efficient and even resin distribution and impregnation. Vacuum air line is set up in at least two locations on either side of the part. Vacuum is then pulled on the composite sample causing consolidation of the dry fabric. Resin is then pulled through one airline and transfers into the composite. Excess resin is then pulled out of the system and into the specialized composite vacuum. The composite can then be autoclaved to reach an even higher degree of consolidating or left at atmospheric pressure at their hardening temperature designated by their respective resin system. For a thermoset resin, this process must be completed by the beginning stages of the chemical reaction. For a thermoplastic resin, this process can be completed in any length of time if the holding temperature of the resin and composite mold system remains above the melting point.

For relatively flat composite plates, both pre-impregnated thermoset and thermoplastic composites can be placed under a temperature hydraulic press to reach high levels of consolidation and superiorly flat surface finishes. The hydraulic press can generate consolidation pressures much higher than that of an autoclave.

However, means of manufacturing that set these apart is a thermoset resin more easily applied at room temperature as the polymer matrix is viscous until cured. This allows fabric to be saturated and formed into a given shape. This process is time consuming as each layer of fabric needs to be arranged in its final spot and consolidated for the length of the epoxy cure which is quite long for high performance epoxies. Furthermore, as soon as the reactive part A and B are mixed, the chemical reaction begins, and the thermoset must be applied before reaching a gel time where the matrix material is too far in the chemical reaction to apply confidently to gain full strength. Comparatively, a thermoplastic can remain liquid for a controlled amount of time without the risk of the resin prematurely hardening since the curing phase can be directly controlled. This process is typically quicker as the cooling schedule of most thermoplastics is shorter than the curing schedule of thermoset resins.

1.2.4 Aluminum Grades and Tempers

Looking at the other constituent of an FML, aluminum is one of the most widely utilized metals known for having relatively low density and high strength properties at a reasonable cost. Aluminum alloys vary widely in composition with the ability to add any nearly metallic element on the periodic table. All certified metal alloys have a code in the form of "XXXX-XXX", the first four digits denoting its chemical composition and the following digits (1 to 3) indicate the temper of the aluminum.

1.2.5 Composition Nomenclature

The first digit in the 4-digit (Xxxx) series indicates the alloy group. The second digit (xXxx) indicates the modification number of the specific series. I.E 2024 has no pervious modifications, where 5183 is the first modification of the series. Lastly, the last two digits (xxXX) are identifications to different alloys within the group [18].

Table 1 Aluminum Alloy (Xxxx) Code Designation [19]

Alloy Series	Main elemental contribution
1000 Series	99% or higher aluminum content
2000 Series	Copper
3000 Series	Manganese
4000 Series	Silicon
5000 Series	Magnesium
6000 Series	Magnesium and Silicon
7000 Series	Zinc
8000 Series	Other

1.2.6 Aluminum Tempers

The temper of an aluminum alloy is indicated after the 4-digit alloy designation. A temper code can be indicated with between 1 to 3 characters. The first character (Xxx) is the temper designation. The last two digits (xXX) are indications of miscellaneous things depending on the initial temper code character (Xxx). Codes F, O and W are typically used alone and are not followed by any further characters. Table 1 demonstrates temper designation for the first character in the temper code. For H series and T series temper codes reference (Tables 26, 27 and 28 in appendix)

1.2.7 Temper, Grades, and Blast

Studies have shown the effects of different aluminum alloys in response to blast[3]. Vo et. al. showed that in a fiber metal laminate system, the role of the aluminum temper and grade strongly effected the materials performance under blast. The findings showed that 7000 (7075) series performed the best when compared to both 2000 (2024) and 6000 (6061) series. Within the study a comparison between tempers was made as well. Aluminum 2024-O and 2024-T3 were both tested and compared. The O grade performing much worse in terms of deflection when compared to that of the T3 temper.

Table 2 Aluminum Alloy (xxxx-XX) Designation Code [18]

Temper designation	Temper process
F	"As fabricated"
O	Annealed
H	Strain Hardened
W	Solution Heat-Treated
T	Thermally Treated

1.2.8 Fiber Metal Laminates

Fiber metal laminates (FML) are a composite system that typically contain a fiber reinforced polymer (FRP) and metal, namely aluminum sheets alternating in a laminated stack. The FML exploits the high stiffness and ductility of metal with the ultimate strength and low density of an FRP to produce a high performance structural composite system that is optimally balanced for light weight strength.

FML's have been traced back to 1947 as a type of Aramid Reinforced Aluminum Laminate (ARALL) for the use in fighter jets in efforts to reduce weight. In 1987, Glass Laminate Aluminum Reinforced Epoxy (GLARE®) was invented. However, it wasn't until 1995 when this material was extensively studied for its blast resistance [20]. In 1988, Pan Am flight 103 exploded via suitcase bomb claiming the lives of 270 people launching an investigation on how to prevent further bombings. The investigation sparked the utilization of FML's in many modern aircraft.

1.2.9 FML Manufacturing

Fiber metal laminate panels come in a variety of stack up heights and orientations suited for fatigue, strength, and impact. Most commonly, GLARE® is composed of 2024-T3 aluminum and an epoxy-glass fiber composite system. Manufacturing specifics are proprietary, but it is known there is no adhesive interface. The aluminum is degreased, pickled, anodized and primed for bonding [21].

Joining dissimilar materials poses a challenge for composite integration in metallic structural systems. To bond the aluminum to the thermoplastic/thermoset composites the aluminum extensive focus must be address to the aluminum surface to better prepare for mechanical and chemical bonding. Cantwell et al. found that when using a thin polypropylene film at the interface of 2024-T3 aluminum and a polypropylene glass fiber composite, the fracture energy at the interface was higher than the interlaminar strength of the polypropylene [22]. The thin film of modified polypropylene (Fusabond M613-05) was hot pressed into an aluminum surface that was prepped with a proprietary amorphous chromate coating.

1.2.10 Blast Kinematics

Understanding blast kinematics is an important aspect when designing experimental procedures for study. Knowing how blast waves load and propagate through an object is crucial on how to design for blast. Explosive events can be categorized into major categories such as high explosives (HE), vapor cloud, pressure vessel, dust, and steam explosions [23]. Each of these explosive events have release their energies differently and should be designed for accordingly.

Furthering the considerations to be made before designing a structure, side effects from blast must mitigated in the final constructed build. These are, and not limited to, fragmentation, cratering, ground shock, and thermal flashes (Figure 2).

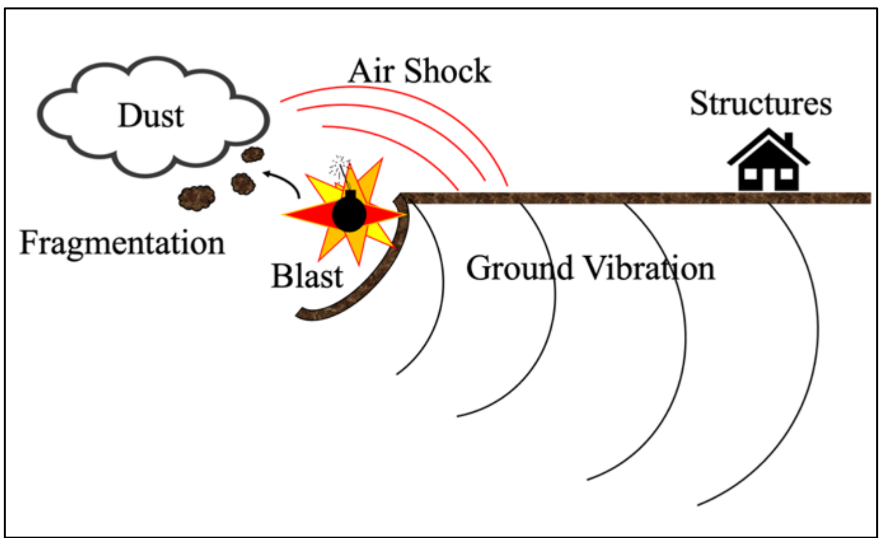

Figure 2 Schematic Depicting the Complexity of a Blast Event

1.2.11 Calculating Blast Loads

When calculating blast loads, multiple assumptions and simplifications are made in the initial design phase. Since the exact loadings cases are not known as these events are unexpected, it is best to generalize the event locations and pressure/impulse magnitudes. Simplified approaches such as TNT equivalencies and ideal blast waves, approaches used to simplify a plausible scenario [24].

With the vast type and complexities of high explosives, it is difficult to quantify weights of a certain explosive to an explosive energy. TNT equivalences are used as a common conversion factor to relate the energies released by any type of explosive to a representative detonation of a particular weight of TNT explosive. The most common example of this conversion scale is seen in quantifying the power of the nuclear bomb. Hiroshima and Nagasaki were 15 and 25 kilotons respectively, meaning the energy released in the explosion was the equivalent of detonating 15 and 25 kilotons of TNT. These equivalences are the most widely utilized base explosive quantification for energetic materials.

Ideal blast wave curves, also known as Friedlander curves [25], are generalized blast wave forms for a pressure-time history. A Friedlander curve starts at T=0, when the blast wave makes initial contact with the structure of interest causing an instantaneous rise in pressure. The pressure loading then exponentially decays with time leading into a negative pressure phase.

This waveform is described with the equation:

$$P = Ps\left(e^{\frac{-t}{t^*}}\right)\left(1 - \left(\frac{t}{t^*}\right)\right)$$

Where *Ps* is the peak initial pressure, t^* is the duration of the blast loading and t is the time within the blast event.

The ideal blast wave Friedlander curve is graphically illustrated in Figure 3.

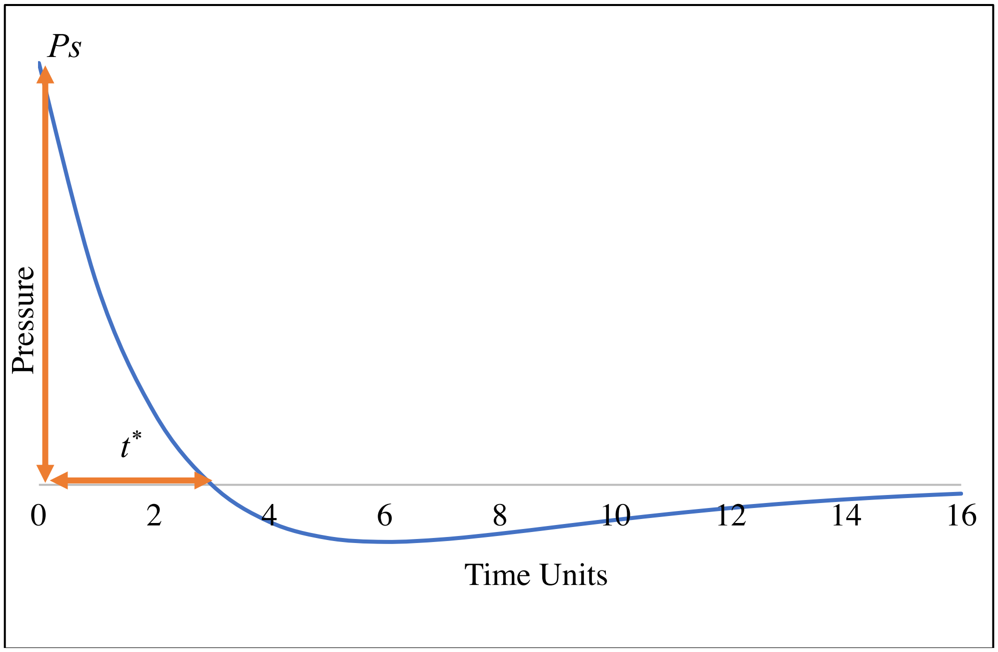

Figure 3 Ideal Blast Wave Example

1.2.12 Blast Testing Experiments

Material testing under blast conditions can be done in a variety of ways. A ballistic/blast pendulum, air cannon, shock tube or open field detonation. The pendulums are fundamental physics contraptions that measure the kinetic energy am event expels on a ridged object. For a blast pendulum, a pressure wave is loaded into a sample contained within a ridged object of known weight that is attached to a rope or string that does not readily elongate. A ballistic pendulum serves the same purpose but instead of a pressure wave loading the sample, a projectile is sent into the material. In both setups, as the assembly is struck, it is pushed back in a pendulum fashion where its height is recorded. Knowing the mass of the block, energies can be calculated from the ballistic/blast event.

Air cannons and shock tubes operate on a simple principle. Air is stored at a known high pressure and is released from its apparatus and directly loads the sample. These devices would be outfitted with pressure gauges to record a pressure-time history in areas of interest in the tube. The result is a sustained loading usually of lower pressure than initially stored.

Specifically, shock tubes are designed apparatuses that contain both a high pressure and low-pressure gas separated by a diaphragm designed to rupture mechanically by a pressure limit, or trigger. The simplicity of a shock tube leads to safe operation for repeatable, consistent, and fast testing.

Shock tubes are well known, and output pressures can be easily predicted given two initial pressures, P_1 and P_4 and their respective temperatures T_1 and T_4. Items with the subscript "4" denote the conditions within the driver gas whereas items with the subscript "1" denote the driven gas. From here, the speed of sound can be determined by $a = \sqrt{\gamma RT}$ Where γ is the ratio of specific heat (5/3 monotomic gas, 7/5 diatomic) R is the ideal gas constant And T is the temperature. The incident shock strength, $\frac{p_2}{p_1}$ can be solved by the relation:

$$\frac{p_4}{p_1} = \frac{p_2}{p_1}\left\{1 - \frac{(\gamma_4 - 1)(a_1/a_{4})(p_2/p_1 - 1)}{\sqrt{2\gamma_1[2\gamma_1 + (\gamma_1 + 1)(p_2/p_1 - 1)]}}\right\}^{-2\gamma_4/(\gamma_4 - 1)}$$

Where p_2 is the pressure behind the propagating shock wave upon firing.

However, it is seen by the shown pressure histories that compared to an ideal blast wave (Figure 3), the load is sustained over a much longer period of time leading to a more quasistatic loading in terms of blast duration (Figure 4). In the shock tube figure, P_5 is taken as the pressure measurement toward the end of a shock tube near the outlet. The abrupt jump in pressure around 7.5ms is the shock and the sustained loading (7.5ms to 15ms) behind is the pressure behind the shock wave. From t=15ms and onward, the pressure is exponentialy decayed until retrating back to atmosphereic pressures.

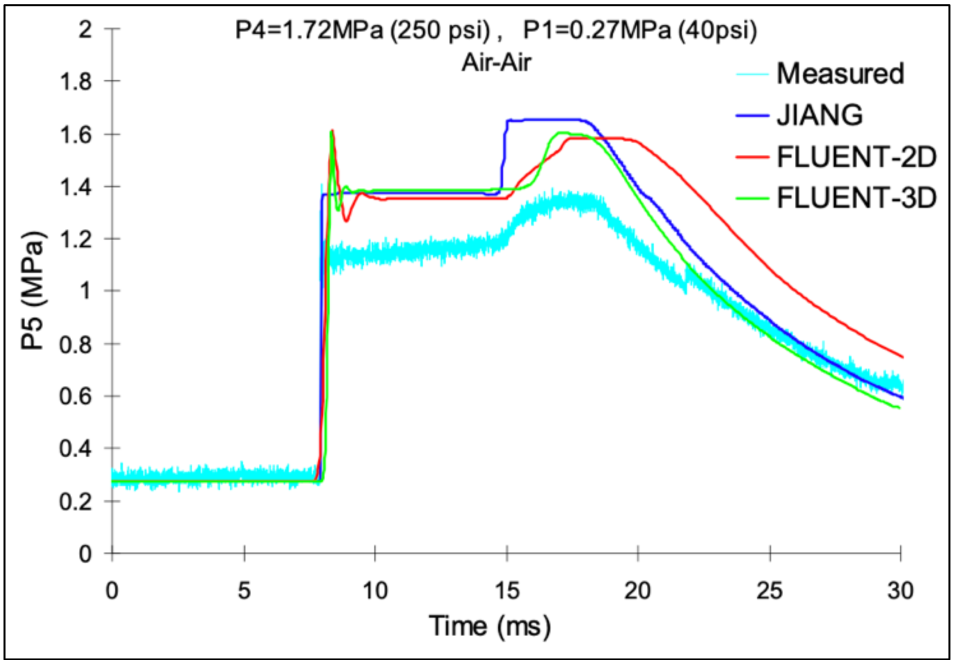

Figure 4 Normal Shock Tube Pressure [26]

As observed in the Friedlander blast curves, there is no sustained load in an ideal blast wave. A normal shock tube gives an unrealistic blast loading on a sample that leads to a higher impulse and thus resulting in more damage. However, modifications to shock tubes can be made to tailor the blast wave to become nearly idealistic. Modifications such as adding a piston, nozzle, incorporating different driving and driven gases and the addition of more diaphragms are all means of addressing the unrealistic loadings.

Open field detonation leads the most realistic experimental data but, are much harder to experimentally set up. Explosive licenses are needed to obtain, handle, detonate and dispose of high energy explosive ordinances. These experiments are also much more expensive to facilitate as the experiments need a large open area away from unnecessary danger and lack the repeatability of laboratory experiments.

1.2.13 Criteria for Blast Resistant Structures

A blast resistant structure should mitigate a variety of hazardous effects set forth by an explosion. One of the more governing criteria when certifying a blast resistant material is deflection. Dynamic deflection is measured by the maximum deformation experienced by a structure under the loading event. Typically, in a blast event, this is larger than permanent deflections. When a structure is blast loaded and undergoes deformation, inertial effects cause the structure to continue to deform past its stressed equilibrium point even after the main front of the shock wave has passed until it stabilizes its inertial effects with the materials strength. At the point of momentary rest, the inertial effects are zero, and the structure begins to rebound causing the structure to elastically “snap back”. This behavior may repeat and oscillate to release the energy that was transferred into it until remaining at rest at its plastically deformed state. Though maximum dynamic deflection is temporary, it is important to mitigate this measurement as occupants or other vital items could be at rest against the structure. As the structure deforms a higher deforming material runs the risk of colliding with vehicle or structural occupants. Permanent deflection is just as vital as it is a direct measurement on the extent of the plastic deformation. By forcing a material into its plastic regime yields the material causing irreversible damage. Though high levels of permanent deflection aren’t admirable due to the same reasons of high dynamic deflections, plastic deformation does absorb a tremendous amount of energy so there needs to be a compromise for the *allowable* deflection the structure can undergo absorb and distribute energy.

Deflection characteristics can be governed by many mechanical properties. Some of the most notable ones include a materials ductility, yield and ultimate strength which are both influenced by a strain hardening and strain rate behavior. High ductility and strength are admirable in a blast event due to increased capacity for energy adsorption capabilities.

Strain rate effects occur under higher strain rate events, where a materials quasi-static properties (modulus, yield, and ultimate strength) increase without doing anything physical to the material resulting in higher amounts of energy absorbance of a material to mitigate blast damage (Figure 5).

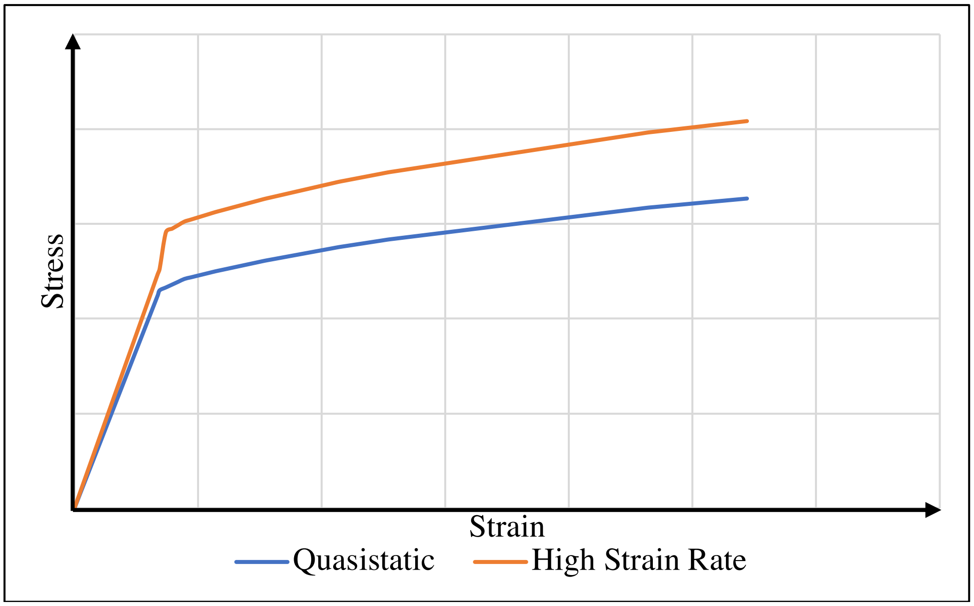

Figure 5 Strain Rate Effects

This is behavior is admirable in a blast event because a material can have this inherent behavior and exhibit higher strength without needing to add more material or modifying a structure. For the American Institute of Steel Construction (AISC) blast design guide 26 [27], strain rate effects are incorporated in analytic equations to increase the yield strength of a structural steel by 110-120%. If not accounted for, heavier beams would have to be included in the design adding weight and cost to a project. However, this strain rate sensitivity behavior might sacrifice a materials ductility.

Stain hardening, or work hardening is the ability to increase both hardness and stiffness of a material by plastic deformation [28]. Under the loading, a material quickly reaches its elastic limit and then undergoes large plastic deformation. Upon unloading and reloading, the material raises its yield point and thus, hardens. This behavior continuously hardens until failure [29], [30]. As seen in Figure 6, the material reaches its linear elastic limit rather quickly, but has a long period of ductility where it continues to plastically strain and carry more stress.

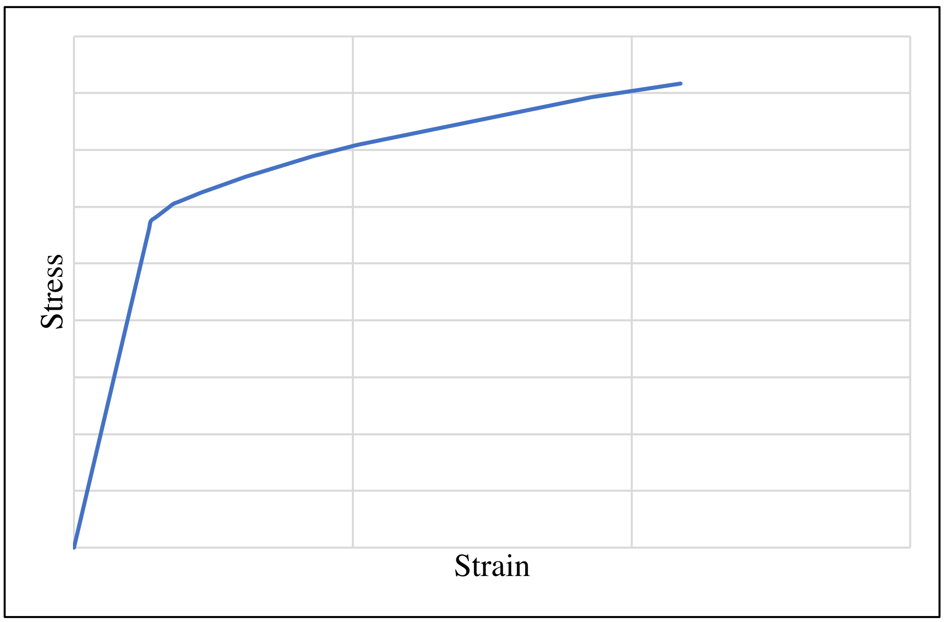

Figure 6 Strain Hardening Behavior

A material structure should not only have acceptable ranges of deflection, but also mitigate secondary hazards like fires. In many cases, an explosive event is followed by a rapid fireball which lags behind the initial blast wave. This fireball can pose a secondary threat to the occupants contained within the structure if the material ignites. There are levels of ways to assess fire retardance, smoke production, toxicity, and flame propagation. Flammability classifications for plastics such as UL 94 [31] serve to standardize how fire retardant a material is. A blast mitigating material should not produce smoke, release toxins into the air and should not readily propagate fire as these are all preventable secondary threats that increase lethality of an event.

1.2.14 Thermoset and Thermoplastic Composite Response to Blast

Composites are great candidates for applications where energy absorption is critical like blast. Under high damage yielding events, composites can absorb energies by matrix cracking and crushing, fiber pullout and rupture and interlaminar delamination [2], [32], [33]. Composite fibers and matrix's have been researched extensively for finding means of increasing energy absorbing capabilities under dynamic loadings [34]–[37]. With the large amount of surface areas between each composite laminate ply and the fiber-matrix interfaces, there is a large capacity for energy absorption. Furthermore, with the high tensile strength of the reinforcing fibers, the energy absorbing capabilities are expanded.

1.2.15 Aluminum Response to Blast

Aluminum alloys have been widely studied under blast loading and are often used for occupant protection in buildings or military vehicles due to their high strength to weight ratios. Armor grade aluminums demonstrate high elongations and strengths, key characteristics to a well performing blast material. Other important characteristics are manufacturability, weldability, fatigue, and corrosion.

A unique behavior of aluminum is the ability to exhibit earlier discussed strain hardening and strain rate effects. Aluminum alloys have temper options to include strain hardening such as those with designated temper codes T and H. For instance, temper codes T indicates that the is thermally worked whereas temper code H indicates the alloy is cold worked. Thermally working an aluminum alloy leads to higher stability in strength [18]. Similarly, armor grade aluminums are also exploited for their ability to show positive strain rate sensitivity by increasing tensile strengths up to 150% [38].

Common armor grade aluminum alloys fall within the copper containing 2000 series and zinc containing 7000 series. Generally, the 7000 series offer higher strength properties but lack the fatigue resistances one would find in 2000 series armors [39] therefore, the selection of an armor grade material should be dependent on the location of application on a structure where the governing loading is a concern.

Weldability plays a key factor in governing which material to use in a blast resistant structure. Thick metallic armor cannot always be press formed into complex geometries of a blast resistant structure. Therefore, sections of armor plate must then be cut and joined together by welding to develop a reliable high strength joint. However, not all aluminums are easily weldable. A 7000 series aluminum is notorious for being difficult to weld where as 1000 series is quite easy [40]. To take advantage of the performance of 7000 series aluminum and avoid the welding challenges such as integration in an FML.

Numerous approaches to modeling aluminum alloys under blast or impact events have been done with good results [3], [41]. The models typically incorporate Johnson-Cook to account for the high strain rates recorded in the experiment. The Johnson-Cook parameters are either obtained from literature or experimentally obtained via split Hopkinson bar tests at a reference strain rate where a stress strain curve is obtained, and the Johnson-cook equation is then parameterized and validated with the split Hopkinson tests.

1.2.16 Fiber Metal Laminate's and Blast

A well-known commercial product, GLARE (Glass Reinforced Aluminum Laminate), utilizes thin layers of aluminum and S-2 glass fiber thermoset pre-impregnated sheets for blast resistance. GLARE was heavily studied in the 1990's after the Pan Am flight 103 disaster and entered into the aerospace industry on the Airbus A380 to help mitigate such potential catastrophes. GLARE panels exhibited superior impact and fatigue properties, enhanced corrosion and fire resistance and was overall less weigh per areal density than the traditional metal cladding.

When tested under blast events, FML panels exhibited superior energy absorbing capabilities and was overall less weight per areal density than the traditional metal cladding [5]. Langdon et. al. attributed the high amount of energy absorption through debonding of the material interfaces, fiber fracture, and rupturing and petaling of the aluminum plies. Further characterization was done to understand failure types with increasing laminate thicknesses and explosive loadings [5], [42], as well as changing constituent materials [3],[22]. Langdon et al. analyzed how symmetric fiber metal laminates of different proportionalities of aluminum and thermoplastic composite affected its behavior under blast [42]. Due to the highly localized nature of their explosive loadings, severe isolated damage occurred around the site of direct contact with the explosive with thinner panels. The result was a "punch through" like shear failure mechanism similar to that of an actual projectile. The localized nature of the damage was seen to transition over a larger area with thicker panels leading to a broader area of delamination and permanent displacements. The dynamic behavior under the blast event was not analyzed. The dynamic deflection is crucial when designing blast panels as the dynamic deflections can actually be greater than permanent deflections [43]. The dynamic events captured under blast loading can better characterize and explain the interactions of the two materials through both observation and model validation.

Though the material tested showed promising results with the large amounts of overserved mechanisms for energy absorption, the substitution as a thicker armor replacement for more extreme loads quickly poses issues. Utilization thin plies and sheet metal becomes impractical due to the increased difficulties of manufacturing thick FML structures. Issues such as manufacturing thick thermoplastic composites and bonding the metal sheet to the thermoplastic all pose manufacturing difficulties. Furthermore, the interactions of the two constituent materials are unknown. The FML seemingly acts as a "black box" where complex wave interactions propagate through alternating layers of material causing damage and delamination until being completely attenuated in the material. To understand and truly characterize the interactions of the material system, and to present practical solutions for thicker material structures, a single interface of a thermoplastic and metallic system is needed.

Avachat et. al addressed some of these shortcomings with his own research [44]. Avachat approached fiber metal laminates at a single interface of an epoxy/carbon fiber and aluminum system for marine structures under blast loading. Though, the single interface was addressed, the need for a single interfaced thermoplastic constituent is needed. Furthermore, the blast loads induced on the structures in his study were submerged. Due to the near incompressibility of water, blast events overpressure duration times are magnitudes shorter than those in an air blast event (0.3ms compared to about 3ms). With the blast propagating through water into the structure that is air backed (water-structure-air), the material loading is much different than that of an air-structure-air loading. Avachat also addressed the importance of dynamic deflections and modeled the deflection-time history of the single interfaced laminates. ABAQUS simulations were conducted to estimate the dynamic deflections during the experiments, but never experimentally validated. As expected, Avachat discovered that the dynamic deflections were more of the permanent deflections he recorded.

The ideology of the fiber metal laminate presents a light-weight armor solutions that can exploit multiple materials inherent characteristics for an optimized material system. However, further research needs to be conducted to fully observe both the dynamic behavior as well as to characterize the induced damage. In this study, a single (asymmetric) thermoplastic composite/metal hybrid armor panel will be experimentally characterized using laboratory scale simulated blast loadings. To fully understand the blast characterization, high speed imagery will be recorded and used to optically calculate dynamic deflections via fringe projection methods. Non-destructive evaluations such as ultra-scanning will be used to quantify delamination through the thickness of the composite. Scanning electron microscopy will be used to observe local failure mechanisms within both the thermoplastic composite and the metal strike face. Knowing these damage characteristics, an LS Dyna MAT_054 Enhanced Composite Damage Model will be utilized to yield a representative model to further explain the dynamic behavior seen in the high-speed imagery. Additional testing is then conducted under the same experimental procedures with a baseline monolithic plate of aluminum, thus elucidating the differences in dynamic response and permanent damage for hybrid panels compared to a baseline armor grade solution.

Chapter 2 Methods

For this work, the shock tube is the main choice of experimental high-pressure blast loading. The Composite Vehicle Research Center (CVRC) shock tube is unique from other shock tubes in the fact it utilizes different components to obtain consistent pressure loadings that are near identical to a Friedlander blast curve. A double intermediate diaphragm, low pressure diaphragm, blast nozzle and piston added to help shape the pressure history diagram to become near idealistic. However, implementation of these components demands modifications to simple shock tube theory, and simple analytical equations to predict the pressures do not apply.

2.1 The CVRC Shock Tube

The shock tube at the CVRC is a Stalker type shock tunnel (Figure 7). Stalker tubes are used to test re-entrant space vehicles on shock loading experienced when re-entering the Earth's atmosphere. This shock tunnel utilizes a freely moving piston with a designed mass generate high loading pressures without having dangerously high initial loading pressures. The shock tube is split into four main sections. The driver, intermediate, driven and blast tube sections.

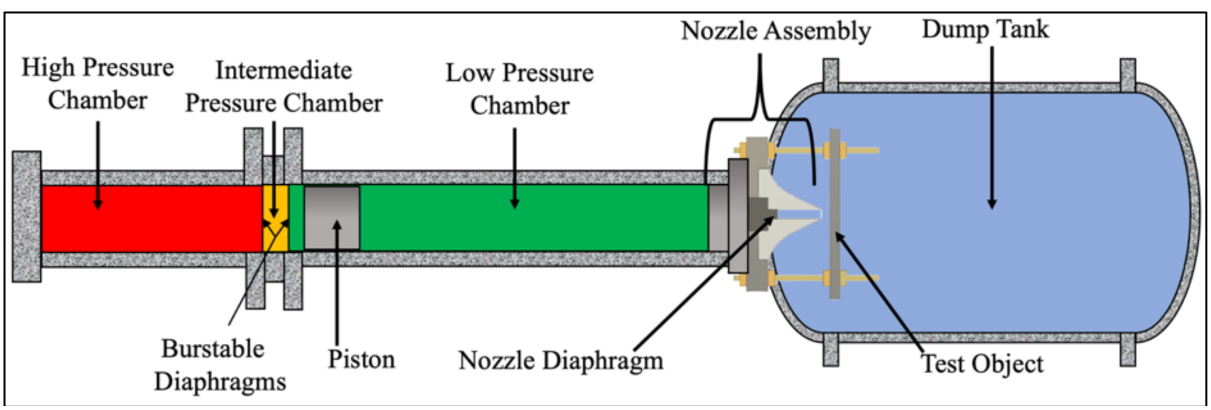

Figure 7 Schematic of MSU's Shock Tube [45]

The driver section is initially filled with high-pressure air acting as the driving gas, P_4. The driven section is initially filled with lower pressure air, P_1 and contains a piston with a designated mass placed at a designed distance from an intermediate section separating the driving and driven sections. The intermediate section is bounded by a double diaphragm system and is pressurized with a pressure, P_3 of the average pressure of P_4 and P_1 sections. The intermediate section acts as the firing mechanism. Once the entire tube completely pressurized to the desired specifications, the intermediate section is vented to atmospheric pressure as the carefully designed double diaphragm system then simultaneously ruptures at a set pressure. The rupture of the diaphragm initiates the blast sequence. The double diaphragm system allows a higher ratio if P_4/P_1 and help with a more uniform rupture process. The last section is the nozzle assembly containing the blast tube contains another diaphragm used to bound the low-pressure chamber allowing a P_1 above atmospheric pressure. Upon diaphragm rupture at the intermediate section, the free piston is accelerated into the low-pressure chamber adiabatically compressing the driven gas. As the piston compresses the driven gas, the pressure increases exponentially until the nozzle diaphragm contained within the blast tube, initially bounding P_1, bursts. The rupture strength of P_1 is designed to be considerably higher than the intermediate diaphragms. This truncates the pressure loading and builds the pressure before rupturing (Figure 8).

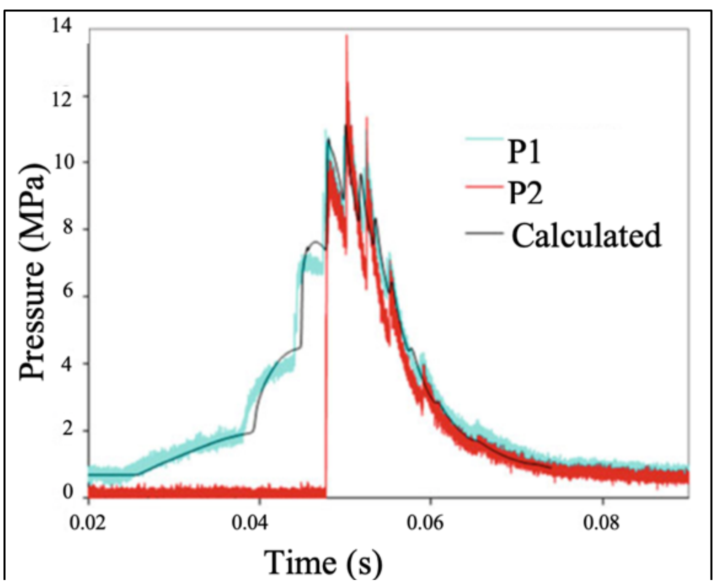

Figure 8 Pressure Profiles Before and After Nozzle Diaphragm [45]

A shock wave develops within the blast tube due to the high pressure gradient between the compressed gas and ambient air. Due to the extremely high gradient across the shock wave boundary, choked flow is experienced and a maximum shock wave speed of Mach 1 is obtained. The choked flow restricts the mass flow rate of the gas exiting the nozzle. The piston continues to compress the gas and increase the pressure. By calculating the initial P_4, P_1, piston weight, nozzle size and diaphragm rupture rate, the piston motion is designed to slightly bump the nozzle in a continuous compressive stroke. As the reflecting expansion wave catches up with the piston, The piston drawing back into the tube and drastically decreasing the pressure exponentially and shortens the overpressure duration to a few milliseconds. The instantaneous pressure spike after the nozzle diaphragm rupture is characteristic in a fielded blast event and that of a Friedlander blast wave. Pressures generated in the shock tube have reached up to 133 MPa, Mach numbers of 5 and temperatures of up to 1000°C[26], [45], [46]. Related pressures to TNT equivalence of roughly 80kg of TNT at 1m standoff distance or 1000kg of TNT at 2.5m standoff distance by work done by Ngo et. al.[47]

2.2 Shock Tube Experimental Set Up

A 1kg piston was machined out of 6061-T6 aluminum stock. Though the nozzle assembly was constructed with soft a copper bump stop in event of piston impact, to further reduce the risk of damage to the blast nozzle system, a softer, aluminum material was chosen as this would become damaged rather the more critical nozzle assembly. The outer diameter of the piston was exactly 0.01mm less in diameter than that of the compression tube. This tolerance ensured an air tight fit and that there was no leakage though the piston ensuring true adiabatic compression. The length of the piston was about twice of that of its width to avoid the piston rotating in the compression tube and getting lodged. The weight was distributed so that the center of mass was directly in the center of the piston to further reduce the risk of lodging the piston in the chamber.

2.2.1 Diaphragm Construction

To ensure the shock tube did not fire prematurely, the intermediate chamber's diaphragm must be manufactured to resist the pressure differences across the three respective chambers (high and intermediate and intermediate and low). Knowing the pressure loading case to obtain the desired pressure in these experiments, a rupture pressure of at least 14.5MPa was needed to allow full pressurization of all 3 chambers. To determine the burst pressure of the diaphragms, an empirical relation was first developed. Literature far underestimated the rupture pressure for the diaphragms as the unbraced rupture area of the diaphragm (Figure 9) was square compared to literatures circular brace so experimentally specific and numerical methods were needed to determine the rupture strength.

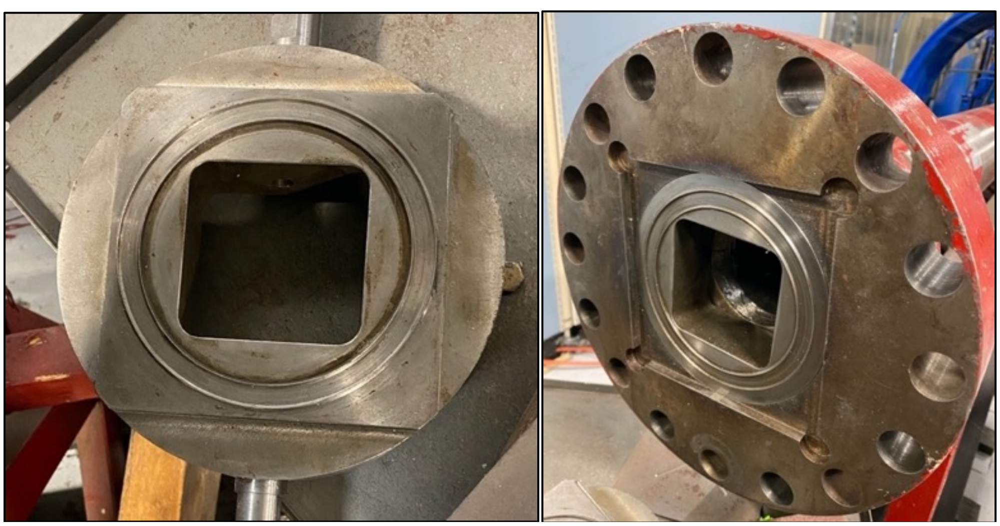

Figure 9 Diaphragm sealing rings

The intermediate chamber diaphragms were constructed out of 4130 steel plate of various thickness and scored in an "X" pattern to promote failure at a desired pressure. The "X" pattern was scored by clamping the 150mm square plate and centering a 9.53mm ball mill bit. The depth of the groove was set, and the cutter traced the desired "X" pattern. The manufacturing processes and finished diaphragm are shown in Figure 10.

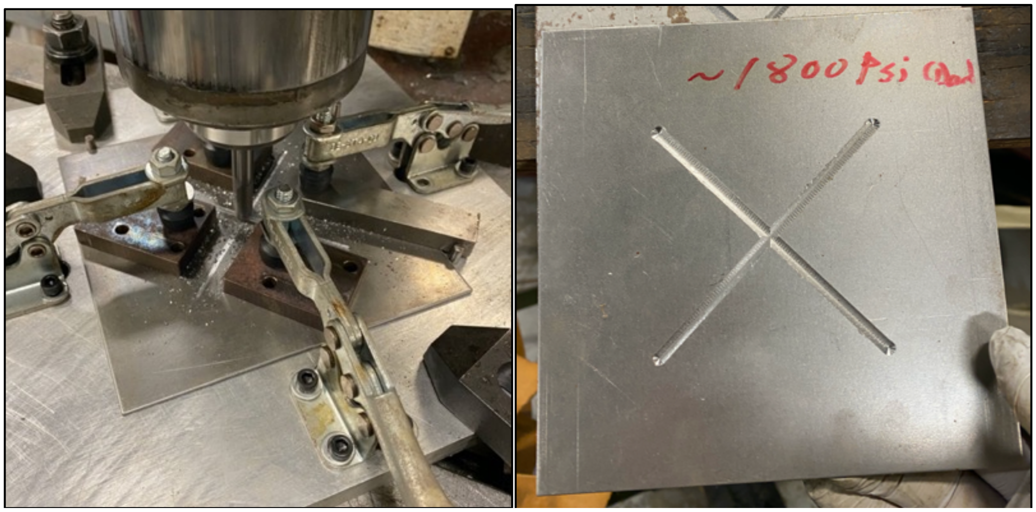

Figure 10 Diaphragm Construction

Diaphragms were loaded into the shock tube without a piston and the high-pressure chamber was pressurized until burst. The burst pressure was then recorded and plotted to see the variance among plate thickness and score depth. The ruptured diaphragms were observed to be a complete and clean rupture as intended by the manufacturing process. Various thicknesses and score depths were tested and validated with finite element analysis.

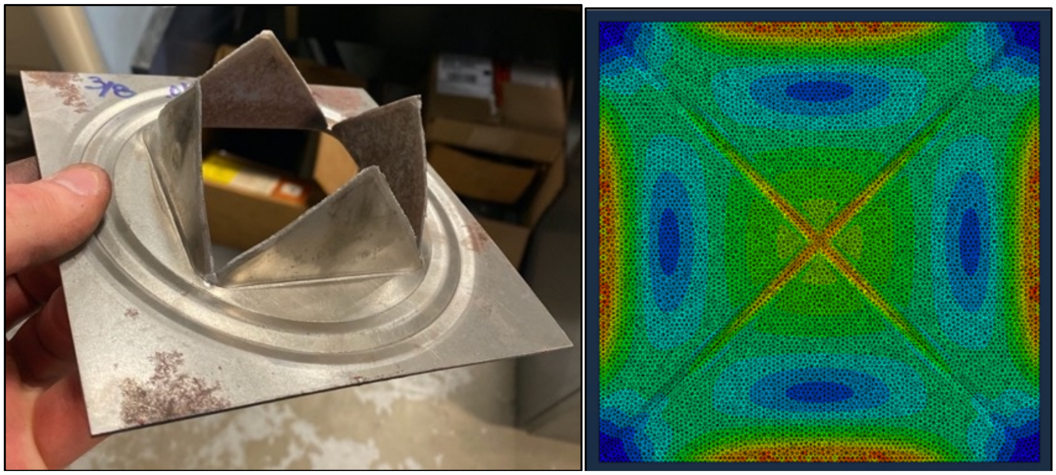

Figure 11 Left: Ruptured Diaphragm Right:Finite Element Validated Diapgrahm Rupture

For this experimental set up, a 1.8mm 4130 steel plate with a groove depth of 0.3mm was used as the preliminary test diaphragm. This led to a burst pressure of 17MPa which gave enough buffer to account for any manufacturing variability causing premature rupture when under the experimental test loading pressure of 14MPa.

The smaller nozzle diaphragms were manufactured and validated in the same process. However, this rupture pressure is needed to be far higher as the diaphragm acts to truncate the rapid rise in pressure building in the blast tube portion of the low-pressure chamber upon firing the shock tube. A higher burst pressure leads to a higher and more defined instantaneous increase in pressure and a more representative Friedlander blast wave. Using the same 1.8mm 4130, a groove depth of 0.381mm was scored in a similar "X" pattern. Finite element models validated the small diaphragm rupturing at 51MPa.

2.2.2 Pressure—Time History Recording

Pressure data outside of the nozzle was needed to determine the material loading for damage characterization and the LS Dyna model validation. A M109C11 PCB piezoelectric pressure sensor was selected as its maximum pressure was far above the predicted 120MPa overpressure (direct contact with nozzle) as well as withstanding a flash temperature of 538°C. The sensor also and an extremely short rise time ($2\mu s$) and proved to be the best selection available. To obtain the pressure loading curve of the material, a 1" steel plate was manufactured to hold a piezoelectric pressure sensor the exact distance from the blast nozzle that the material was designed to be. The sensor was flush mounted to record all surface effects on the plate. Figure 12 illustrates the pressure sensor mounted in the shock tube and is further detailed in Figure 13.

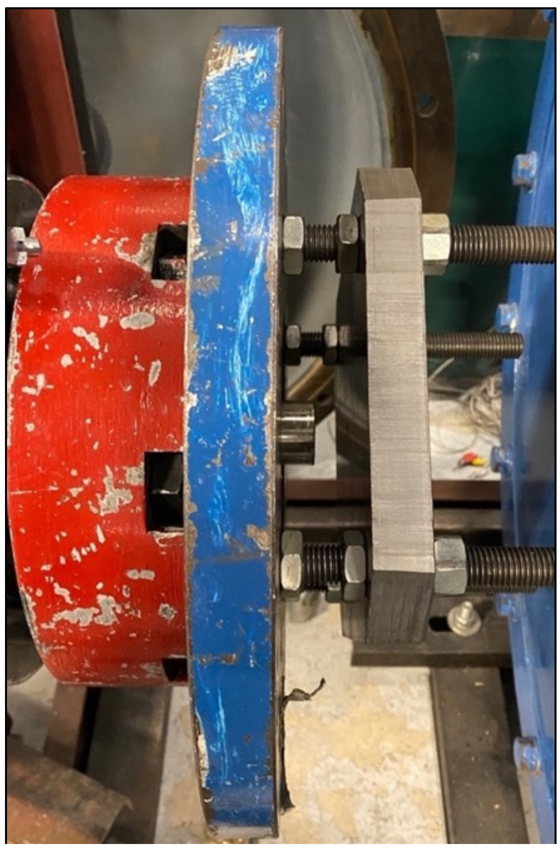

Figure 12 Pressure Sensor Mounted in Shock Tube

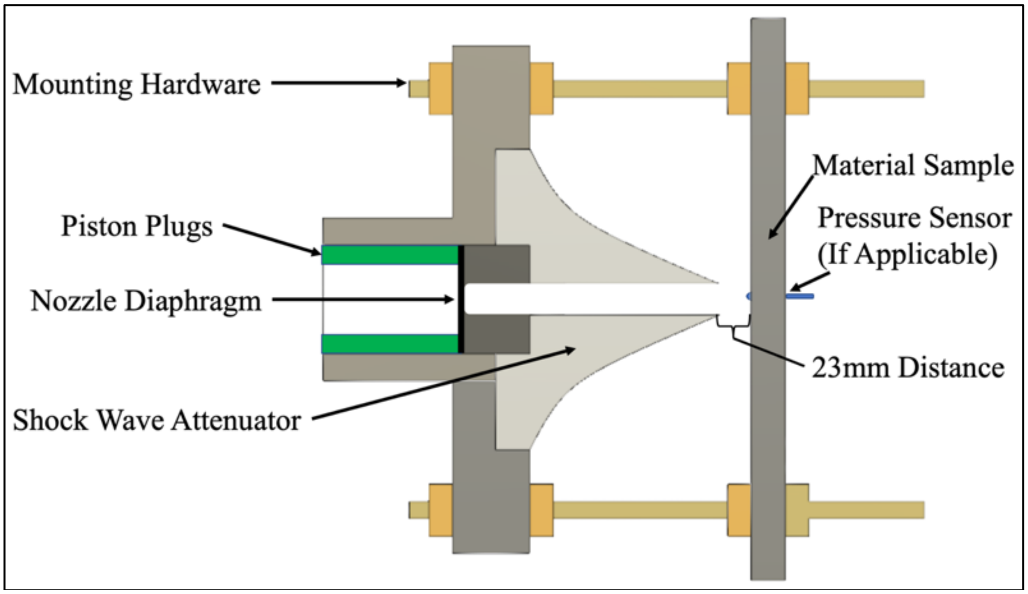

Figure 13 Detailed Schematic of Blast Nozzle Assembly Shown in Figure 12

The ridged plate and pressure sensor was then tested using the exact experimental set up needed to test the material (Table 3). The generated pressure profile was assumed to be identical to those loading the experimental panels. Assuming the ambient air temperature stayed the same in the enclosed laboratory environment and the nozzle diaphragm ruptured at the same pressure, the pressure curves could be assumed to be identical. This assumption is needed as the tested material cannot be outfitted with the pressure probe physically altering the material.

Table 3 Shock Tube Experimental Loading Set Up

Item	Value
High Pressure Chamber	28.26MPa
Intermediate Pressure Chamber	14.5MPa
Low Pressure Chamber	0.69MPa
Nozzle Diameter	23mm
Piston Weight	1kg
Intermediate Chamber Diaphragm Rupture Pressure	17MPa
Nozzle Diaphragm Rupture Pressure	50MPa
Distance from nozzle	23mm

2.3 Preliminary Shock Tube Data

A series of calibration shots were conducted and yielded consistent repeatable Friedlander structured blast waves (Figure 14). The pressure curves depict a steep rise time with exponential decay. However, upon further inspection, there are multiple “spikes” in pressure in the pressure-time history. These pressure spikes were thought to introduce additional damage into the material sample and therefore must be attenuated. Two approaches were conducted to address these additional rises in the pressure profile to obtain a more Friedlander like blast form.

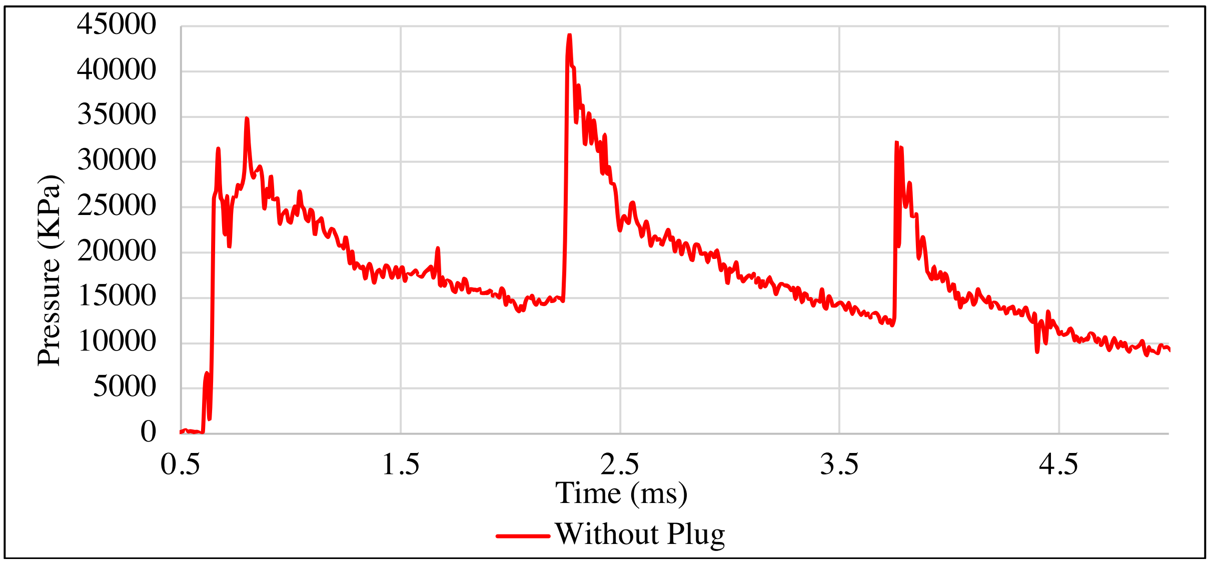

Figure 14 Shock Tube Pressure Time History Artifacts

2.3.1 Reflected Shock Wave Attenuating Device

Initially, these additional pressure spikes were thought to manifest due to the shockwave that is expelled from the nozzle, bouncing off the ridged pressure plate, reflecting into the shock tube end and then back into the pressure sensor. This phenomenon would occur over a multiple of cycles and eventually diminish when the pressure was completely expelled out of the compression tube. A device was fitted to the end of the shock tube to address this potential source of experimental error. This theory was squandered upon initial testing but brings upon valid observations that could introduce experimental error. Even though this phenomena wasn't addressed with this experimental test, it was a valid design consideration and was implemented on all further tests.

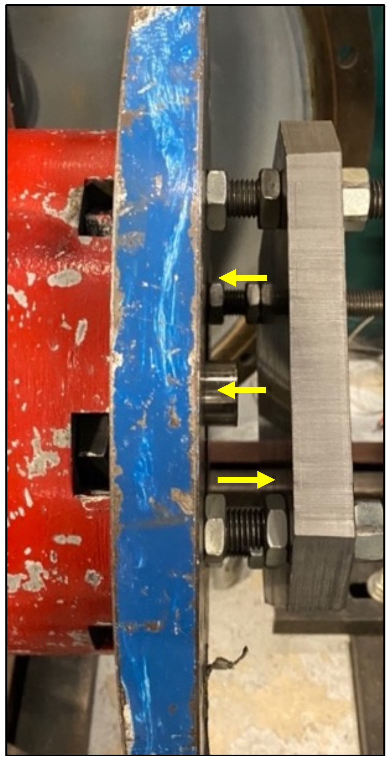

Figure 15 Theorized Reflected Shock Waves

The attenuative device is a log-spiral duct which has been studied in literature for the geometric capability of focusing shock waves [48], [49]. The continuous curvature allows for shock wave focusing at the cusp of the log-spiral without expanding the shock wave and causing more shock wave artifacts (Figure 16). Utilizing the log-spiral geometry for focusing waves, an axi-symmetric log-spiral curve was developed to redirect these waves. Figure 16 shows the focusing capability of the log-spiral. For this application, the shock wave needed redirection, so the half plane of symmetry shown in the figure was utilized on the outside profile of the attenuating device to the shock wave was directed toward the external edge of the ambient dump tank.

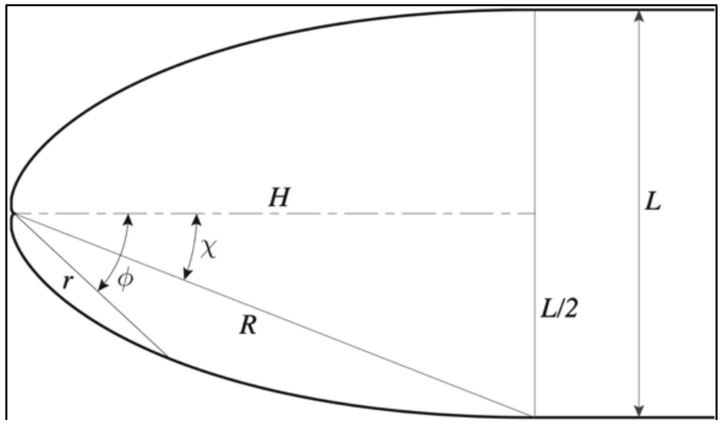

Figure 16 Schematic of a log-spiral [48]

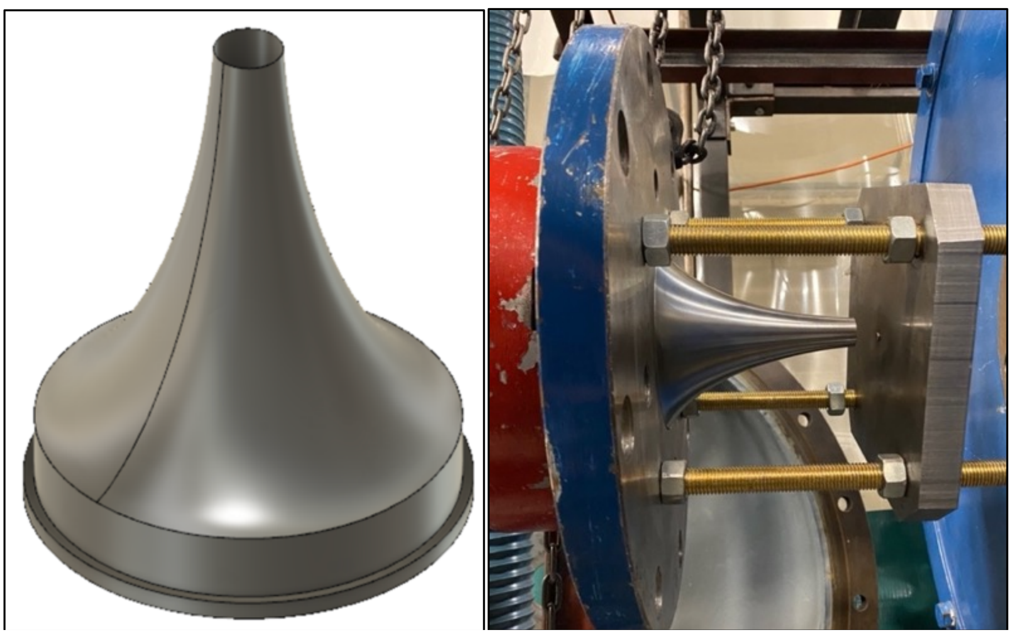

Figure 17 Shockwave Attenuation Device and Fitment on Compression Tube and Nozzle End

The curvature of the log-spiral curve is dependent on the incoming shock wave speed. Knowing the incoming Mach number, a characteristic angle, χ, can be obtained by the relations described by Milton [49]. The value can then be implemented in the log-spiral equation depicted below where $R = \frac{L}{\cos(\chi)}$

$$r = R * exp\left(\frac{\chi - \theta}{tan(\chi)}\right)$$

From here, a length of spiral, L, can be chosen and θ and r can be plotted in a polar coordinate system and then translated into a Cartesian coordinate system for means of modeling in a CAD system for manufacturing.

The speed of the shock wave estimated by obtaining the pressure gradient within the tube after nozzle diaphragm rupture. By ideal gas laws and finite element diaphragm rupture strength, the pressure ratio of compressed gas (P_2) to ambient air (P_1) was upwards of 500. This is far higher than the pressure ratio ($\frac{P_2}{P_1}$) needed for choked flow (1.894). With the presence of choked flow, the estimated Mach number was assumed to be 1.

It is important to note that Milton [50] found that the *focusing* ability of the log-spiral diminishes at Mach numbers below 2. However, the main objective of this device is not to focus but redirect it away from the experimental test object. When designing for a Mach number of 1, the log-spiral device led to an extremely thin-walled structure and preservation of the device was doubtful after a repeated high-pressure tests. For this reason, a higher Mach number of 2.1 was selected as it led to a broader curve and a thicker walled structure.

The device was machined of 4140 steel and tested. As previously mentioned, for this experimental set up, the device did not attenuate the reflected shocks nor have any effect on the original experimental data. However, it highlights an important design flaw that has the potential to introduce wave abnormalities under different experimental conditions. Since there was no change in experimental data, it was kept in the experimental set up for the remainder of this work.

2.3.2 Shock tube plug inserts

With the initial theory of external reflected shocks being debunked, the excess pressure spikes were ruled as an internal shock tube issue. Understanding the fundamental mechanics of the moments just before and after the nozzle diaphragm burst were key in understanding where the spikes were resonating from.

As the shock tube is fired and the piston and accelerated forward, a pressure wave propagates in front of the piston further compressing a localized section of air. This pressure wave is large enough to cause the nozzle diagram to rupture and cause the pressurized air to vacate the compression tube and impinge on the material or pressure sensor causing the rapid rise in pressure (Figure 18 top). However, the differences in diameter of the inner tube wall and the nozzle assembly diameter allow for the pressure wave causes the propagating shock wave to be partially reflected and sent propagating toward the opposite end toward the piston (Figure 18 bottom). The reflected shock wave eventually collides with the piston face. At this moment the pressure in front of the piston face increases pressure. The rise in pressure from the colliding pressure wave and piston face pushes the piston backwards until the reflected wave, now propagating toward the nozzle, drops the pressure on the front side of the piston allowing the back pressure of the piston to thrust it forward causing yet another pulse of pressure that soon catches up with the original reflected shock wave, and further strengthens it. The process repeats until the internal energy of the system is eventually depleted. These internal reflections and additional piston movements were assumed to cause the additional pressure spikes.

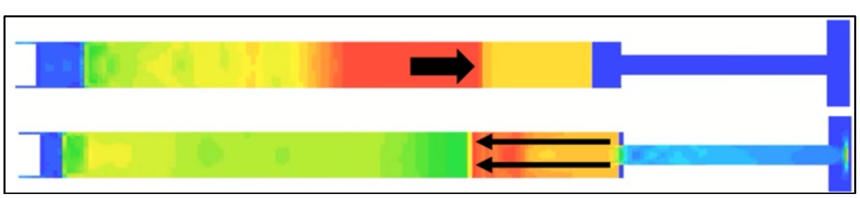

Figure 18 Finite Element Model Showing Internal Shock Wave Reflections

To address these behaviors that cause the additional pressure spikes in the Friedlander form without changing key characteristics of the shock tube that allow it to simulate blast loading, the piston motion must be controlled. A simple solution was theorized to restrict piston motion upon diaphragm rupture. Instead of experiencing a full piston stroke and having internal wave reflections cause additional piston thrusts, plugs were inserted to prematurely stop the piston at a distance further away from the end diaphragm. Prematurely stopping the piston allowed for the initial pressure wave from the accelerated piston to propagate down the tube to burst the nozzle diaphragm. Afterwards, due to the increased length of travel for the wave reflections and vacating mass flux of pressurized air out of the nozzle, the reflected pressure wave is cannibalized partially, or completely, where the pressure in front of the piston never exceeds that of the back pressure creating a piston that is restricted in space allowing for a single pressure peak throughout the entire loading.

To do so, the plugs were inserted between the piston and the copper bump stop. The internal diameter of the plugs was that of the nozzle assembly itself making a seamless transition between pieces so additional wave artifacts could not manifest.

To estimate the length of the piston plugs, ideal gas formulations were used and coupled with adiabatic compression rules. Knowing the rupture pressure of the nozzle diaphragm, the original temperature, pressure, and volume of gas contained within the low-pressure chamber, a theoretical final volume was calculated at which the final pressure exceeded the diaphragm rupture strength. This final length established a maximum length where exceeding the limit would produce a lesser pressure expected and result in an unruptured diaphragm and failed test.

The plugs were constructed out of a nylon tube with an outside diameter of the inner diameter of the shock tube and an inner diameter of the nozzle assembly (53mm). Nylon was chosen to prevent damage to both the nozzle assembly, and the piston face, as the piston was designed to directly impact the plugs. The calculated maximum length of the plugs from the ideal gas calculations was determined to be 662mm. The 662mm length was divided into individual sections of plug to obtain a characterization of the length of plug itself. A series of tests were conducted to test how the length of plugs attenuated the additional pressure peaks in the pressure-time history (Figure 19).

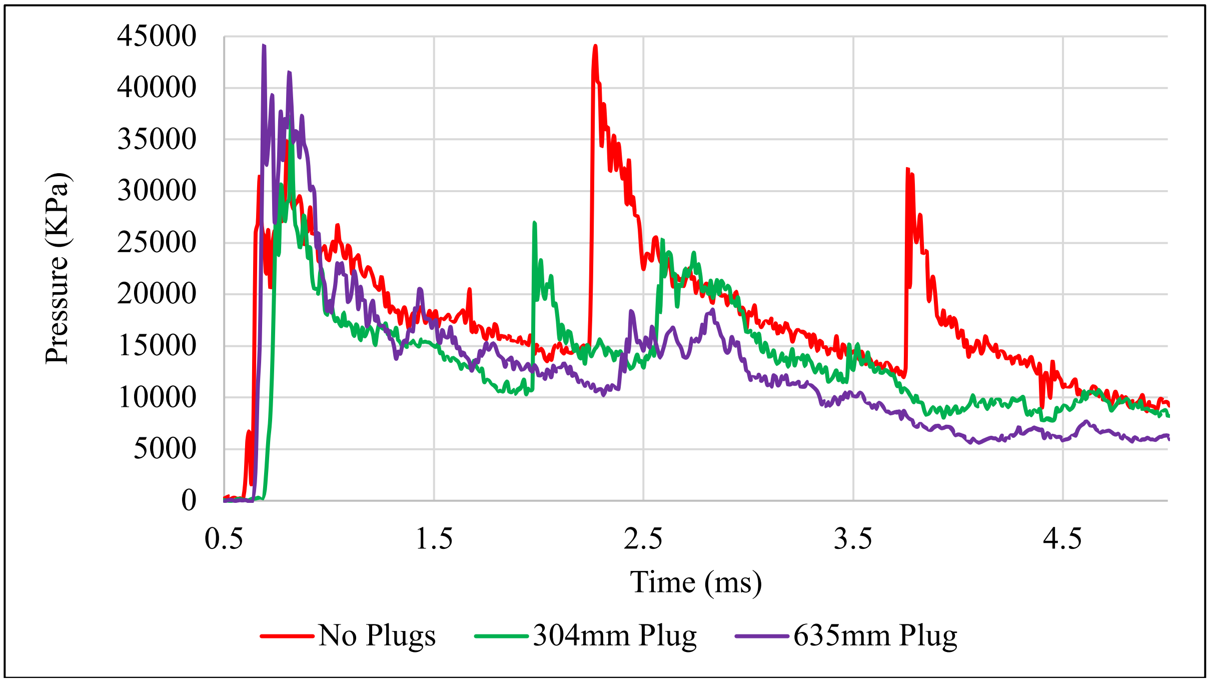

Figure 19 Effect of Piston Plugs on Shaping Pressure Profile

With the addition of the initial 304mm plug, all spikes were attenuated or completely removed from original data. Adding a second 304mm plug (608mm total plug) the excess spikes were nearly all removed. An extra 27mm (635mm total) of plug was added and further improvement was observed. To push the limits of the plug length, a total of 662mm of plug was added (an additional 27mm plug was added). This length exceeded the capacity of the ideal gas calculations and proved the theorized behavior correct when the test did not rupture the final diaphragm resulting in an incomplete test. Clearly, the implementation of plugs restricting the piston motion reduces the severity of the additional pressure spikes.

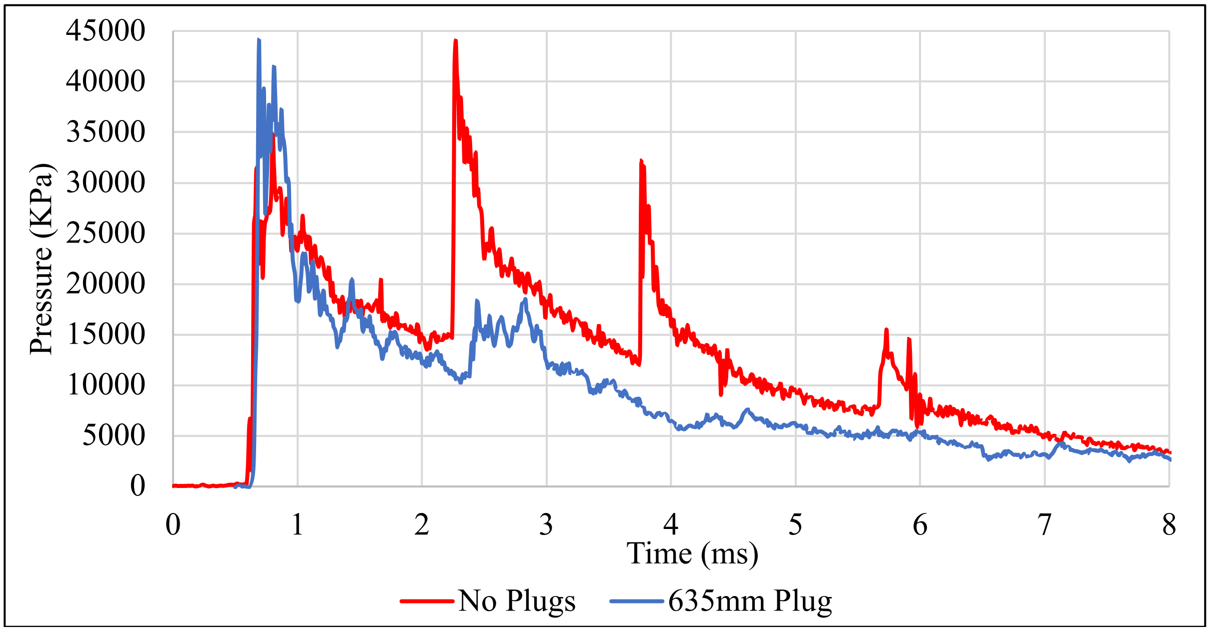

Figure 20 Effect of Piston Plugs: With Max Length and Without

The results were repeatable and deemed suitable to declare as a Friedlander form as hardly any additional pressure impulses were experienced throughout the exponential decay portion of the Friedlander curve.

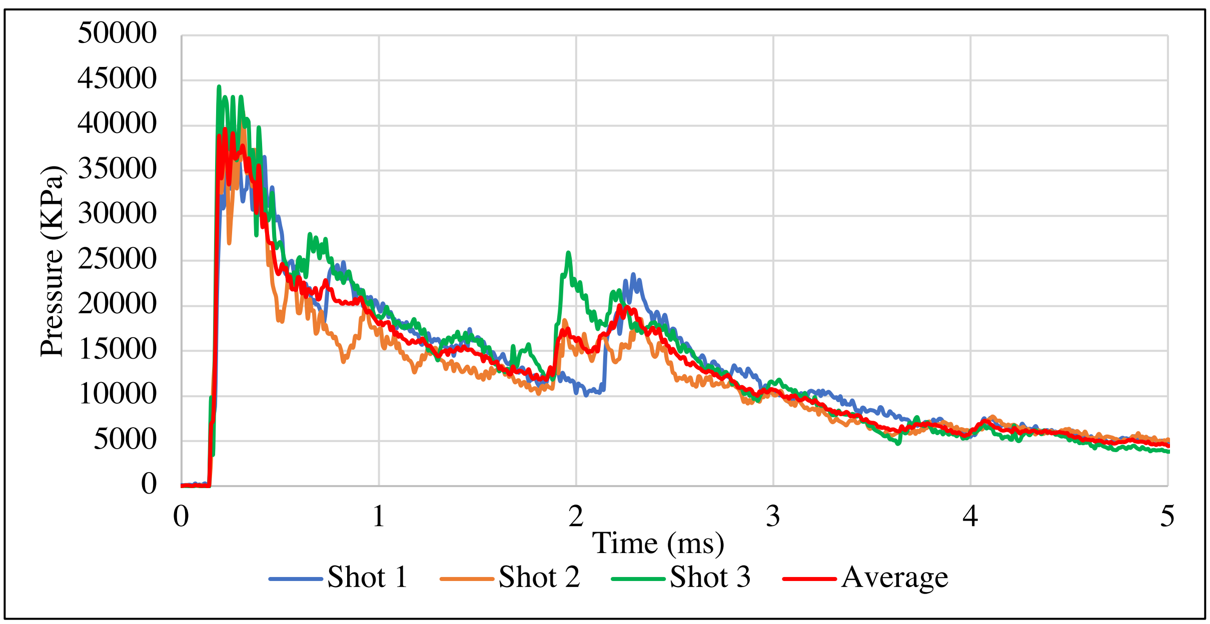

Figure 21 Series of Calibration Shots and Average of Test Loading Case

2.3.3 Shock Tube Pressure Distribution

The last component in fully characterizing the shock tube pressure loading was determining the area of loading at a specified distance away from the nozzle exit. The exit behavior of an open ended shock tube has been studied in literature [51]–[53]. Medhi et. al. found that as a shock wave propagates out of an open-ended tube, for every tube diameter away from the open end of the respective tube, the radius of spherical shock front increased by the length of the diameter. In terms of pressure loaded area on a plate, at one nozzle distance away the distributed pressure loading diameter is roughly 2 nozzle diameters. For this reason, it was decided to characterize all pressure curves at a distance of one nozzle diameter (23mm) away as it would yield a large pressure distribution of around 56mm around.

A simplified fluent model was created to further prove the general shape of the pressure loading distribution upon exiting the nozzle (Figure 22).

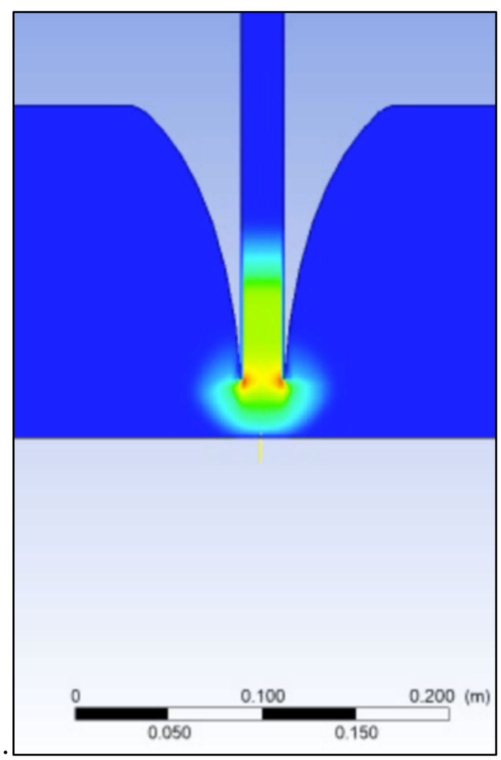

Figure 22 Fluent Analysis of Expansion of Pressurized Gas Expelling out of Blast Nozzle

As expected, the shape of the pressure distribution is hemispherical. The model shows good agreement with the rate of expansion when impinging on a plate 23mm away.

To experimentally validate the general shape and to quantify the local pressure of a specific point on the loaded plate, Fiji Film Prescale; a pressure sensitive film, was applied to the surface of a ridged plate and tested at a distance of 23mm. The pressure sensitive film contains glass beads of various sizes that rupture when a specific pressure is reached. Upon rupturing, a reactive pigment is released. The color density of the pigment is then used to determine the pressure reading at that particular spot. A high color density indicates a pressure around the max of the film rating and an unregistered color density reveals a reading below the minimum detectible pressure of the film. Two individual Prescale films, low and medium strengths, were added to the ridged plate. The pressure distribution was estimated to range through the detectible range of both films so both were needed for a full characterization. The medium film had a range from 10MPa to 49MPa was placed in the centralized area of the nozzle where higher pressures were expected. The low range film had a detectible pressure range of 2.4MPa to 10MPa and was placed behind the smaller film to catch the area toward the outside of the localized area in front of the nozzle where the gas was assumed to expand. The overlap in pressure ranges between both films enabled the entire pressure loading to be captured in the significant pressure ranges that were assumed to cause deformation.

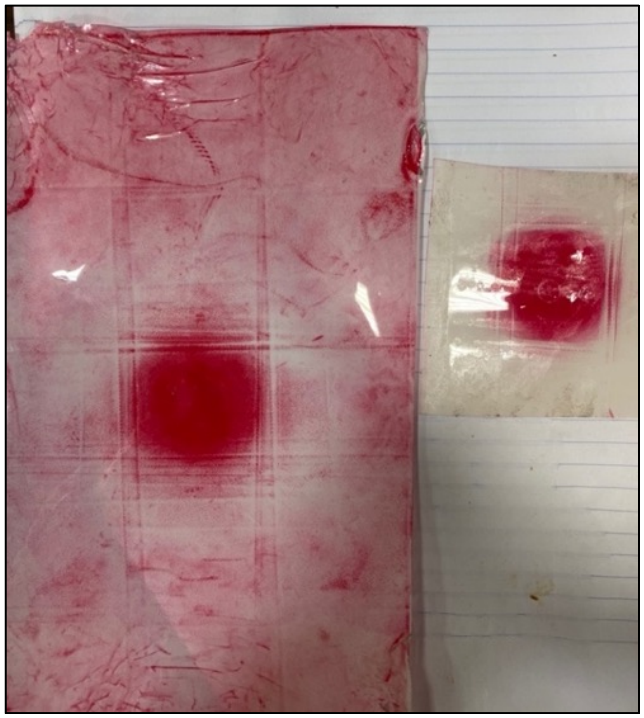

Figure 23 Left: Exposed Low Pressure Right: Exposed Medium Pressure Film

The films were exposed to a blast pressure loading and sent to Fiji Film for statistical image processing analysis to obtain a contour plot of the pressure distribution over both pressure films.

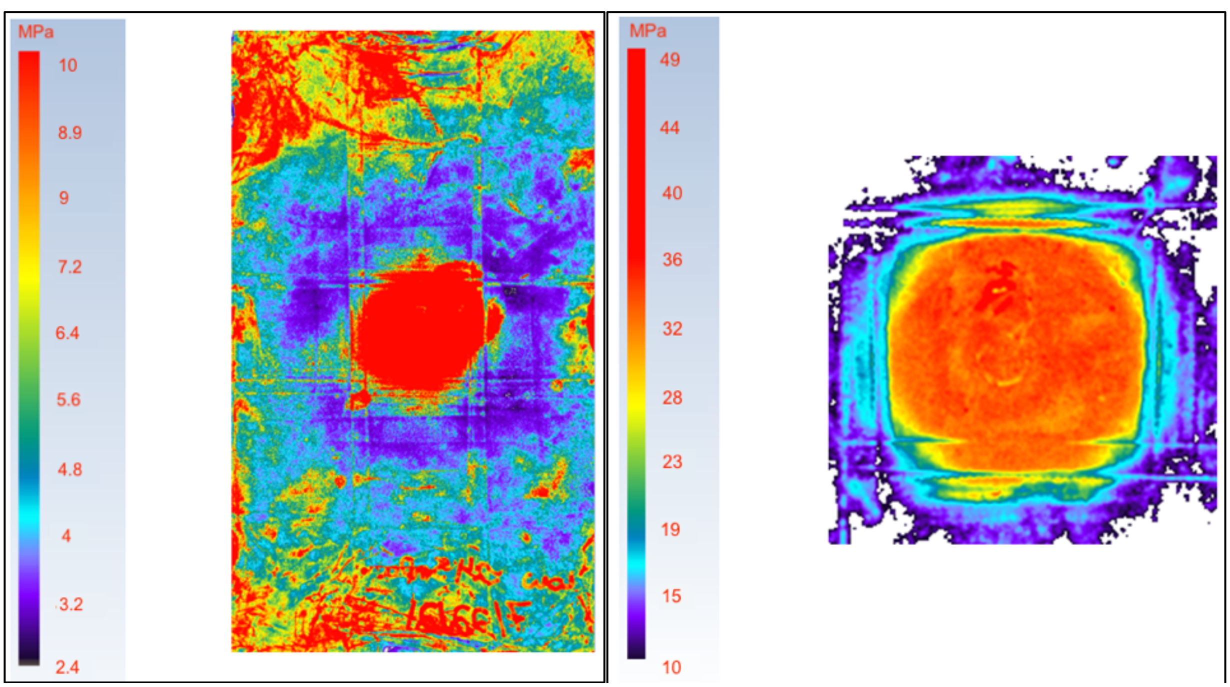

Figure 24 Left: Low Pressure film pseudocolor analysis Right: Medium pseudocolor analysis

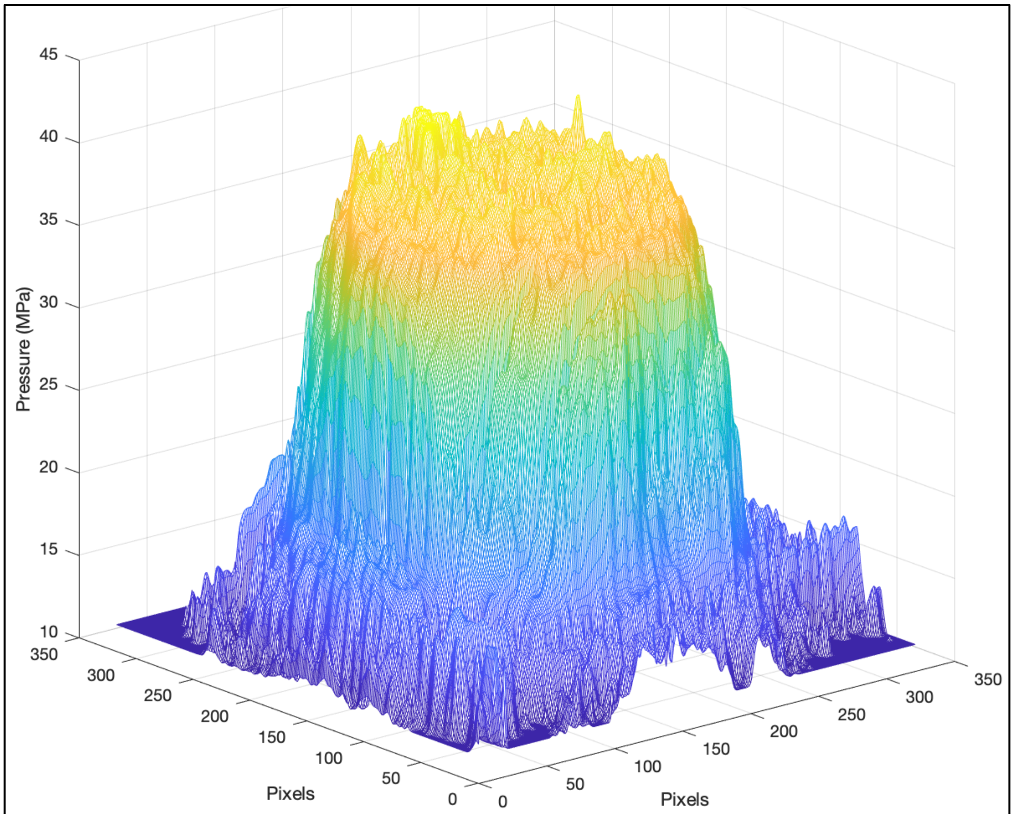

Figure 25 3D Photo Pseudocolor Analysis of Medium Pressure Film

The pseudocolor films validated the gas expansion theory by recording a hemispherical like pressure loading that was 56mm in diameter (2 diameters) when held 23mm (1 diameter) away. The low-pressure film was found to be maxed out around 10MPa and experienced a significant gradient down to 3.45MPa. The maxed-out section was expected as this area of the film was below the medium pressure film with a higher pressure threshold. The film captured the globally expanded pressure distribution well. The medium pressure film neared 37.9MPa which was expected from the previous pressure characterization tests. The pressure loading quickly reduced below undetectable range of the film which was then recorded and indicated on the low-pressure film. The overall width of loading from 3.1MPa to 37.9MPa was approximately in 118mm diameter.

2.4 Fringe Projection Setup

Dynamic measurement of deflection is challenging in a high strain rate event. Digital image correlation (DIC) proves difficult as a 3-dimensional picture is needed to correlate optical strain measurements. Under high deformation, the DIC grid pattern is likely to get damaged under excessive deformations under blast loading. Strain gauges lead to similar issues where the resolution of time recording isn't sharp enough, or the gauges are removed under high deformations. Moreover, this process required a second high speed camera which was unavailable for these experiments. To avoid these issues and obtain accurate real time deflections, an optical method was needed that required no modification to the material panel I.e., speckle painting and stain gauge fitting. Fringe projection techniques were introduced as the optical method requires a single camera. Furthermore, the only modification to the material of interest is painting the back of the deformable material with high elongation paint. Fringes are projected onto the sample and cannot be destroyed under high deformations.

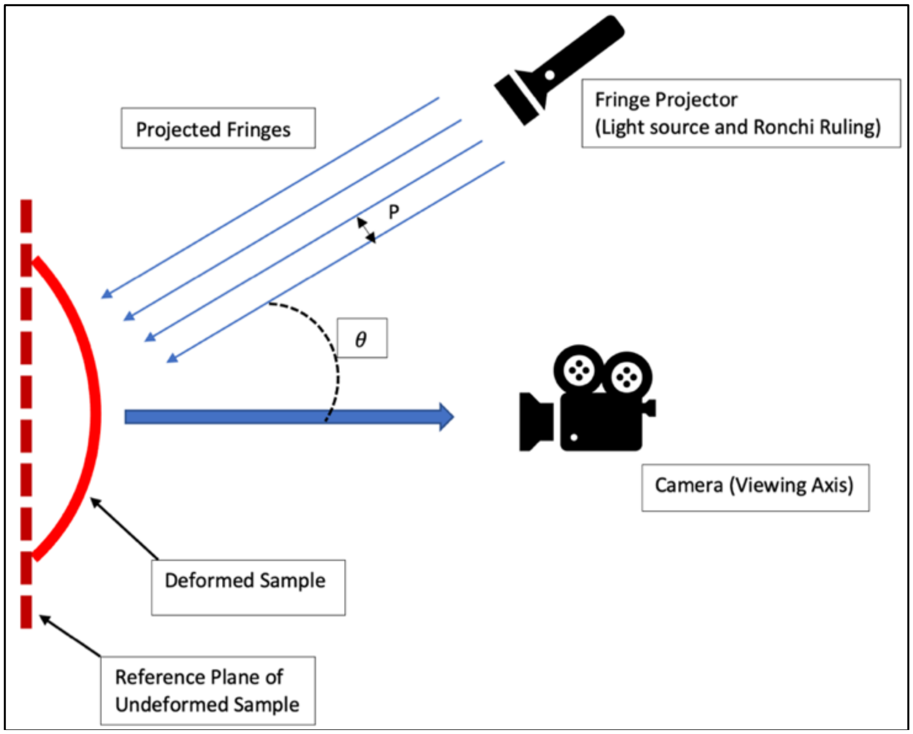

Figure 26 Fringe Projection Detail

Fringe projection is an optical measurement process in which vertical fringe patterns are projected onto the back the material of interest. As the specimen deforms, the fringe patterns then begin to deform with the material (Figure 27). Knowing the pitch of the fringes and the optical set up of the data acquisition system, the Z-displacement can be obtained from any deformed image simply using the intensity of the captured image in a process developed by Oritz [54].

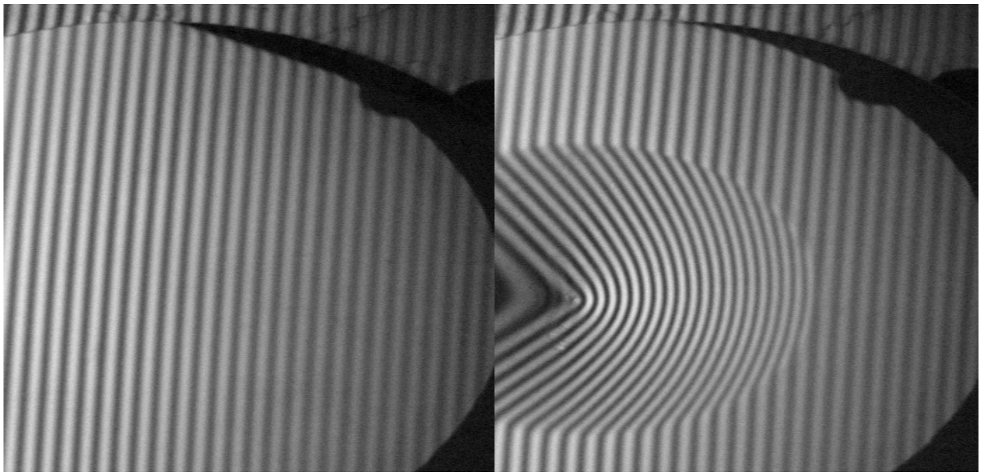

Figure 27 Depiction of Projected Fringes Deforming with Deformed Material

Utilizing an images intensity distribution, fringe data can be manipulated to calculate the out of plane displacements by subtracting the spatial phase shift of a flat reference and deformed object image. The intensity distribution over a regular 8-bit black and white image ranges from 0 to 256 where 0 corresponds to black and 256 to white. After projecting fringes on the sample, the respective image is normalized and shifted by the pitch distance, P. The pitch distance of an image is the measured distance between the center of fringe peaks.

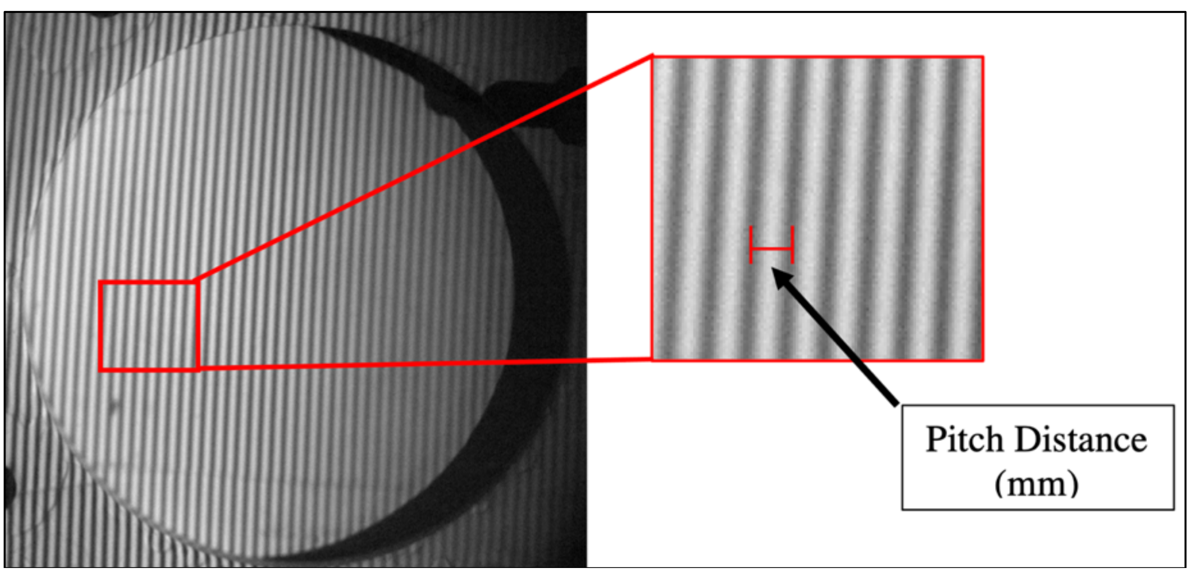

Figure 28 Pitch Distance

Both reference and object image are phase shifted by a series of 5, P/4 phase steps yielding 5 images for each original image:

$$I_1 = I(i, j - \tfrac{P}{2})$$
$$I_2 = I(i, j - \tfrac{P}{4})$$
$$I_3 = I(i, j)$$
$$I_4 = I(i, j + \tfrac{P}{4})$$
$$I_5 = I(i, j + \tfrac{P}{2})$$

The images are then spatially phase shifted to find the modulated phase, ϕ.

$$\phi = arctan\left(\frac{2(I_2 - I_4)}{2I_3 - I_5 - I_1}\right).$$

The modulated phase is calculated for a flat reference image and with an object of interest (ϕ_R and ϕ_o). Here, the differences between the modulated phase in the object and reference image are used to find the displacement of an object in a set of 2D images.

$$\phi_f = \phi_o - \phi_R$$

The difference in the modulated phase contains a relative displacement that is phase wrapped on the interval of [- π, π]. These 2π peaks are identified in the unwrapping technique to reveal the relative displacement of the test specimen. The unwrapped profile is then scaled by the displacement factor K, determined by P and the angle of the projected fringes $\theta,$ in the equation,

$$K = \frac{P}{2\pi * tan\theta}$$

Giving the finalized displacement as:

$$\Delta Z = \phi_f K.$$

To project these fringes, a 1000-watt halogen light was used and focused with a 150mm PCX lens and a 101.6mm half ball lens. The focused light was then passed through a Ronchi grating of 20 lines/mm. The grated image was then projected onto the specimen through a 12.5-

75mm zoom TV lens. Figure 29 is a detailed image of the fringe projector. The utilization of a 1000-watt halogen light was needed as it was the most easily available, brightest point-like light source. Difficulty arose with the extremely high operating temperatures of the halogen light source that often cracked the Ronchi grating. To cool the optical lenses and Ronchi grating cooling fans were installed and the operation time of the fringe projection system was kept minimal. Though light emitting diodes (LED's) run at a far lower temperature for the same amount of luminosity, many optical lenses would be needed to focus the light into a single point source where it would become impractical with the refractivity and transmissibility dwindling the highly scatted light source.

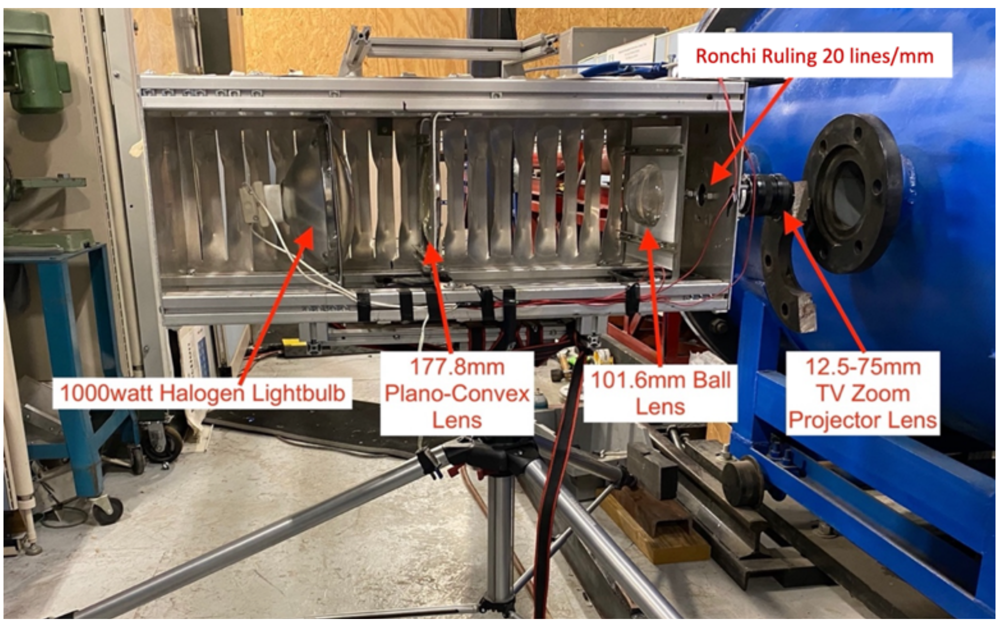

Figure 29 Fringe Projector

Figure 30 illustrates the optical set up for the fringe projection process. The projected fringe pattern was directed to the back of the sample by an angled mirror. A Phantom V2512 series high-speed imaging camera captured the images from an additional angled mirror.

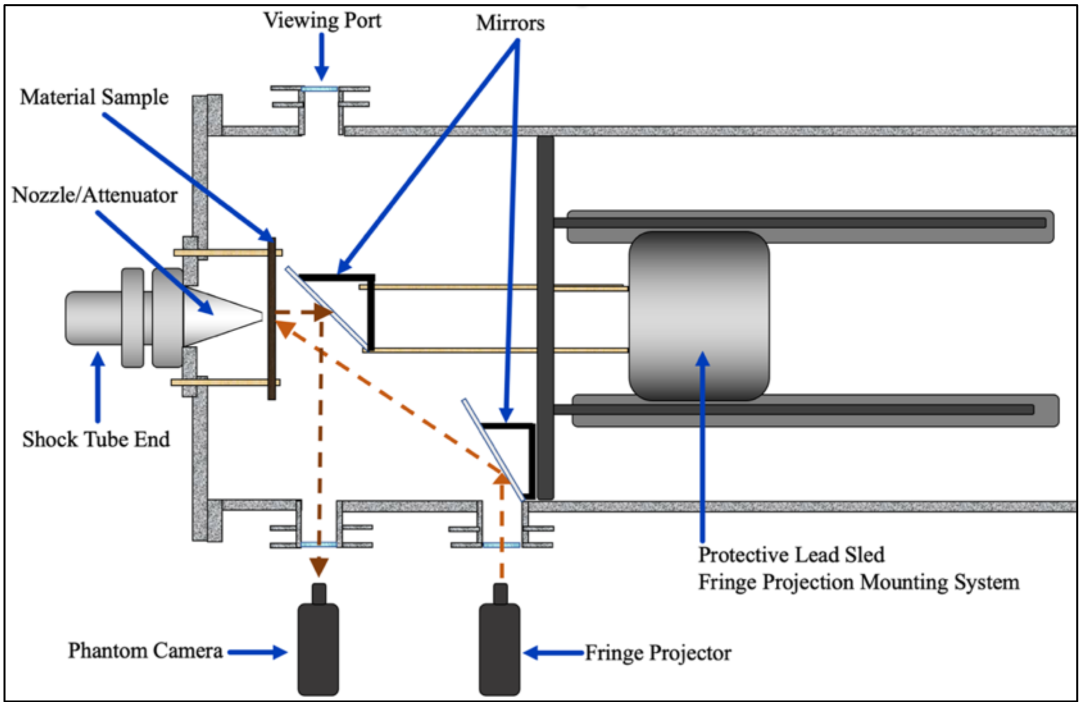

Figure 30 Shock Tube Fringe Projection Optical Setup

2.4.1 Fringe Projection Calibration

The fringe projection system calculates displacement unique to an optical setup. The distances between the mirrors and cameras as well as the type of optics used all effect how the fringe projection technique calculates the displacement of the images. For that reason, an experimentally specific calibration process is needed to ensure repeatable and accurate displacement calculation.

To calibrate the fringe projection system, a calibration cone was used of known height and width. The calibration cone was selected to be 4.97mm tall with a radius of 10mm. This height was chosen as it was closest to preliminary tested samples and their resultant permanent deflections. A flat image without the calibration cone, and an object image with the cone were taken in the exact experimental set up as the material tests was designed for. The images were then loaded into MATLAB where the fringe projection process was conducted and the calibration constant, K, was calculated and saved for implementation in all image analysis as long as the optical setup remained the same. Figure 32 illustrates the contour map of only the localized area of the calibration cone. The focused area allowed for truncating of the parts of the image that were unnecessary for analysis that may induce noise in the calibration process.

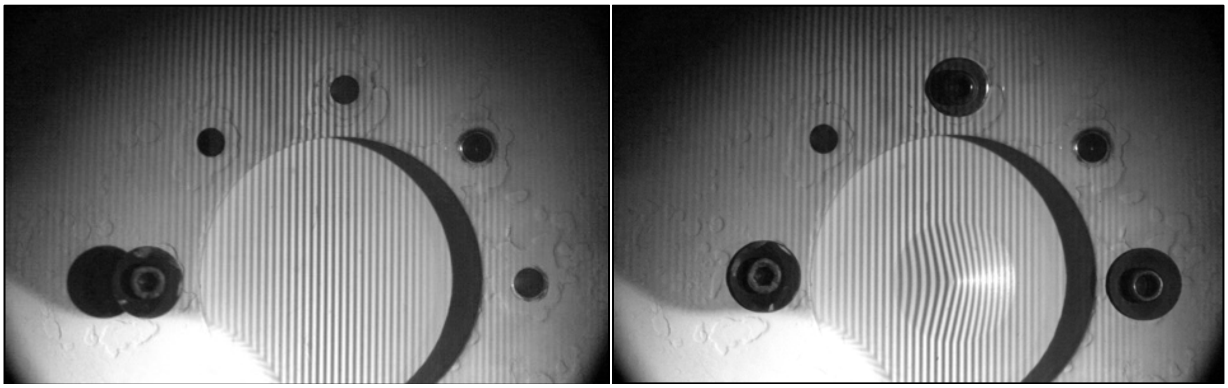

Figure 31 Fringe Projection Calibration Images of Calibration Cone

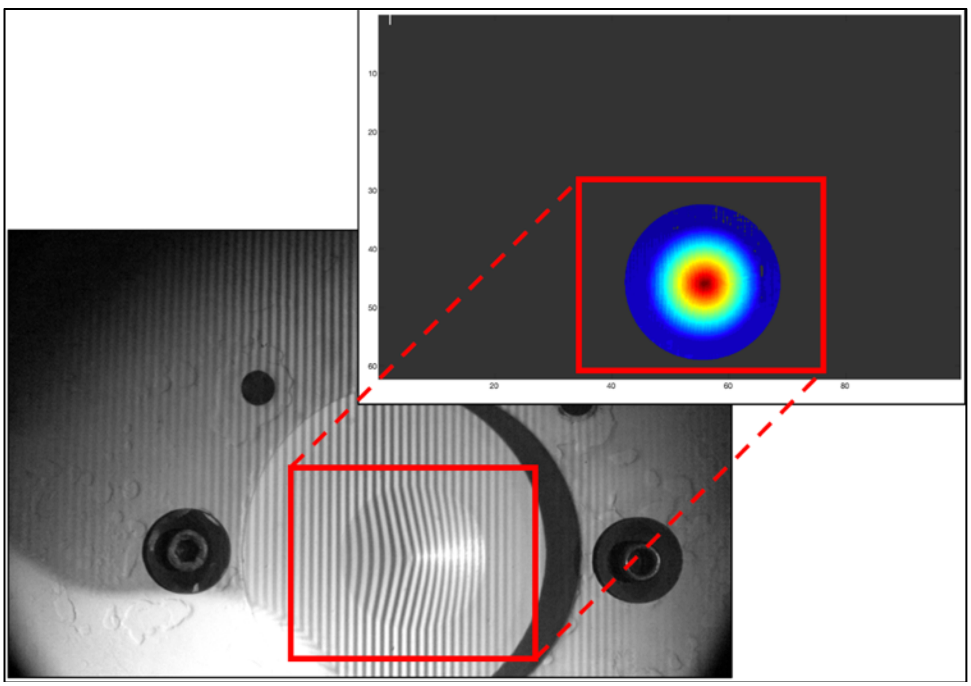

Figure 32 Fringe Projection Calibration Cone Contour Map

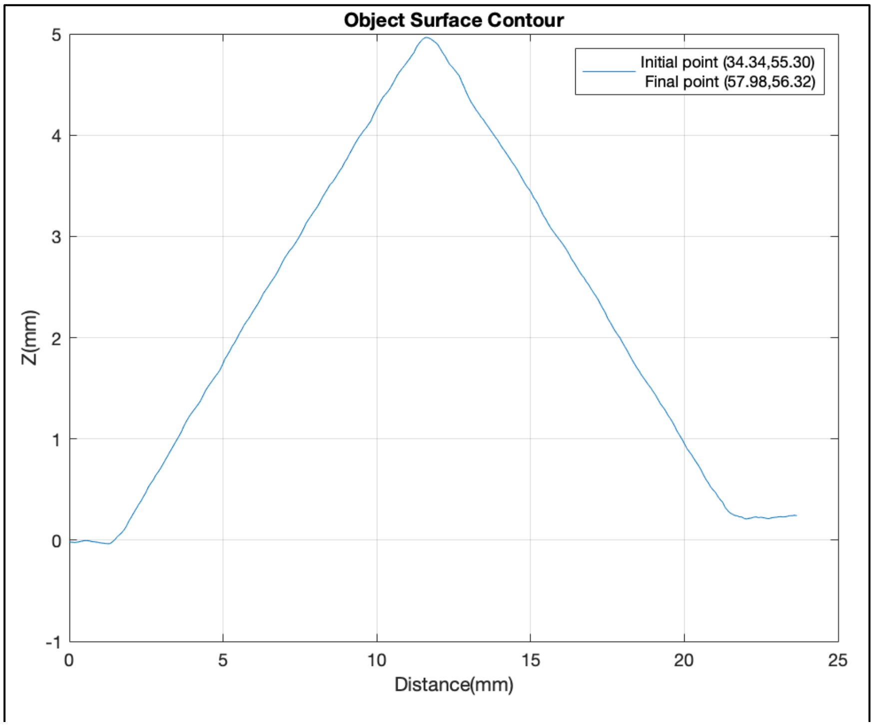

Figure 33 Cross Sectional Displacement Plot of Calibration Cone

Table 4 Calibration and Optical Parameters for Fringe Projection Analysis

Spatial Resolution	7.87mm/pix
Calibration Constant, K	0.4863
Pitch Distance, P	2mm

Chapter 3 Material Design

3.1 Thermoplastic Composite Selection

Toray Cetex® TC940 PET/GF (polyethylene terephthalate) (Table 30 in appendix) semicrystalline polyester unidirectional composite tape was chosen as the representative thermoplastic composite. The high strength and low cost of the TC940 make it an attractive material for large, heavy structures. TC940 is a prepreg thermoplastic composite system with 60% unidirectional glass fiber volume fraction. The unidirectional tape comes in 0.26mm thick and 165mm wide tape. Core composite density of the material is 1.89g/cm^3 compared to 2.81

g/cm^3 of aluminum. The recommended processing temp for the thermoplastic matrix system is 254–277°C.

PET is one of the strongest and lightest thermoplastic material that is commercially available. PET is an excellent thermoplastic for applications where flammability is a concern such as explosive events like blast. Neat PET resin material exhibits decent flame retardance superior to many other thermoplastics [55]. The resin can also be blended with phosphonates to promote further flame retardance in the neat material [56]. The neat PET resin used in the TC940 composite has an HB rating under UL94 Flammability Rating (Table 31 in appendix) showing good resistance to horizontal burn propagation making it an ideal candidate for thermoplastic composite in blast loading events.

3.2 Aluminum Selection

Commercially available 5083-H116 aluminum is one of the most abundant and commonly used armor grade aluminum available to the general public. However, for the specimens in this work, there was no material thickness available thin enough to show deformation and damage with the anticipated high-pressure loading. For this reason, alternative armor grade aluminums were chosen with a thickness constraint. Aluminum 2024-T3 and 7075-T6 alloys are both highly available armor grade aluminums with the desired. Aluminum 2024-T3, as previously mentioned, is utilized in modern GLARE type panels and has been extensively studied in literature [21], [57]–[59]. Aluminum 7075-T6 alloy has been shown to behave similarly to the 2024-T3 grade, but with higher strengths [3]. Vo et. al. reported nearly 150% improvement in back face deflection of a 7075-T6 fiber-metal laminate under blast loading when compared to a similar laminate with 2024-T3 aluminum**.** For that reason, it was decided the 7000 series alloy was better suited for a blast loading application.

The hybrid panels were constructed with a 2.3mm layer of aluminum 7075-T6 alloy. At the interface of the aluminum and PET composite, a layer of 1mm Plexus MA310 methacrylate adhesive bonds the two respective material systems together. Due to the lack of symmetry and differences in the coefficients of thermal expansion in the material panel, the PET composite could not be hot pressed directly into the aluminum. After the melting point of the PET was reached, and cooling of the composite began, crystallization within the PET began and solidify the composite at a higher relative temperature. As the PET would cool further, it would carry more thermal load from the aluminum that was contacting more quickly than the composite due to its higher coefficient of thermal expansion. Upon cooling to room temperature, the resulting material panel had large amounts of interfacial stress leading to a warped material panel and even material failure as the composite would delaminate from the aluminum. By including an adhesive layer, the material panel could be processed at room temperature leading to a stress-free bond in the material joint. The PET composite was a 3.175mm thick 0/90 cross ply laminate. The total panel thickness was 6.475mm.

The monolithic aluminum plate was 3.175mm of thickness as this was the 7075-T6 stock that was most like the weight per square as the hybrid panel was estimated to be.

3.3 Material Manufacturing for Blast Panels

Manufacturing was done on a Grimco Press Model D150-9-22 136-metric ton heated press outfitted with a chiller.

Figure 34 Hydraulic Hot Press

A 6.35mm by 610mm x 610mm polished aluminum plate acted as the lower and upper caul plates. When manufacturing hot formed thermoplastic structures using a mold system (Figure 35), a release coating or film is often needed to ensure the part can be removed without damage. For consolidating the flat test panels in this study, 0.0508mm thick polyimide film (Kapton®) was utilized as a release ply between the PET / GF laminates and the aluminum platens. The polyimide film was rated with an operating temperature of up to 400°C, which was well above the processing temperature of the PET composite used in this study. The release film was cut into 325mm x 325mm squares and allowed to overhang the edges of the platens to ensure that no excess PET was allowed to flow outside and touch the platens. Another 6.35mm x 610mm x 610mm aluminum plate was placed on top of the polyamide release film and lower platen. This aluminum plate had a 308mm square hole cut out of its center and was used as a bump stop for its final consolidation thickness. Polyamide tape was placed around the perimeter to ensure the edges remained non-stick. Thirteen layers of the Toray prepreg PET unidirectional tape was then stacked on top of the aluminum in an alternating cross ply fashion as [0/90/0/90/0/90/0/90/0/90/0/90/0]. Two separate width tapes, 140mm and the original 165mm unmodified width were used to create a single unidirectional ply of 305mm width without having any overlap.

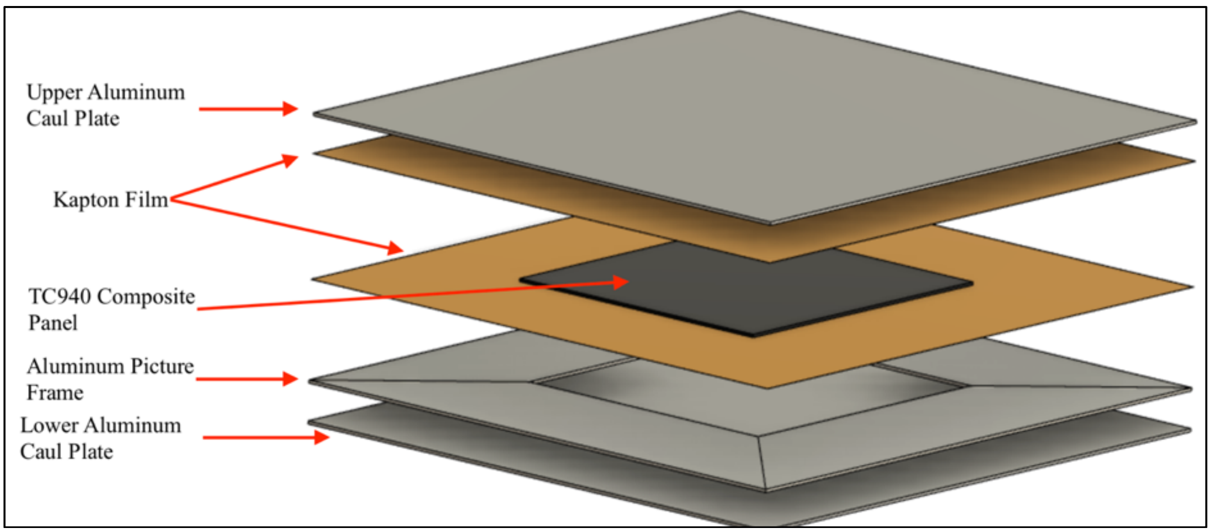

Figure 35 Manufacturing Stack Up [60]

After putting the mold together as shown in Figure 35 inserted between the platens of the press. The mold was then bound by another top and bottom layers of Kapton to prevent the mold from sticking to the platens of the press if resin was to leak. The hydraulic press had a maximum clamping force of 136 metric tons, maximum operating temperature of 400°C, programmable heating, and cooling cycles, and both air and water cooling. It should be noted that when cooling down from 400°C to 315°C, only air cooling is available, per manufacturer's recommendation.

The manufacturing cycle was as follows: (i) Preload at 31.75 metric ton force, (0.83MPa) (ii) heat to 265°C (maintain 31.75 metric ton force), (iii) dwell at 265°C for 15 minutes (maintain 31.75metric ton force), and (iv) cool to 52°C (maintain 31.75metric ton force until cool). Cooling began at 265°C with air and water cooling to allow platens to cool without over pressurizing from excess water vapor. Pure water was then pumped into the platens at a temperature of 21°C. From this point, a cooling rate of 15°C/min was achieved. After removing the polyamide film from the composite laminate, the panels were labeled, and the thickness was measured as a verification step to make sure that proper consolidation was achieved. Further details of manufacturing followed were detailed in previous conducted research [60].

Plexus MA310 methacrylate adhesive was used to adhere the composite to the aluminum front plate. Surface preparation techniques included consistent grit blasting of the aluminum substrate to mechanically etch the surface for maximum mechanical bonding to the substrate. After grit blasting, isopropyl alcohol was used to degrease the surface and remove any grit blasting residue. To prepare the PET/GF substrate, 400 grit sandpaper was used to lightly rough the surface of the composite ensuring to not over rough the surface and damage the underlying fibers. Though, the methacrylate had good adherence to the PET, its adherence to glass was much higher so removing the surface skin of PET allowed for maximum bonding to the embedded glass fibers. After the light sanding, isopropyl alcohol was used to clean the surface and remove any contaminants. To ensure quality control in bonding consistency, weights of the constituent materials were tracked. Pre-bonded weights of both the aluminum and the composite were recorded before and after bonding to estimate the amount of adhesive used within the bond line. To bond both substrates, steel rod was placed along the edges of the panel. The steel rods set the bond line thickness of the panels. The rods were placed on the outside edges of the panel as these would be removed so the panel can fit within the shock tube. The steel rods had a diameter of 1mm. Adhesive was applied to the substrates and spread with a glue spreader until a consistent layer of adhesive was applied. The two substrates were merged and placed into a mold that held both firmly in place but allowed excess glue to flow out of the material without thinning the bond line. The panels were then weighed a final time and the final bond line thickness was estimated and compared to the other panels within that lot. The final bonded panels were then cut via bandsaw for final fitment inside the blast tube. Mounting holes were cut using diamond coated abrasive hole saw. Precautions were taken in both cutting and drilling to ensure a healthy composite specimen was produced without inducing damage initiating defects.

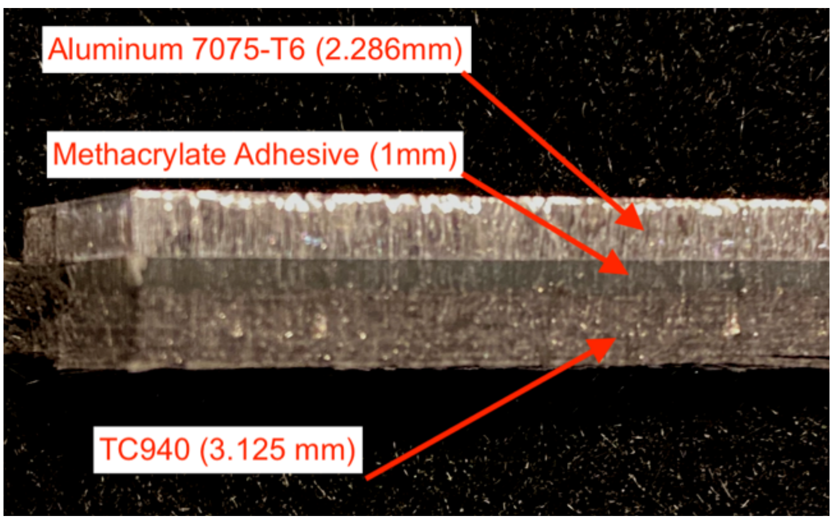

Figure 36 Cross Sectional Cut Over Manufactured Hybrid Panel

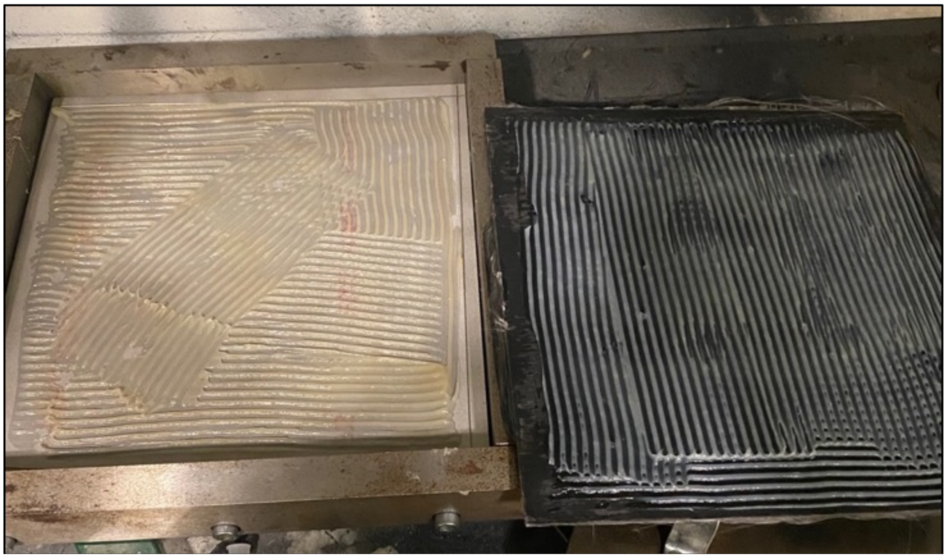

Figure 37 Glue Application

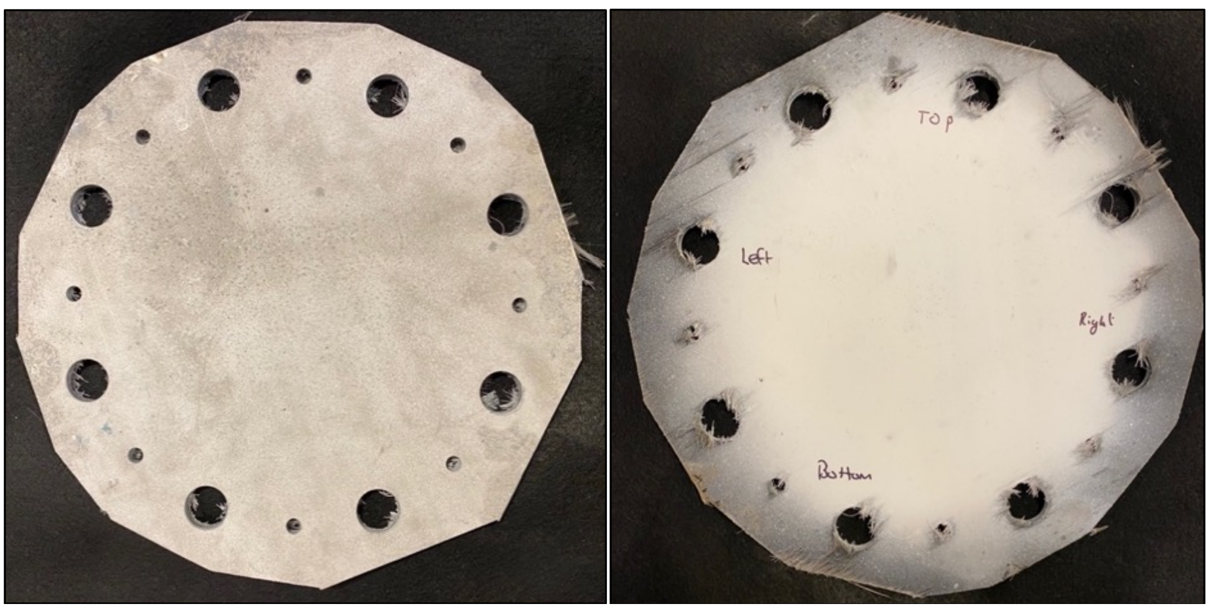

Figure 38 Untested Material Panel

Chapter 4 Experimental Results

The shock tube blast simulation experiments were conducted under the exact same initial conditions as the pressure profile characterization detailed in Table 3. A series of tests were conducted 23mm away from the nozzle assembly including the shock wave attenuator and piston plugs. High speed imagery and fringe projection was used to calculate the dynamic deflections of both the monolithic aluminum plate and the composite-metal hybrid panels. With the fringe projection and lighting set up, 10,000FPS was obtained and deemed suitable for deflection monitoring under the pressure loading.

When comparing the dynamic behavior of both the monolithic and hybrid panels, excess vibration was observed in the mounting system for the material as well as the fringe projector and camera system. Though the images were clear and able to be analyzed under fringe projection, the integrity of the data remained in question as the specimen, high speed camera and fringe patterns were moving independently. However, the system did not register the vibration until roughly 5ms after the specimen was already undergoing deformation. Data captured between the moment of first pressure loading impact to roughly 5ms after the loading remained well preserved and able to be processed and recorded with full confidence. It is important to note that the maximum dynamic behavior was assumed to happen within this time frame which was the main objective of the fringe projection.

After the test was conducted, a validation photo was taken. The validation photos were used as a final reference image without dust and contaminant noise in the image. Though, the camera, fringe projector and tested specimen all experienced movement in the experiment, all 3 rested in their initial positions like those recorded in the first frame of the test. The validation photos were analyzed with the fringe projection system and compared to the physical measurement from a dial gauge probe. The correlations between the final fringe projection measurement and the gauge reading instilled more confidence in the fringe projection system.

4.1 Monolithic Aluminum Trials

The 7075 aluminum panels experienced consistent permanent and dynamic deflections and experienced no rupturing or excess damage of the aluminum plate. The permanent deflection was recorded via dial gauge probe when the sample was fully clamped in the mounting test fixture as well as when it was removed. The measurements showed no difference in deflection measurements when the samples were removed from the clamping fixture. The average maximum permanent deflection experienced amongst the 4 trials was 4.96mm with a standard deviation of 0.06994mm.

Figure 39 Typical Deformation Characteristic of Monolithic Plates

Fringe projection analysis was conducted on the high-speed imagery from the Phantom camera. Figure 40 -Figure 42 depict the fringe projection process. Figure 40 illustrates the raw images captured by the phantom camera The left image is the aluminum sample just before the pressure load and the right is at peak deflection. Figure 41 is the normalized images of the ones depicted in Figure 40. The images then underwent the fringe projection process, and a contour map was revealed (Figure 42).

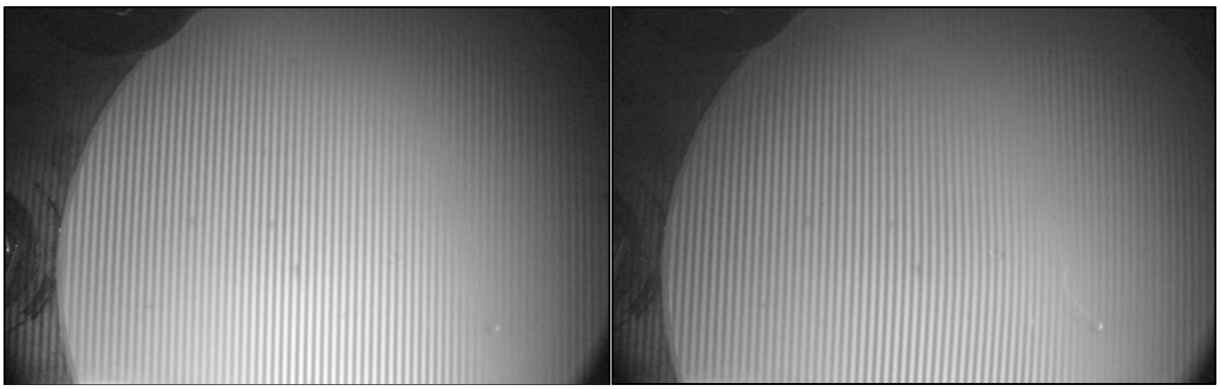

Figure 40 Fringe Projection Image (Left: Initial, Right: Peak Deflection)

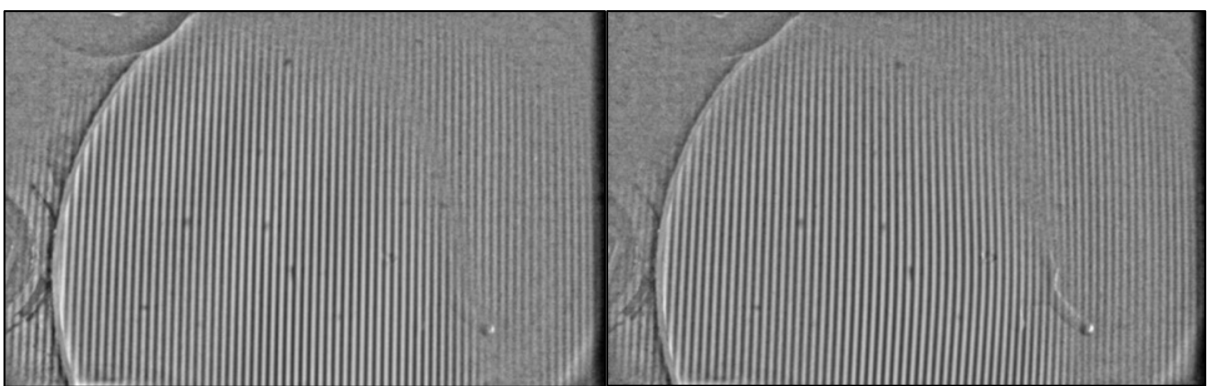

Figure 41 Normalized Fringe Projection Image (Right: Initial, Left: Peak Deflection)

The contour map reveals a dome like deflection profile that is consistent and symmetric revealing a centered loading of the pressure. A cross sectional profile was analyzed from the edge of the contour map to the center of maximum deflection. The profile was then plotted and used to characterize the deformation at peak and permanent deflections. The peak deflection profiles reveal a consistent global deformation without any areas of higher relative deflection.

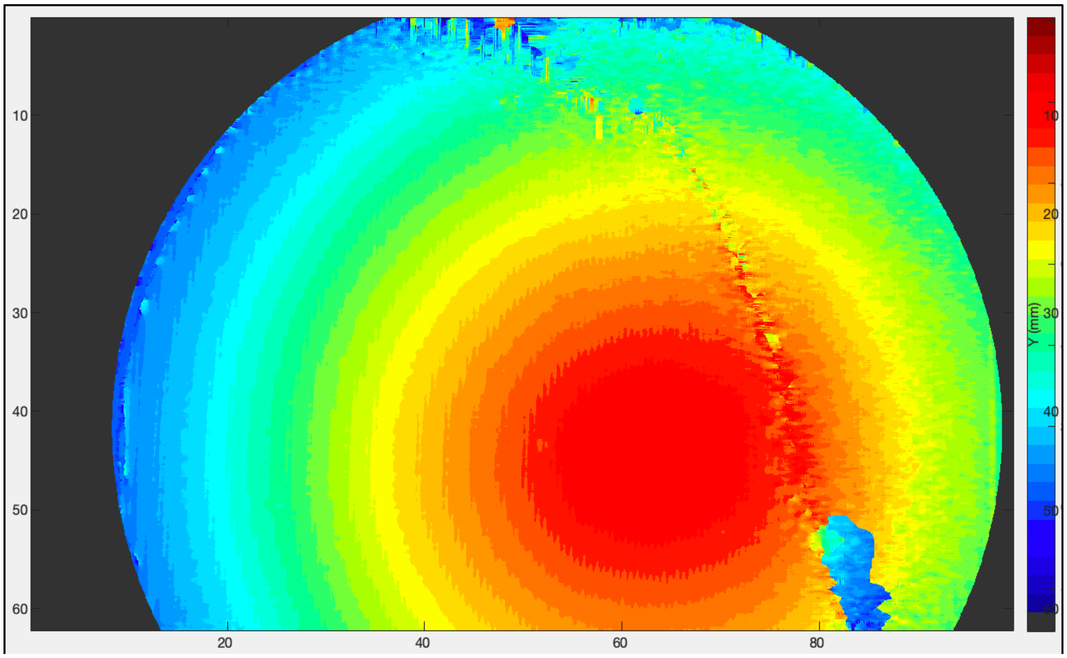

Figure 42 Fringe Projection Contour Map of Peak Dynamic Deflection in Aluminum Plate 4

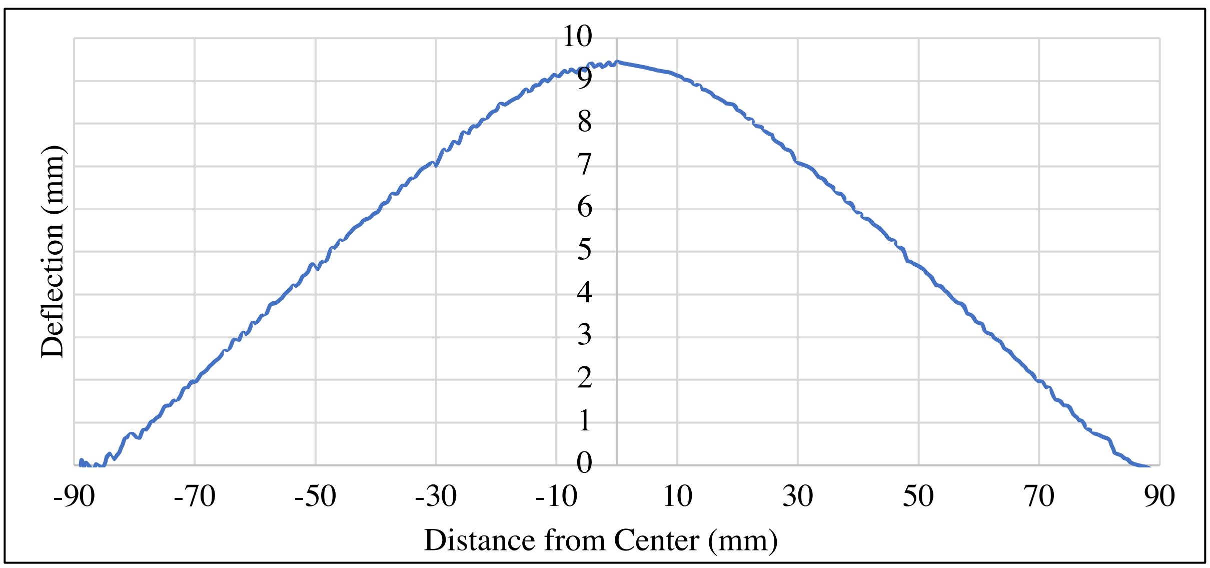

Figure 43 Cross Sectional Contour of Dynamic Deflection of Aluminum Plate 4

Unlike the peak deflection profile, the permanent deflection profiles reveal greater inconsistency in that the deflection increases more toward the center of the profile than the edges. Though kept at a distance and allowed to expand, the pressure films indicated a more localized area of high pressure loading towards the center of the material sample. Due to a more localized nature of the load, higher stresses and thus, higher stains were experienced during peak loading. As the material relaxed and rebounded, the excess strain accumulated within the center of loading creates the "bulging" area within the center of the plate.

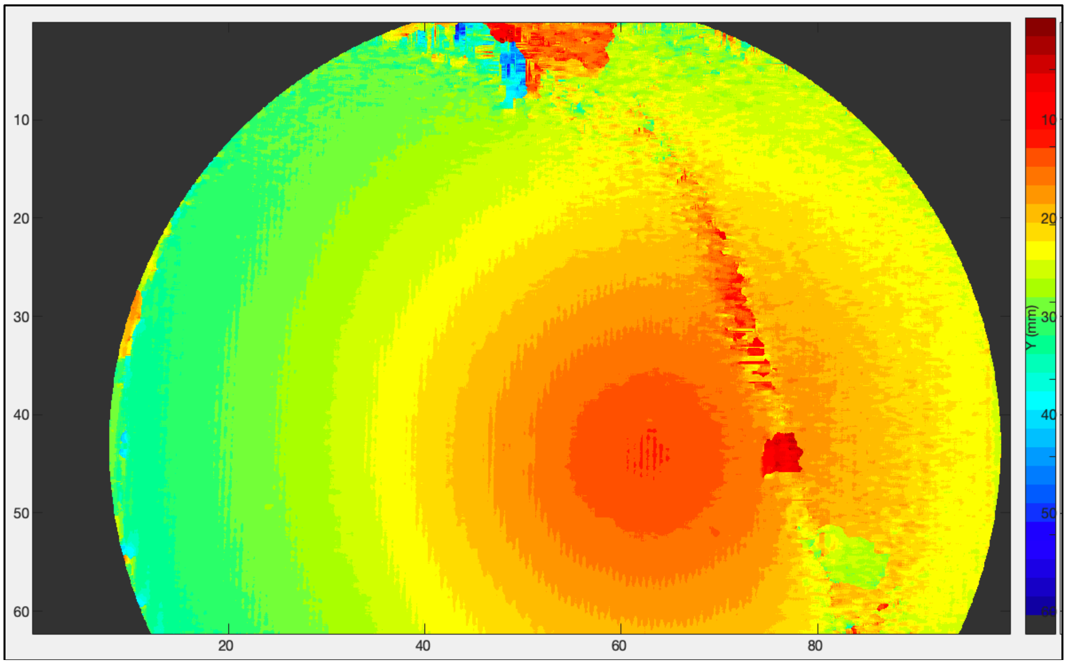

Figure 44 Fringe Projection Contour Map of Permanent Deflection in Monolithic Aluminum

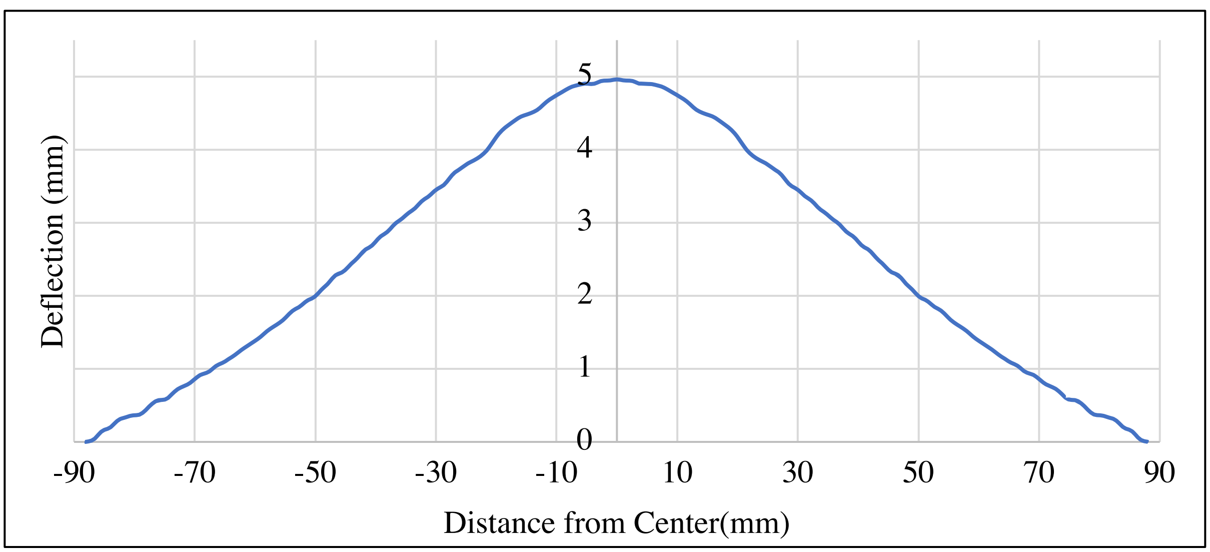

Figure 45 Cross Sectional Contour of Permanent Deflection of Aluminum Plate 4

As expected, the deflection history of the aluminum reveals the maximum deformation occurs within the peak loading (0-2ms). The average peak dynamic deflection for the aluminum was 9.89mm with a standard deviation of 0.254mm. As the pressure load is reduced, the plate elastically oscillates with lower deflection, until the plate is at rest. This shows that at maximum dynamic deflection, a combination of both plastic an elastic deflection can be observed. This is due to the strain hardening phenomena. As the aluminum is deformed greater than its original plastic limit, the failure envelope is shifted. Due to the shifting of the failure envelope, plastic strain is accumulated. As the load is reduced, the stress state of the material retreats within the elastic regime within the failure envelope and the material relaxes to it its final deformed shape as the load is eventually removed.

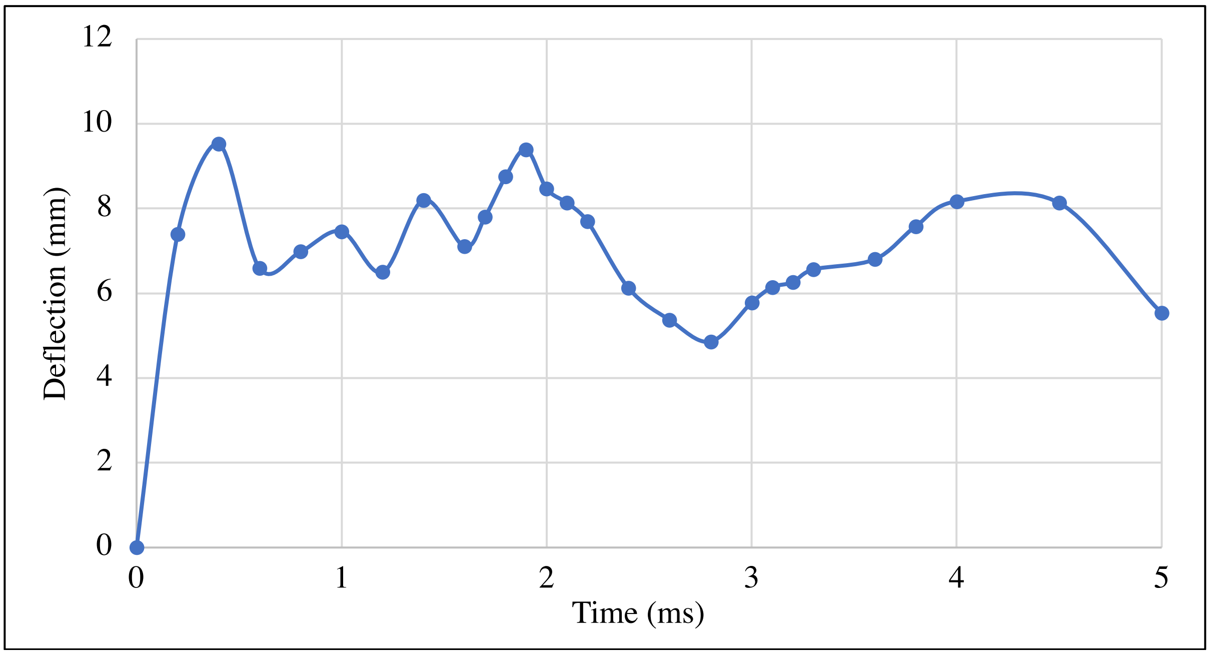

Figure 46 Deflection-Time History Aluminum Plate 4

Table 5 Deflection Data for Monolithic Aluminum

Test Object ID	Permanent Deflection	Dynamic Deflection
7075AL1	4.95mm	NA
7075AL2	4.87mm	10.03mm
7075AL3	5.03mm	10.12mm
7075AL4	5.00mm	9.54mm
Average	4.96mm	9.89mm
Standard Deviation	0.06994	0.254886

4.2 Composite Metal Hybrid Panel Trials

The composite-metal hybrid panels experienced consistent permanent and dynamic deflections. A representative deflection-time history from test object HP5 can be seen in Figure 53. The panels observed plastic deformation in the 7075 aluminum and delamination in the composite. Ultrasonic testing was conducted on the delaminated panels to obtain damage characterizations.

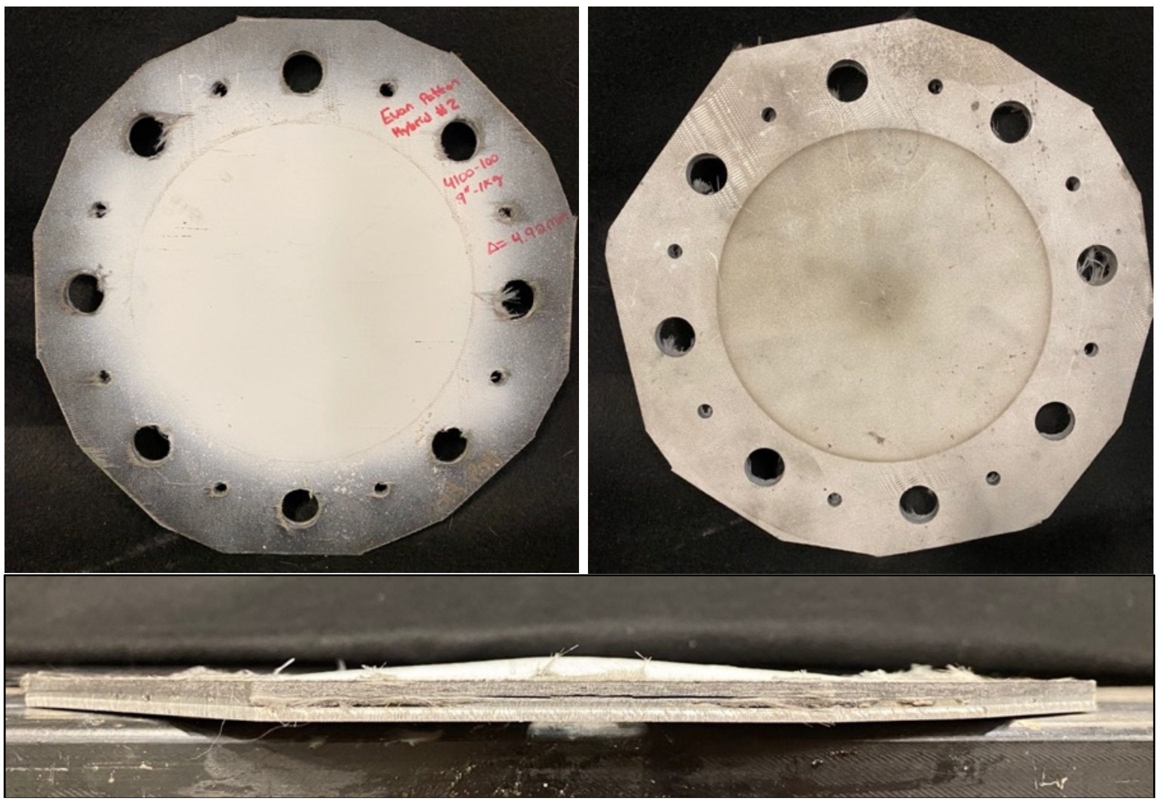

Figure 47 Typical Damage and Deflection Characteristics of Hybrid Panel

The fringe projection process for the hybrid panels was identical to that of the monolithic plates. The images were taken, normalized and fringe analysis was conducted to obtain deflection measurements throughout the shock tube experiment. The contour maps were then used to obtain cross sectional deflection profiles so the peak and permanent deflections could be analyzed. It should be noted that the cross-sectional profiles were taken in the direction of the fibers on the backside of the panel. It was assumed that a 0/90 layup could cause deflection abnormalities if analyzed across the fibers in a direction different than parallel or perpendicular.

The peak deflection profiles reveal noteworthy insights into the behavior of the composite panel. Roughly 50mm from the center of the plate, there is a point of slight inflection in the deflection profile. This area of deflection inconsistency was assumed to be attributed to delamination within the composite. Due to the localized nature of the loading, a higher stress was experienced within this area. The high stress would cause a high interlaminar shear causing possible delamination.

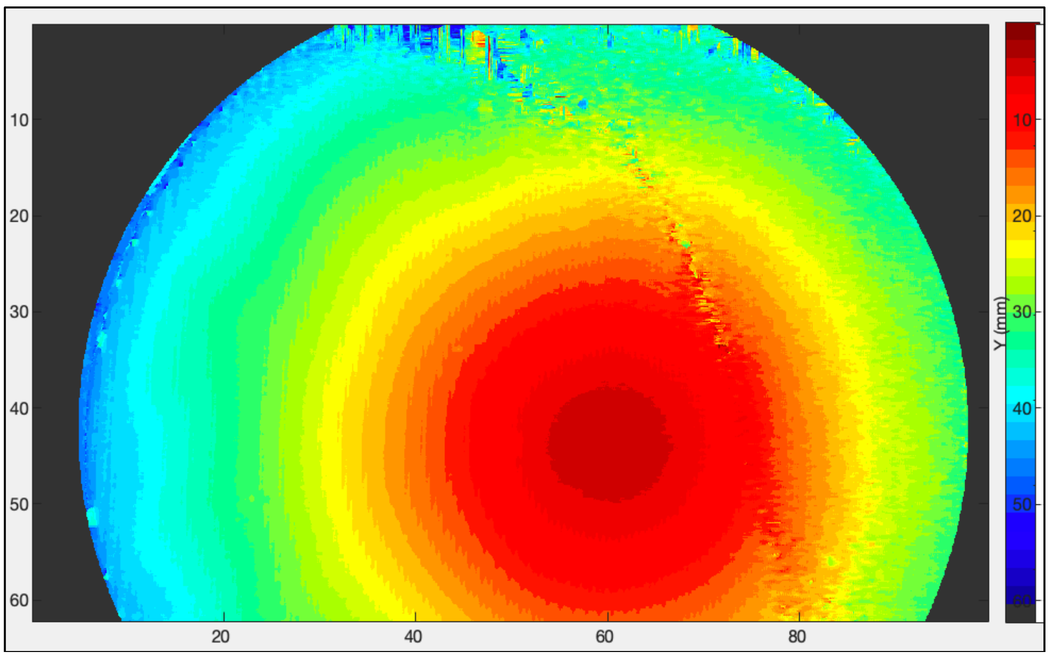

Figure 48 Fringe Projection Contour Map of Peak Dynamic Deflection in HP5

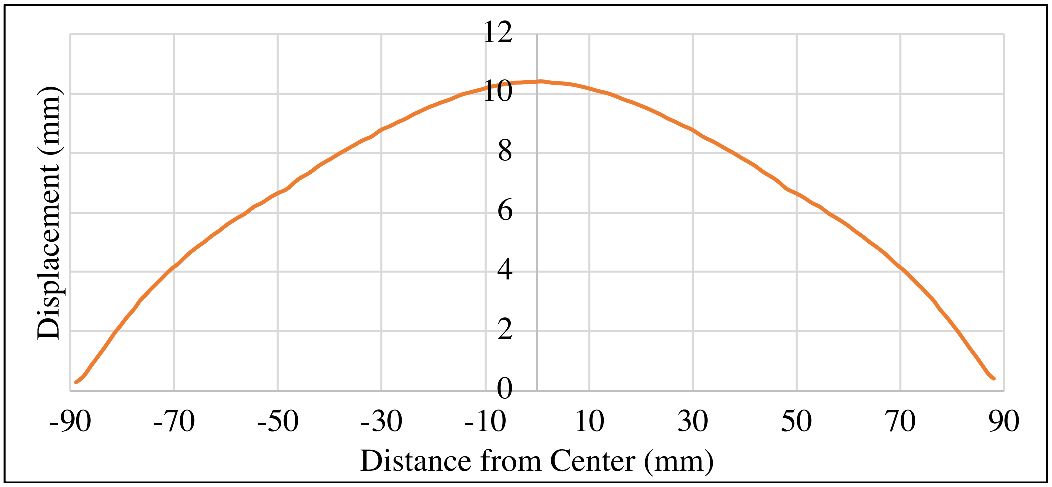

Figure 49 Cross Sectional Deflection Map Through Peak Deflection

The permanent deflection profiles revealed more pronounced bulging toward the edges around 70mm from center. This can be attributed to delamination and poorly consolidating within the composite at the end of the loading.

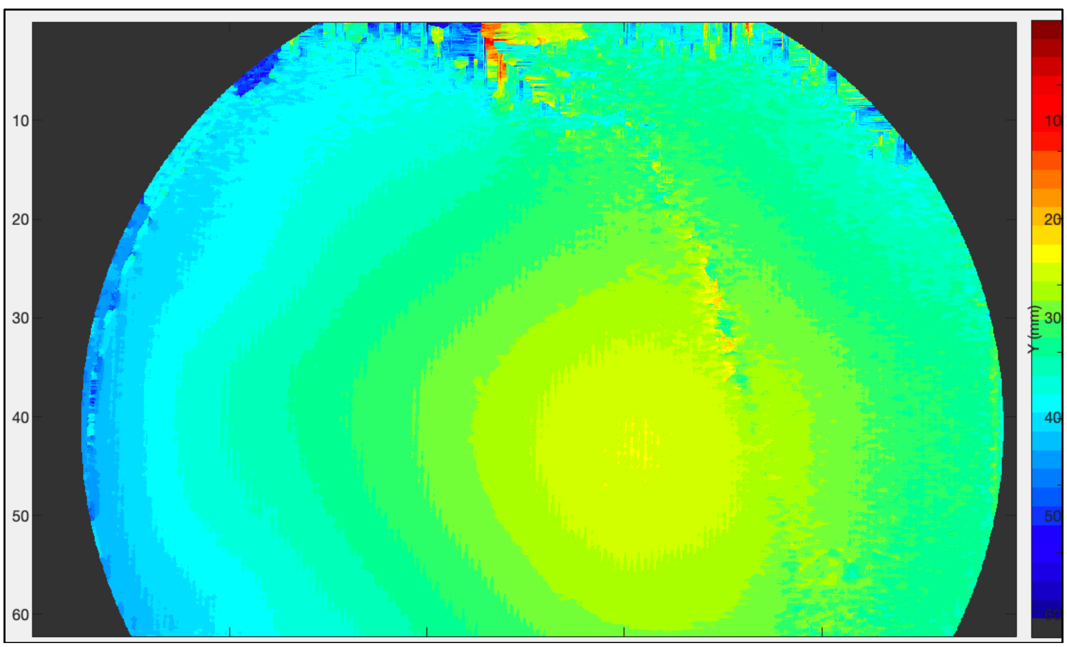

Figure 50 Fringe Projection Contour Map of Permanent Deflection in HP5

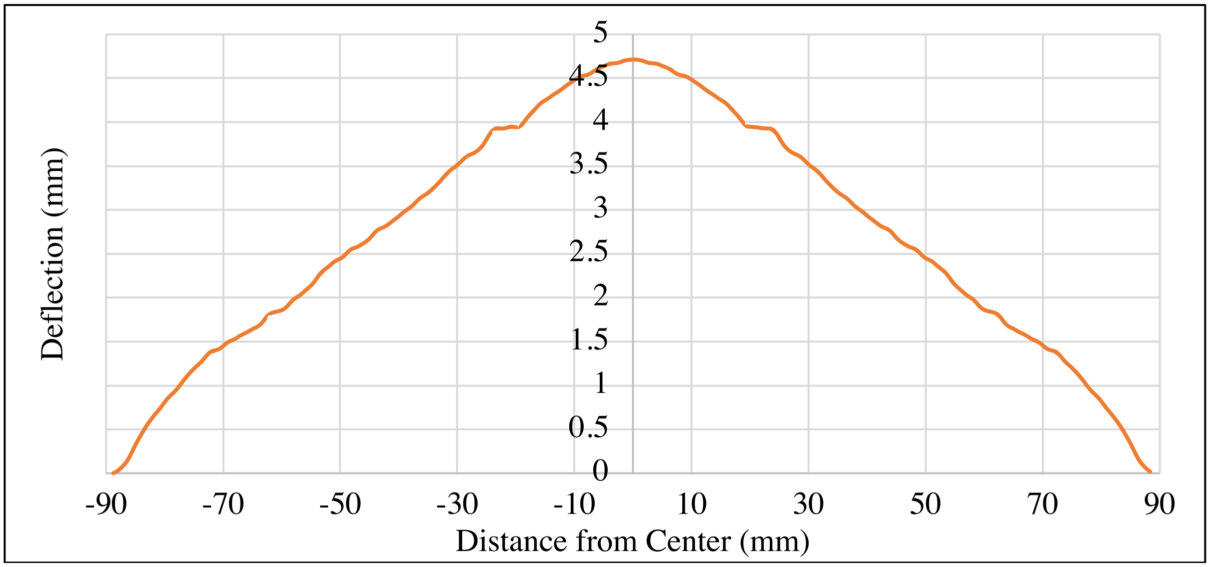

Figure 51 Cross Sectional Deflection Map Through Permanent Deflection in HP5

The contour maps show dome like deflection patterns however, directional deflection “fingers” can be seen in the contour maps upon closer inspection as denoted by the dashed lines in Figure 52. These protrusions are assumed to be the result of delamination within the composite. At peak deflection, the composite is assumed to delaminate throughout the cross section to the clamped boundary. Upon settling, the composite reconsolidates and reveals the extent of the delamination as a more pronounced irregular contour is shown with a cross like delamination pattern.

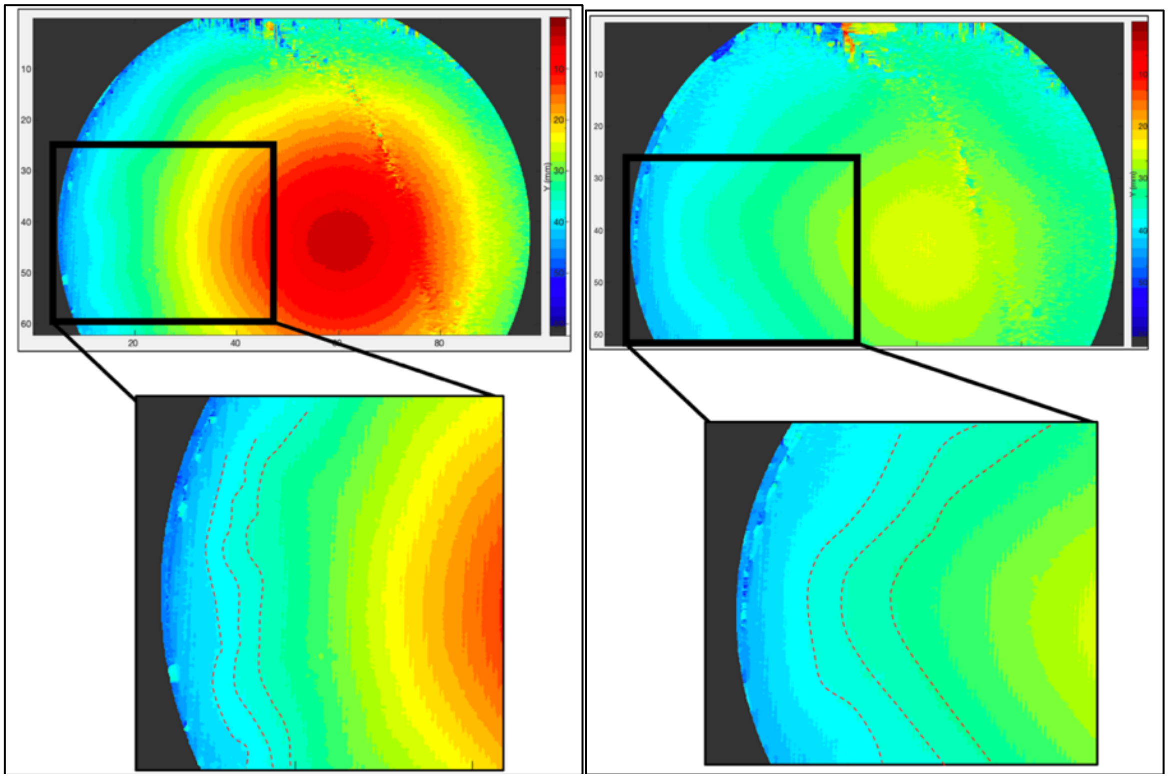

Figure 52 Deflection "Fingers"

As expected, the deflection history of the hybrid panels revealed the maximum deformation occurred within the peak loading (0-2ms). The average peak dynamic deflection for the hybrid panels was 10.95mm with a standard deviation of 0.3952mm. As the load is reduced, and the material relaxed to it its final deformed shape the average maximum permanent deflection experienced was 4.87mm with a standard deviation of 0.1896mm.

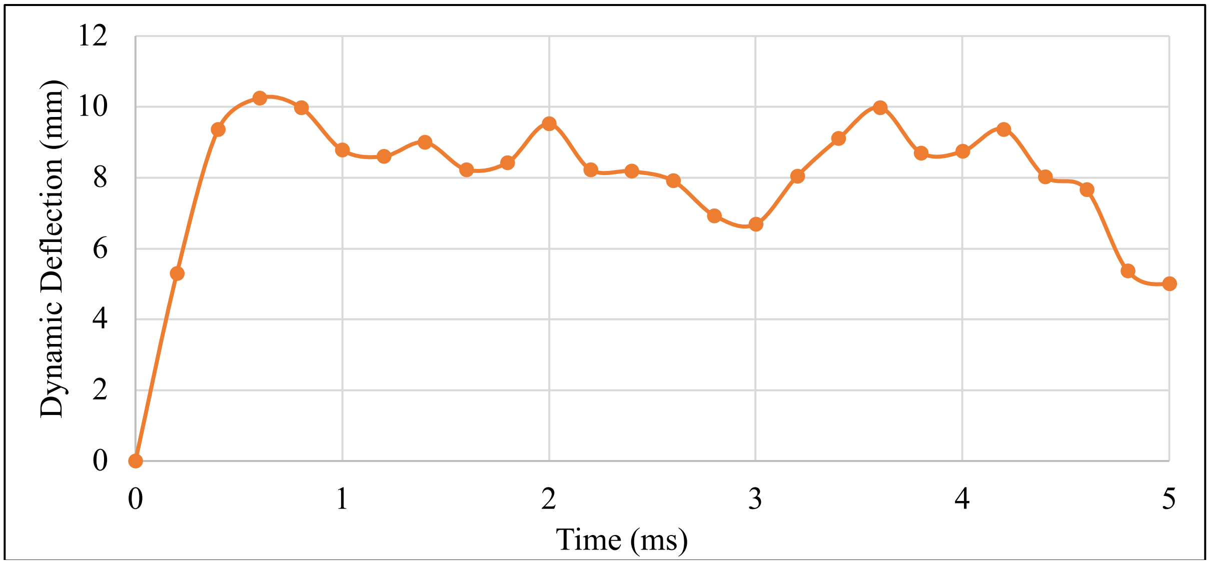

Figure 53 Deflection-Time History for HP5

Table 6 Hybrid Panel Deflection Data

Test Object ID	Permanent Deflection	Dynamic Deflection
HP1	4.97mm	11.09mm
HP2	4.92mm	11.23mm
HP3*	6.47mm*	12.06mm* (Cracking Observed)
HP4	5.00mm	11.10mm
HP5	4.59mm	10.36mm
Average	4.87mm	10.95mm
Standard Dev	0.1896	0.3952

4.2.1 Nondestructive Evaluation: C-Scan

Non-destructive analysis was conducted on hybrid 5 panel without having to destroy the sample to obtain through thickness damage characteristics. Two types of C-Scanning techniques were utilized: through-transmission and pulse-echo. Initial spot conducted tests with pulse-echo revealed extensive delamination within the entire unclamped area, however individual ply data could not be obtained due to the attenuation within the material. When scanning a healthy sample of pure composite, it was seen that the material is highly attenuative. The disruption of the pulse-echo signal is due to the inhomogeneous nature of the hot-pressed composite. Being made of multiple materials (fibers and matrix) the difference in the speeds of sound within each respective material are vastly different causing attenuation. Not only is the signal disrupted due to the fiber inclusions within the composite, but the fiber orientation and localized randomness also causes the signal to be disrupted. Under the manufacturing process conducted on the blast panels, the fiber bundles drifted as the matrix was thermoformed into a thin composite sheet. This fiber drift, though slight, is randomized enough to lose material structure and further scatter the signal. Though the pulse-echo technique failed to provide a ply by ply damage characterization and only showed complete delamination somewhere within the composite, the technique was used in obtaining a deflection contour plot of the material. Knowing the speed of sound a wave propagates in water and the time of travel from the pulse to the recorded echo, a relative distance from the sample surface to the pulse-echo head can be plotted and thus, obtaining a surface profile. Though the resulting contour map was noisy and low resolution, the general contour shape and peak deflection value was representative of the contour map from the fringe projection data. Peak deflection measurement from the pulse-echo was found to be 4.96mm relating to an 8% deviation from the measured value of 4.59mm for hybrid panel 5.

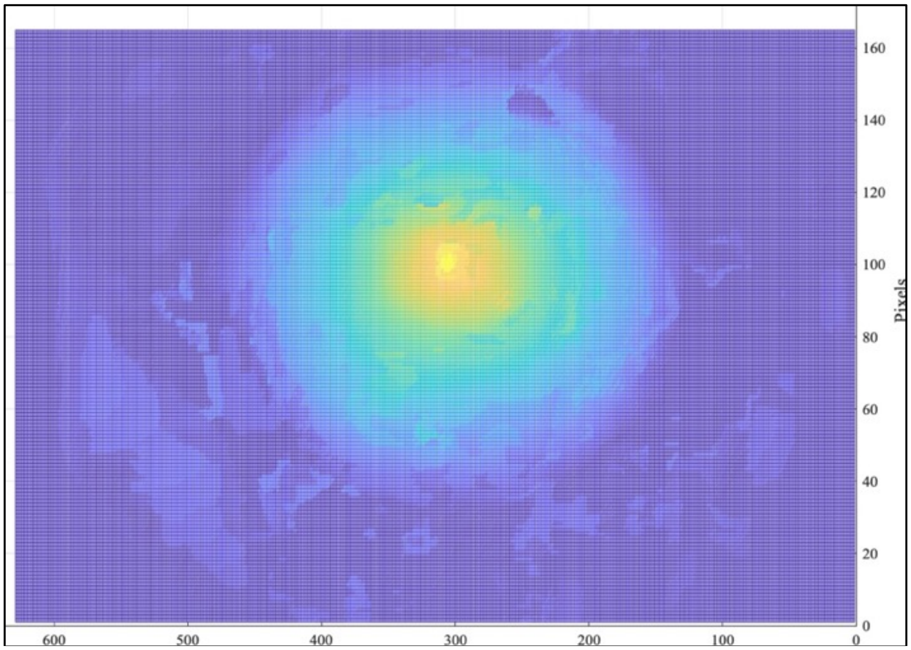

Figure 54 Pulse Echo Deflection Contour Map

To receive a better representation of the internal damage, through-transmission scans were conducted. A through-transmission scan pulses a signal through the composite, on the opposite side, there is a receiver recording the transmitted energy and the time of flight for the signal. An intact sample will yield a higher transmitted energy and a faster time of flight. As a sample is damaged, air begins to arise in the areas of fiber pull out, delamination, matrix cracking etc. The air has a much slower transmissibility of the wave thus, attenuating the propagating signal and revealing the damaged area.

Two through-transmission scans were conducted on hybrid panel 5 and a healthy sample. The damaged sample revealed nearly no transmitted energy throughout the unclamped section as shown in Figure 56. The areas of low transmitted energy correlates to areas of heavy damage and delamination. Along the outside of the loaded section and in the area clamped by the mounting hardware for the shock tube system, the transmitted energy reveals that the sample is relatively intact. Localized areas around the drilled holes and those close to the edge of the blasted area reveal damage, however, due to the nature of the transmission devices, these areas can become blurred due to the large area of sonication.

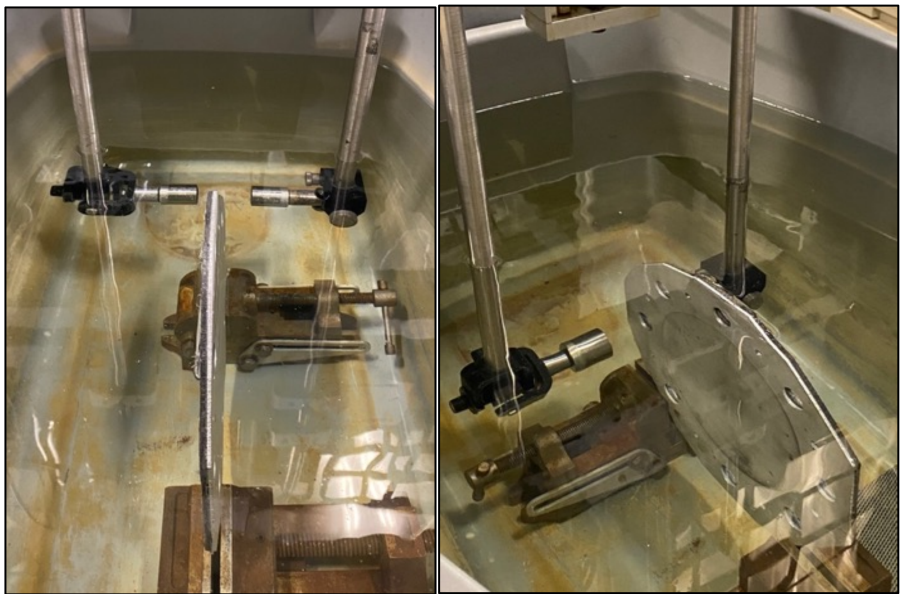

Figure 55 C-Scan Through-Transmission Process

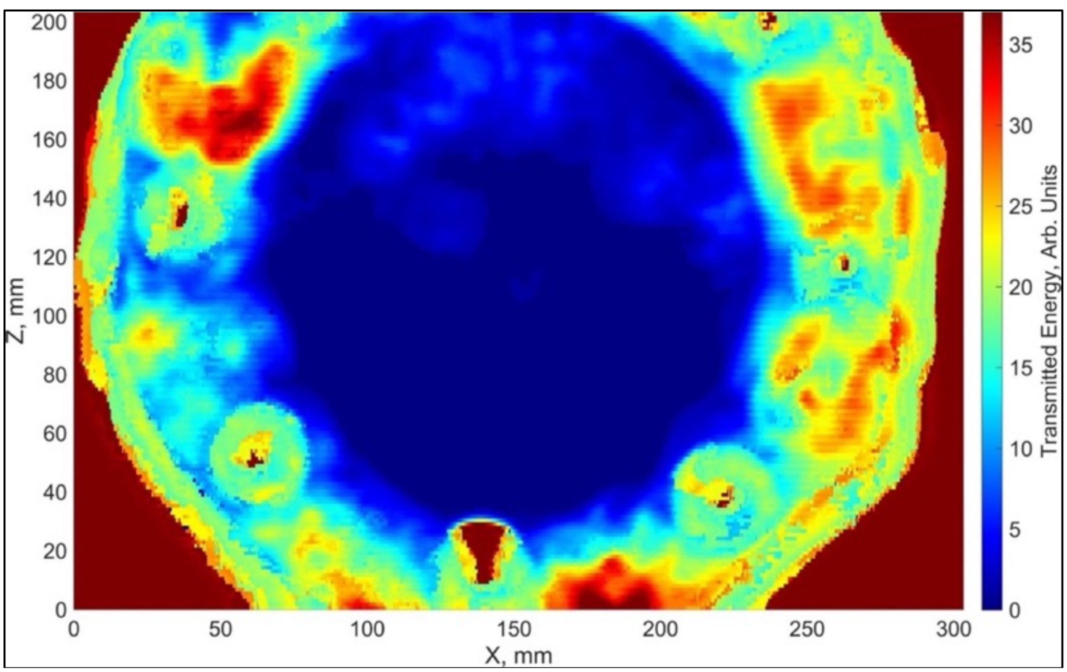

Figure 56 Though Transmission C-Scan Damaged Sample Plotted Energy

The hybrid panel was then cut to validate the interior damage. The sample was carefully cut with a diamond tipped wet saw along the center cross section across the area of peak deflection. The cross sectional cut revealed heavy delamination throughout the entire thickness of composite. Nearly all plies in the thickness experienced some extent of delamination.

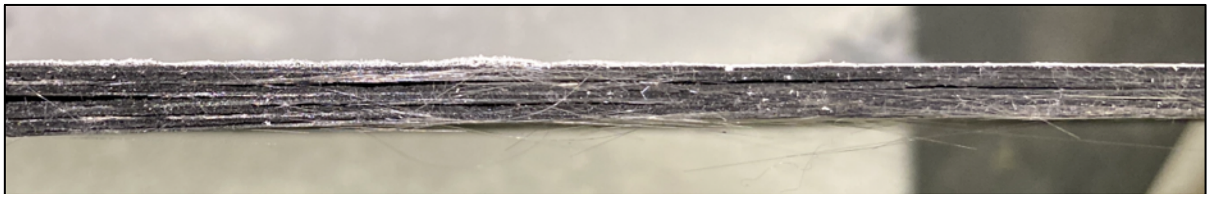

Figure 57 Cut Cross Section of HP5 Depicting Delamination

The healthy sample revealed higher amounts of transmitted energy throughout the entire sample as shown in Figure 58. The areas in red show good transmissibility and those in blue show areas of weaker transmissibility. Due to the manufacturing process of the composite, this type of randomness in transmissibility is expected as fiber rich, matrix rich, over and under consolidated areas can all cause changes. Furthermore, entrained air within the adhesive layer could cause further lack of transmissibility within the composite. With the manufacturing techniques used in the fabrication of the hybrid panels, this result is satisfactory.

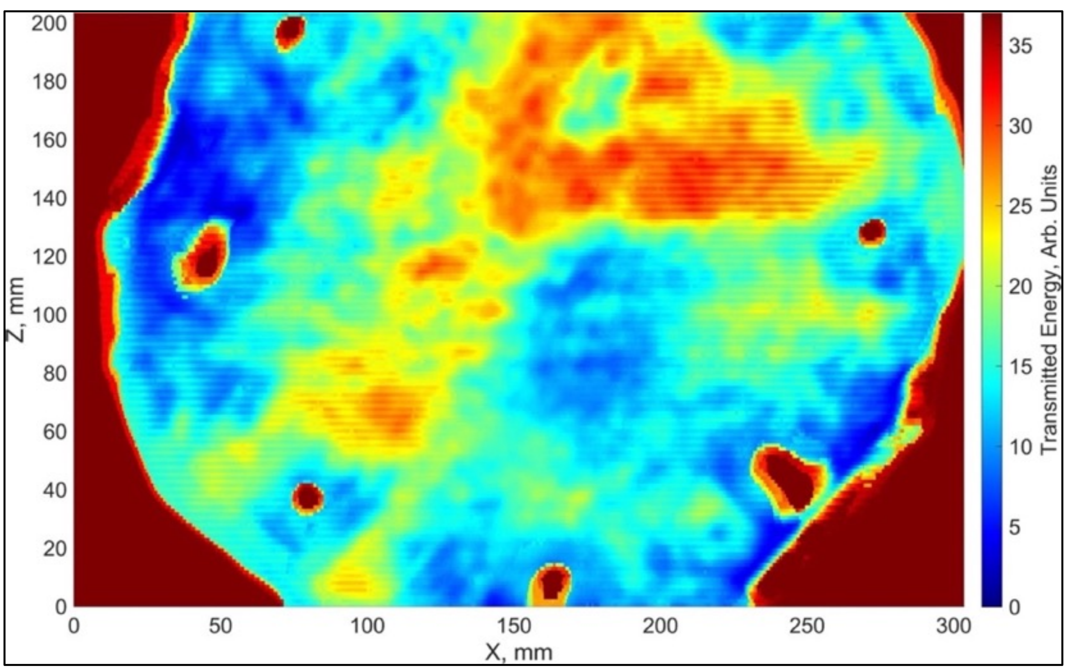

Figure 58 Though Transmission C-Scan Healthy Sample Plotted Energy

4.3 Comparative Analysis

When analyzing the validated deflection data, both the aluminum and hybrid panels showed deflections much higher than their permanent deflections. The aluminum plates experienced an average maximum dynamic deflection of 9.89mm and a permanent deflection of 4.96mm. The hybrid panels experienced an average maximum dynamic deflection of 10.95mm and a permanent deflection of 4.87mm. duration between the onset of the pressure loading and the peak dynamic deflection was longer for the hybrid panel compared to the monolithic aluminum plate. During every hybrid panel test, the hybrid panels were consistently reaching their maximum deflections 0.2 to 0.3ms longer than the aluminum. Possible causes for this could be the difference in material thicknesses between the monolithic and hybrid panels. The hybrid panels were roughly double the thickness of the monolithic plates. Due to the high strain rate loading, there could have been lag within the hybrid panel thickness resulting in a delayed response. Additionally, moments of delamination could have led to delays in the moment of maximum peak delamination.

The aluminum and hybrid panels seem to mirror the general trends of each other's deformation history even though the material systems are of different compositions. Given the post damage analysis on the hybrid panels showing complete delamination of the composite, it was assumed after peak deflection, the composite in the hybrid was delaminated in all plies aside from the adhesive and first composite ply interface and offered minimal structural support for the material panel. From this point, the material system could be thought of as two individual pieces of material, the plastically deformed aluminum, adhesive and 1st composite ply in one material system, and the delaminated composite consisting of plies 2-13 in the other material system. As the panel reacted to the pressure loading, the debonded aluminum acted as the governing response system with little to no influence from the delaminated composite. Due to the independence of the materials, the aluminum could behave similar to the monolithic plate. The greater deflection in the hybrid system could be attributed to the damaged composite loosely moving in response to the underlying debonded aluminum.

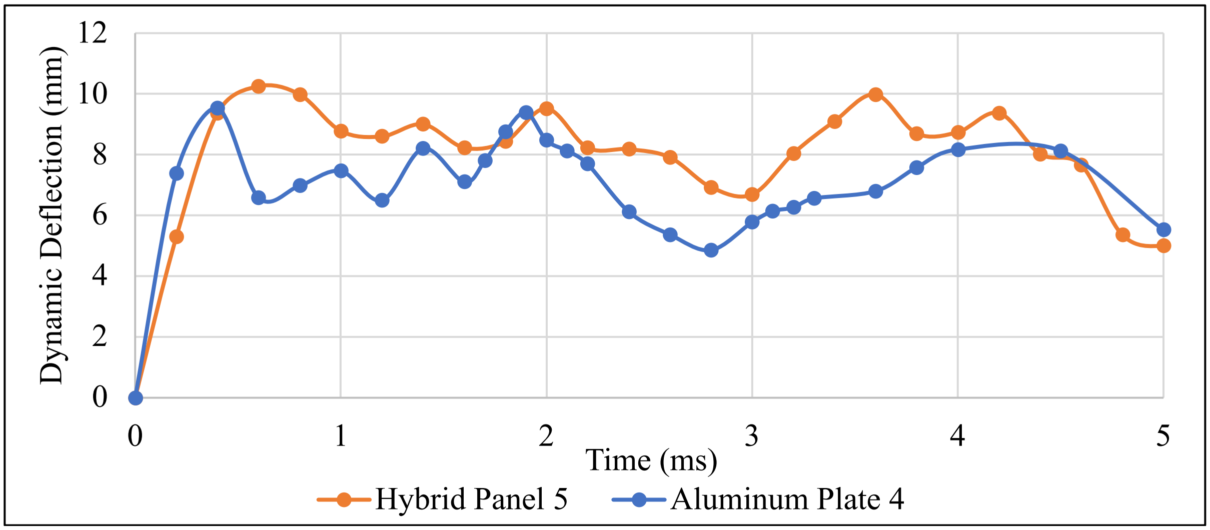

Figure 59 Dynamic Deflection Time History Data

When assessing the deformation characteristics of both peak and permanent deflections for the hybrid and monolithic plates, keen differences can be noted. The composite sees a global higher deflection in all locations of the panel. This was assumed to be due to the delamination experienced within the panel. Comparing the permanent deflections, another unique observation can be drawn. The monolithic aluminum plate is observed to have a more localization of deformation where the composite remains broad with additional bulges on the edges near the clamped boundary. As previously mentioned, the aluminum experienced a more localized deflection toward the center due to the higher loading in the localized are that resulted in higher amounts of plastic flow. Areas more distal from the center of loading experience less stress and thus, yields less plastic flow. The result is higher permanent deformation toward the center and less toward the edges of the plate creating the localized area of high deflection. The composite on the other hand has no distinct yield point and does not plastically flow. However, the composite delaminated. After delamination, the composite compacted back onto the underlying deformed aluminum. When settled, the composite buckles near the areas of constraint i.e. the edges of the clamped fixture.

Due to both the peak and permanent deflections being similar, it is convenient to directly compare the hybrid and monolithic plate performance. Though the hybrid panels experienced slightly smaller deflections (4.87mm compared to 4.96mm), the weight per square meter was 34.1% higher than that of the monolithic plate (88.9kg compared to 125.4kg). Moreover, the dynamic deflections of the hybrid panels were larger than the monolithic plates (10.95mm compared to 9.89mm).

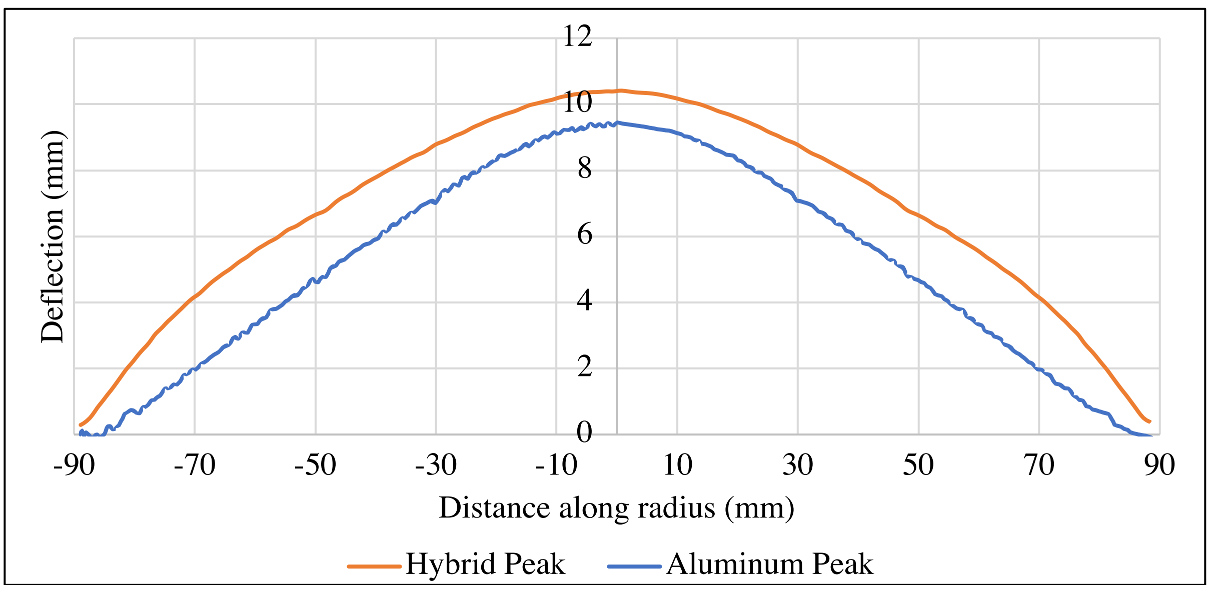

Figure 60 Peak Deflection Cross Section Comparison

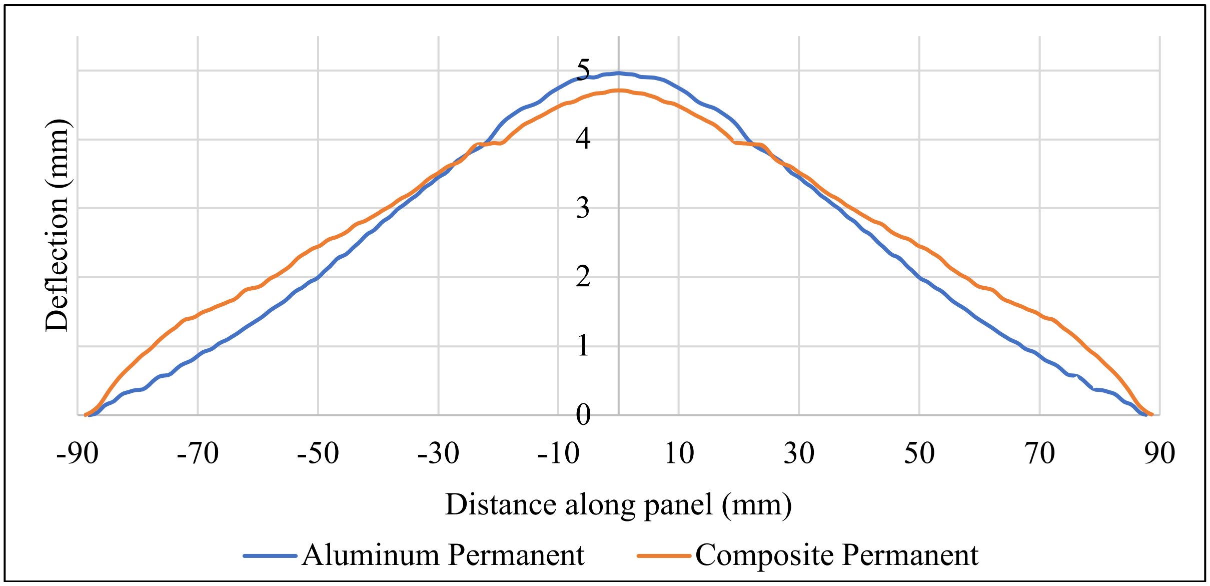

Figure 61 Permanent Deflection Cross Section Comparison

Chapter 5 LS Dyna Modeling

5.1 Shock Tube Model

To obtain accurate pressure loadings in the LS dyna model, the material model needs to be well characterized for the pressure loading. Peak pressure, over pressure duration time and area of blast load all need to be considered when determining the fidelity of the model. Methodology approaches such as modeling an explosive and surrounding environment in a multi-material Arbitrary Lagrange-Eularian, MM-ALE, utilizing the streamlined LOAD_BLAST_ENHANCED material card, or a combination of the two are used commonly in Dyna for model Friedlander like pressure forms.

LOAD_BLAST_ENHANCED is the most simple method to create a free-air burst. LS Dyna recognizes a charge weight and distance away from the target and detonates the assumed TNT explosive. The blast wave is propagated through the open air and makes contact with the target. The simplicity in the model allows for a rapid blast loading computation without sacrificing accuracy when simple loading is presented. While using this card however, there is no wave reflections and thus, misses out on complex wave interactions.

MAT_HIGH_EXPLOSIVE_BURN material card coupled with ALE (arbitrary Lagrangian-Eulerian) is another blast modeling approach. The material card uses a EOS_JWL keyword to define the Jones-Wilkins-Lee equation of state parameters such as detonation velocity, density, and other afterburn constants specifically formulated for a certain type of explosive. The benefit to using this methodology is due to the tailorability of the modeling setup. The ALE implementation can capture complex wave interactions with a structure and its surrounding environment. The EOS_JWL card can expand on the incorporations of other high explosives used in the model or experiments further allowing for a more tailorable Friedlander blast form. Though this is seemingly the most accurate method to modeling an explosive event, it comes with high computational expense. In events with a large amount of explosive detonated a far distance away, the ALE elements drastically slow the simulation time down.

Coupling the multi material ALE and LBE keywords presents a third approach which captures the benefits in both models. This approach uses the LBE card to load the material that is locally bounded by ALE elements where complex wave interactions are expected. The utilization if the LBE card at a distance allows for fast computation for the area between the explosive detonation and the test object where there is no variability and reason for ALE calculation. The pressure data from the LBE detonation is read into the ALE elements the moment LS Dyna computes the interaction between the two cards and the ALE elements then are used to load the material.

Although LS Dyna is streamlined to simulate high energy events such as blasts and explosions with these methods, it is important to understand the physical differences between the CVRC shock tube and those high energy events.

5.1.1 Modeling of Gases

Though the pressure characteristics of the CVRC shock tube are all signature of a Friedlander ideal blast wave, the cause of the rapid rise and decay in pressure is not solely due to a typical strong shock wave seen in a high energy detonation. Although there is a small shock from the localized pressure instability, the pressure is caused by fluid motion and the actual density of the air. For that reason, typical LS Dyna tools and solvers cannot be used as they are designed for signature blast events in a free field setting. The fluid motion across the plate would need to be considered as the material deforms and causes changes in pressure across the plate.

To obtain the most accurate pressure loading, an Arbitrary Lagrange-Eularian (ALE) model was made of the shock tube and its mechanics (Figure 62). The ALE model represented the exact settings of the experimental pressure characterization tests.

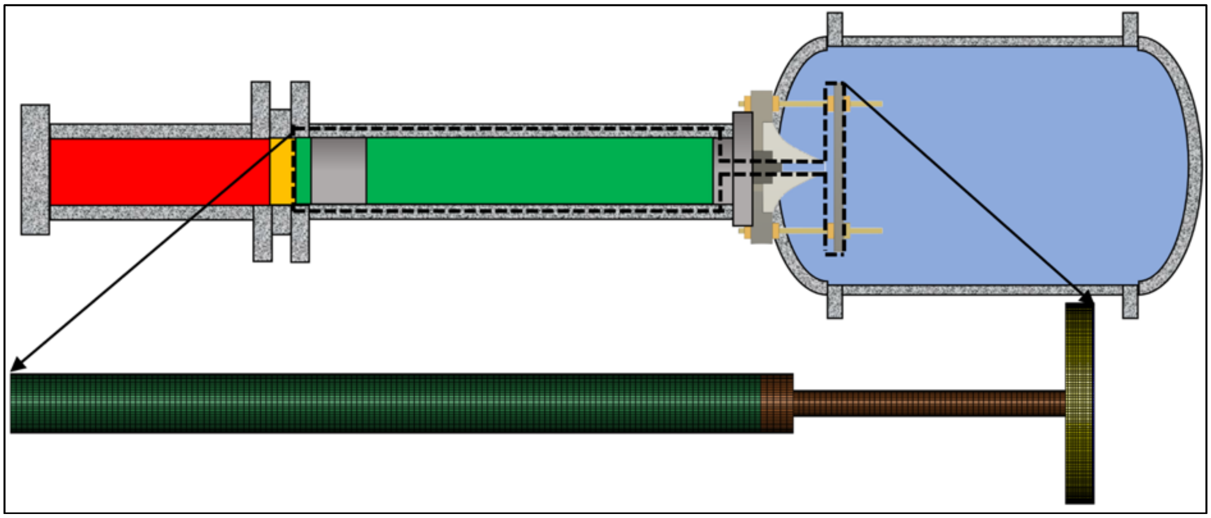

Figure 62 Detailed View Depicting LS Dyna Model Generalization

The shock tube was truncated into three sections, the area in the low-pressure chamber with the piston plugs and driven gas the ambient section in the blast nozzle including the space in front of the material section, and lastly the tested material itself. The ALE sections (low pressure chamber and ambient) utilized ELFORM=11, one point ALE elements. Equations of state and material properties were given for each ALE section. EOS_Linear_Polynomial was utilized to describe the equation of state in each ALE section of the model. This material card is extensively used to model air and was used to define the "C" parameters [61]. The C_4 and C_5 parameters are simply found by $C4 = C5 = \gamma$-1.

Ambient air was assumed to have zero external pressure. The compressed low-pressure driven gas was assumed to be near, but not exceeding the diaphragm rupture strength. With the piston starting a 735mm away (100 mm away from piston plugs in the model). Theoretical pressures were calculated using ideal gas equations. The pressure in the low-pressure chamber at time of diaphragm rupture was approximated to be 50Mpa given the compressed volume by the piston and assumed conditions within the gas. To set the initial pressure, E0, or internal energy was calculated by $E_0 = \frac{C_v T}{V_r}$ Where C_v is the specific internal energy, T is the internal temperature and V_r is the reference volume.

Table 7 EOS Linear Polynomial

Section	C0	C1	C2	C3	C4	C5	C6	E0	V0
Ambient	0	0	0	0	0.4	0.4	0	0	1
Compressed Low Pressure	0	0	0	0	0.4	0.4	0	90	1

Next, material states had to be defined for both the ambient and compressed low-pressure sections. Utilizing ideal gas laws, two MAT_009_Null cards were created for each section.

Table 8 MAT_009_Null Material Cards for ALE Elements

Section	RO	PC	MU	TERD	CEROD	YM	PR
Ambient	1.293e-6	0	0	0	0	0	0
Compressed Low Pressure	2.48e-4	0	0	0	0	0	0

With the initial gas conditions being properly defined, boundary conditions were applied. For this, a theoretical tube wall was needed to confine the gas within the tube. Elements on the outmost surface of the ALE sections were restricted from having gas flow normal to the element surface. Only flow parallel to the element surface of the tube was allowed. All other elements allowed flow in 3D space. A similar secondary boundary condition was given as the diaphragm. At the interface separating the low pressure and ambient sections of ALE defined gas, element surfaces were given a completely constrained condition with a death time. This allowed the pressures in the low pressure and ambient pressure to remain independent until the death time was met which simulates instant diaphragm burst. The importance of this was allowing a theoretical piston to compress the driven gas causing a higher internal pressure and pressure wave motion like the assumed experimental conditions. The death time of the boundary condition was dictated by the time of contact it made with that of the compression wave formed by the piston motion.

The theoretical movable piston was added to control the wave reflections like that experienced in the plug experiments and was used to generate the necessary pressures inside the tube. The piston motion was the most influential condition when characterizing the pressure-time profile. To begin the model, the piston was accelerated forward 100mm and abruptly stopped to simulate contact with the experimentally implemented piston plugs. The acceleration was approximated by using adiabatic compression relations and simple equilibrium equations on each side of the piston face. The pressure imbalance was used to estimate the piston movement knowing the weight of the piston in the experiment. The propagating pressure wave in the ALE model was then tracked, and the "diaphragm" boundary condition previously mentioned was released and the compressed gas in the low-pressure chamber was then allowed to interact with the ambient air and impinge on the material modeled next to the ambient chunk of air. A ridged plate was placed in front of the nozzle exit simulating the pressure plate with the PCB sensor in the pressure characterization experiments. The ALE elements tracked the pressure and velocity of the gas throughout the tube, nozzle, and ambient air between the nozzle and material sample. Gas expelling out of the blast tube nozzle was able to flow in free space. To record the pressure time history, a tracer was implemented on the center most element. The results show excellent agreement to the average pressure curve obtained at 23mm away (Figure 63).

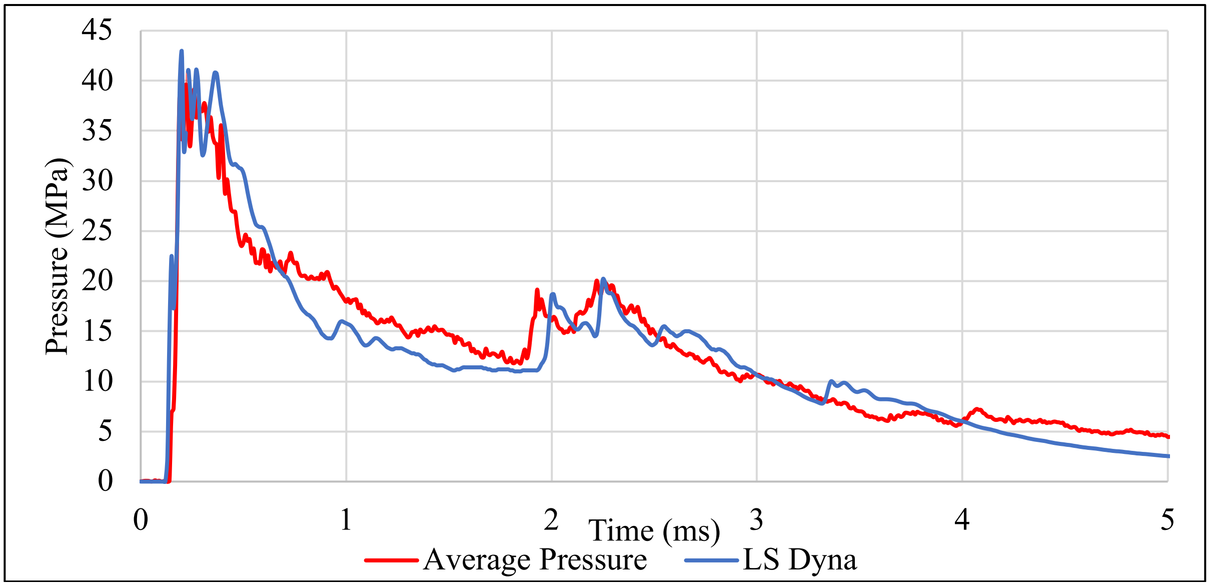

Figure 63 Averaged Pressure Data Vs. LS Dyna ALE Simulation

5.1.2 Pressure Distribution

To further validate the pressure characterization of the shock tube, the pressure distribution needed to be defined for the LS Dyna model. The ambient section between the blast nozzle and ridged plate allowed for the gas to flow in free space.

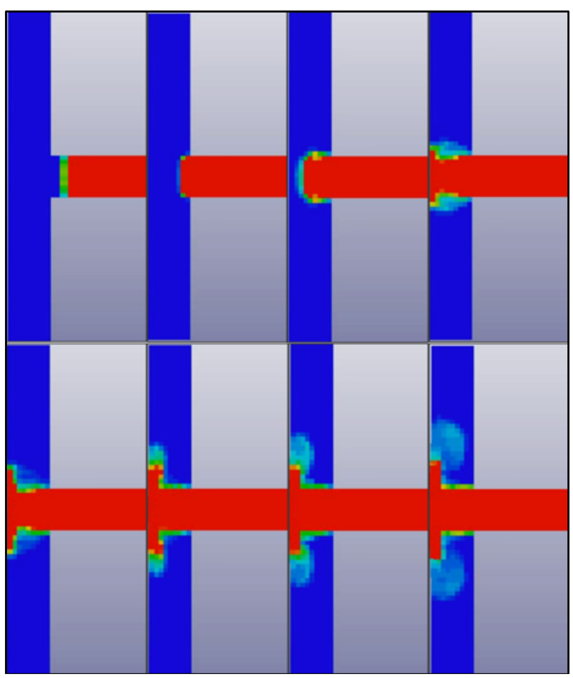

Figure 64 Progression of Gas Expansion Outside of Blast Nozzle Impinging on Ridged Plate

The modeled ridged plate was checked to see the pressure distribution and compared to the distribution previously obtained by the pressure sensitive films. The films depicted a collective 118.4mm diameter area of loading from 3.1MPa to the maximum pressure. However, it should be noted that this range does not happen simultaneously meaning, only the localized peak pressure is recorded, and not the pressure-time history. The pressurized air was assumed to have a spherical like loading distribution with the peak pressure in the very center of the blast nozzle with rapid pressure decay radiating out toward the edges of the films. This localized area of high pressure can be seen in the medium film ranging from 10 to 49MPa. This pressure loading was distributed over approximately 66.1mm diameter area which is validated with the model. Furthermore, the edge of the pressure loadings can be validated with the low-pressure film that was placed directly below the medium film. From the film, pressure ranges from 3.1-10+MPa was experienced over a diameter of 118.4mm. Figure 65 depicts the spliced low and medium films on a continuous pressure contour compared to that of LS Dyna.

With good agreeance on the peak pressures experienced on the films and in the model as well as reasonable assumptions and approximations made about the time of peak pressures, the LS Dyna ALE model can confidently model the pressures experienced by the ridged plate in the pressure characterization tests.

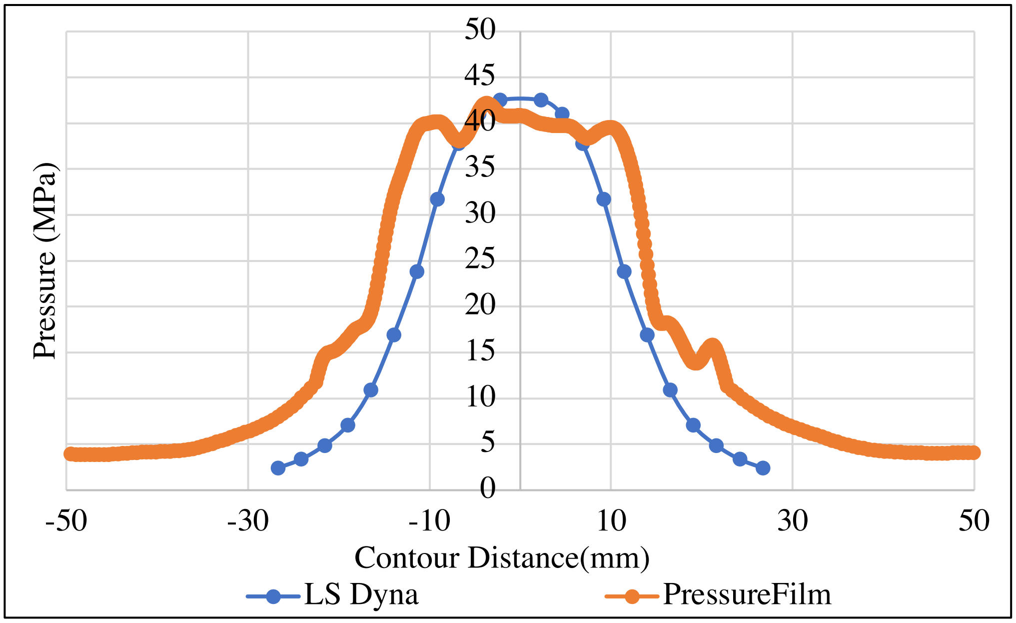

Figure 65 Pressure Distribution Over Plate with Films and LS Dyna

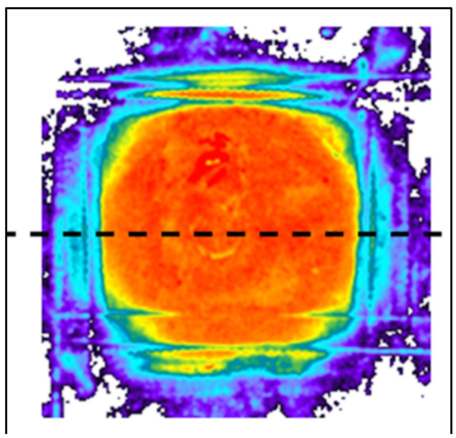

Figure 66 Cross section of Pressure Film used in LS Dyna Comparison

5.2 Aluminum Model

After the pressure loading was accurately modeled on the ridged plate (Figure 63), the monolithic and composite hybrid panels were then implemented in the model as in the shock tube experiments. First, monolithic aluminum plates were modeled and compared to the experimentally tested plates. The monolithic plate of aluminum was modeled first to obtain validation for the shock tube loading, and to instill confidence for implementation in the hybrid material model. By knowing the aluminum and the shock tube conditions were well defined, the composite material card would be able to be properly calibrated. The Johnson-Cook model is well understood, and material parameters are readily available in literature.

To tie material loading into the previously developed ALE shock tube model, the ridged plate in the original model used to mimic the calibration experiments was modified into the 3.175mm monolithic plates. The monolithic plates were modeled with ELFORM=2 standard integrated solid elements.

5.2.1 MAT_098 Simplified_Johnson_Cook

To capture strain rate effects for the aluminum components of the composite and monolithic plate of aluminum, a MAT_098 Simplified_Johnson_Cook material card was used. Johnson-Cook captures accurate strain hardening effects of most metals and is able to take quasistatic mechanical testing data and develop a strain rate sensitive model.

MAT_098 utilizes a simplified version of the Johnson-cook equation where thermal effects and damage are ignored. It should be noted that damage in LS Dyna is classified as material rupture which was not observed in these experiments. The simplification allows for a much faster computational time.

$$\sigma = [A + B(\varepsilon^{pl})^n]\left[1 + Cln\left(\frac{\varepsilon^{pl}}{\varepsilon}\right)\right][1 - \theta^m]$$

The original Johnson-Cook equation can be broken into respective parts. The first set of brackets relates stress as a function of strain where, *A* is the yield stress at the testing rate and speed, *B* is the strain hardening modulus, *n* is the strain hardening coefficient and ε^{pl}equivalent plastic strain. The second set of brackets is the strain rate term at the strain at which is being tested. The parameter, *C* defines the strain rate constant and $ln\left(\frac{\varepsilon^{pl}}{\varepsilon}\right)$ dimensionless plastic strain rate. The third set of brackets is the temperature term where, θ is the homologous temperature

$(T-T_{room})/(T_{melt}-T_{room})$, and M related to the thermal softening. Since all tests were done at room temperature, $(T=T_{room})$ the Johnson Cook formula reduces its form to

$$\sigma = [A + B(\varepsilon^{pl})^n]\left[1 + Cln\left(\frac{\varepsilon^{pl}}{\varepsilon}\right)\right].$$

The input parameters for MAT_098 utilized in both the monolithic plate and composite hybrid panel model can be found in Table 9.

Table 9 Johnson Cook Parameters for 7075-T6 Obtained at 0.001s^{-1} [62]

Parameter	A (MPa)	B (MPa)	n	C
Value	548	678	0.71	0.024

5.3 Hybrid Panel Model

Modeling the entire panel required multiple material cards and interface characterizations. The same Johnson-Cook material card was implemented in the hybrid panels for the aluminum face sheet. The entire hybrid panel was modeled with solid elements and each composite ply was individually modeled to capture the delamination with tie break constraints. The interfaces of both the composite and aluminum with the methacrylate adhesive were also modeled by tie break constraints. By incorporating these interfacial properties, delamination can be modeled throughout the entire panel.

5.3.1 Adhesive Modeling

The adhesive was modeled with MAT_001_Elastic material card and ELFORM=2 standard integrated solid elements. Since the adhesive had high elongation suitable for the large in-plane deformations and the interfacial properties were characterized, failure within the adhesive was not of interest. The material properties of the cured methacrylate adhesive were obtained from the manufacturer.

Table 10 MAT_001_Elastic Material Card for Methacrylate Adhesive

RO	E	PR	DA	DB
0.001	1100	0.3	0	0

5.3.2 Interface Modeling – Delamination

The hybrid panels have 15 interfaces all capable of delamination dictating the performance of the model and therefore, must be captured. The interface of the adhesive to the panel constituents called for characterization for the material model inputs in LS Dyna. The interfaces of the aluminum to adhesive, composite to adhesive and the interlaminar composite to composite properties were modeled with parameters characterized via butt joint test and lap shear. Maximum normal stress and maximum shear stress properties were obtained for the tie break criterion given by:

$$\left(\frac{\sigma_n}{NFLS}\right)^2 + \left(\frac{\sigma_s}{SFLS}\right)^2 > 1$$

Where $\sigma_n$is the current normal stress, $\sigma_s$is the current shear stress, NFLS is the normal stress at failure and SFLS is the shear stress at failure.

5.3.3 Composite Modeling

LS-Dyna finite element package uses different composite material behavior theories to accurately predict a material system under a given loading. To accurately describe the modeled material behavior in LS-Dyna, the material system tested needs characterization of its material properties. Tensile, compressive, and shear characterization properties of the hybrid material systems constituents were tested via ASTM standard to generate a LS Dyna material card for finite element validation simulations.

The most common LS Dyna composite material card is MAT_054 Enhanced Composite Damage, a progressive ply failure model. This material card is an enhanced version of MAT_022 (Composite Damage) that is widely used in crash simulations. The material card includes the option to select a failure criterion of Chang-Chang [63] or Tsai-Wu [64] by setting the CRIT parameter to 54 or 55 respectively.

Chang-Chang (Table 11) is a 2-dimensional failure criterion that accounts for tensile and compressive stresses in both fiber and matrix. Tsai-Wu (Table 12) is another 2-dimensional failure criterion but failure occurs only with tensile stress., compressive stresses do not contribute to failure criterion. With the case in blast loading normal to a composite plate, a beam in bending experiences compressive stresses that cannot be ignored. For this reason, MAT_055 was omitted from the model selection process. In MAT_054 and MAT_055, ply failure occurs when met by the selected stress criterion. Ply deletion occurs with a strain criterion. This means there is an option to have residual stress even after ply failure introducing material ductility in the composite model. The simulated shock tube pressure loading was used to load the material sample in LS dyna to obtain the most accurate loading profile.

Table 11 Chang-Chang MAT_54 Failure Mode Formulations [65]

Failure Mechanism	Stress Criteria Formulation	State
Tensile Fiber ($\sigma_{aa}>0$)	$e^2{}_f = \left(\frac{\sigma_{aa}}{X_t}\right)^2 + \beta\left(\frac{\sigma_{ab}}{S_c}\right)^2 - 1$	$e^2{}_f \geq 0 \rightarrow failed$ $e^2{}_f < 0 \rightarrow elastic$
Compressive Fiber ($\sigma_{aa}<0$)	$e^2{}_c = \left(\frac{\sigma_{aa}}{X_c}\right)^2 - 1$	$e^2{}_c \geq 0 \rightarrow failed$ $e^2{}_c < 0 \rightarrow elastic$
Tensile Matrix ($\sigma_{bb}>0$)	$e^2{}_m = \left(\frac{\sigma_{bb}}{Y_t}\right)^2 + \beta\left(\frac{\sigma_{ab}}{S_c}\right)^2 - 1$	$e^2{}_m \geq 0 \rightarrow failed$ $e^2{}_m < 0 \rightarrow elastic$
Compressive Matrix ($\sigma_{bb}<0$)	$e^2{}_d = \left(\frac{\sigma_{aa}}{2S_c}\right)^2 + \left[\left(\frac{Y_c}{S2_c}\right)^2 - 1\right]\left(\frac{\sigma_{bb}}{Y_c}\right) + \left(\frac{\sigma_{ab}}{S_c}\right)^2 - 1$	$e^2{}_d \geq 0 \rightarrow failed$ $e^2{}_d < 0 \rightarrow elastic$

Table 12 Tsai-Wu MAT_54 Failure Mode Formulations [65]

Table 12 (Cont'd)

Failure Mechanism	Stress Criteria Formulation	State
Tensile Fiber (σ_{aa}>0)	$e^2{}_f = \left(\frac{\sigma_{aa}}{X_t}\right)^2 + \beta\left(\frac{\sigma_{ab}}{S_c}\right)^2 - 1$	$e^2{}_f \geq 0 \rightarrow failed$ $e^2{}_f < 0 \rightarrow elastic$
Compressive Fiber (σ_{aa}<0)	$e^2{}_c = \left(\frac{\sigma_{aa}}{X_c}\right)^2 - 1$	$e^2{}_c \geq 0 \rightarrow failed$ $e^2{}_c < 0 \rightarrow elastic$
Tensile Matrix (σ_{bb}>0)	$e^2{}_m = \left(\frac{\sigma_{bb}{}^2}{Y_tY_c}\right) + \left(\frac{\sigma_{ab}}{S_c}\right)^2 + \frac{(Y_c - Y_t)\sigma_{bb}}{Y_tY_c} - 1$	$e^2{}_m \geq 0 \rightarrow failed$ $e^2{}_m < 0 \rightarrow elastic$
Compressive Matrix (σ_{bb}<0)	$e^2{}_d = \left(\frac{\sigma_{bb}{}^2}{Y_tY_c}\right) + \left(\frac{\sigma_{ab}}{S_c}\right)^2 + \frac{(Y_c - Y_t)\sigma_{bb}}{Y_tY_c} - 1$	$e^2{}_d \geq 0 \rightarrow failed$ $e^2{}_d < 0 \rightarrow elastic$

Mat_058 is a continuum damage model governed by Matzenmiller-Lubliner Taylor theory [66]. Similar erosion criteria as MAT_054 are included in the model.

When comparing MAT_054 and MAT_58, it is seen that both cards require similar inputs and the same material characterization data. MAT_058 describes a composite with a nonlinear elastic behavior, however. The result being, MAT_058 tends to behave a bit more plastic without a definite failure point.

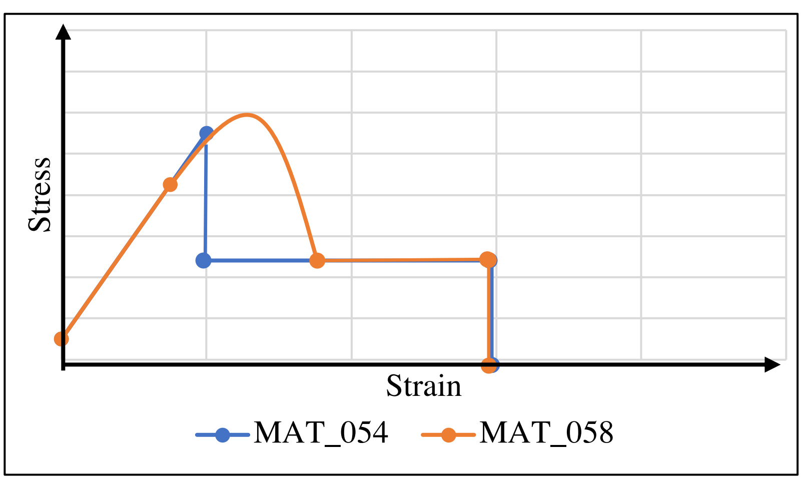

Figure 67 MAT_054 Vs. MAT_058 Stress-Strain Curves

Work by Jackson et. al compared simulated deformations of helicopter components using both MAT_054 and MAT_058 [67]. Under the study, it was found that MAT_054 performed more brittle when compared to MAT_058. However, at the time of the work done by Jackson, MAT_054 did not include the plastic parameters that it does at the time of this research, and the assumption of unrealistic deformation behaviors cannot be made. From their experimentally tested aerospace components, 45° fabric was used for construction. The 45° composite compressive behavior might have exhibited nonlinear elastic behavior which would describe the better deformation agreeance. Nonetheless, their research highlights a key observation in which both material models stating that LS Dyna cannot predict composite failure using either material card, only be calibrated to illustrate the failure. Many of the damage parameters used to characterize failure and plasticity cannot be obtained experimentally and must be approached by trial and error. This is an important observation as multiple iterative processes must be done to achieve a representative simulation.

MAT_158 follows the same continuum damage model as MAT_058 includes viscoelastic strain hardening effects admirable to high strain rate loading cases. However, the material model is only accurate to 115% of the quasi-static strength. From literature, both thermoset and thermoplastic composites have experienced strain rate effects well above 115% [68]–[70]. For that reason, it was assumed that the PET/GF composite or the epoxy/GF composite would reach a higher level of strain rate effect to be able to accurately be captured in MAT_158 thus, omitting MAT_158 from selection.

Taking the material behavior and loading application into consideration, MAT_054 was decided to be the best suited composite material card for this blast loading application. The MAT_054 card has been utilized successfully for modeling the damage behavior of thermoplastic composites in high loading rate automotive crash simulations [71], [72] and has also shown to successfully describe modes of failure in flexural bending loads [72],[73].

5.3.2 MAT_054 Modeling

To characterize the material for MAT_054, tensile, compression and shear properties were needed. To obtain the most accurate model, it is important to experimentally determine these mechanical parameters. When dealing with thermoplastics, a wide range of manufacturing factors can influence composite performance. Heating and cooling rates, degrees of consolidation, mold temperature, the overall fabrication process can lead to large amounts of variability. Utilizing the same manufacturing process and parameters as the blast tested specimens.

Chapter 6 Material Characterization

6.1 Lab Specimen Manufacturing

The TC940 PET/GF panels were manufactured in the same manner as the experimentally tested blast panels. The bulk panels were cut into their designated ASTM standard coupon form via waterjet (Figure 68). Specimens were analyzed for edge finish, fiber alignment and any other manufacturing defect such as air voids or cracks using a Nikon SMZ25 Microscope. The images show good fiber matrix wetting and adhesion (Figure 69 and Figure 70).

Figure 68 Water Jet Cut Samples of TC940 Thermoplastic Composite

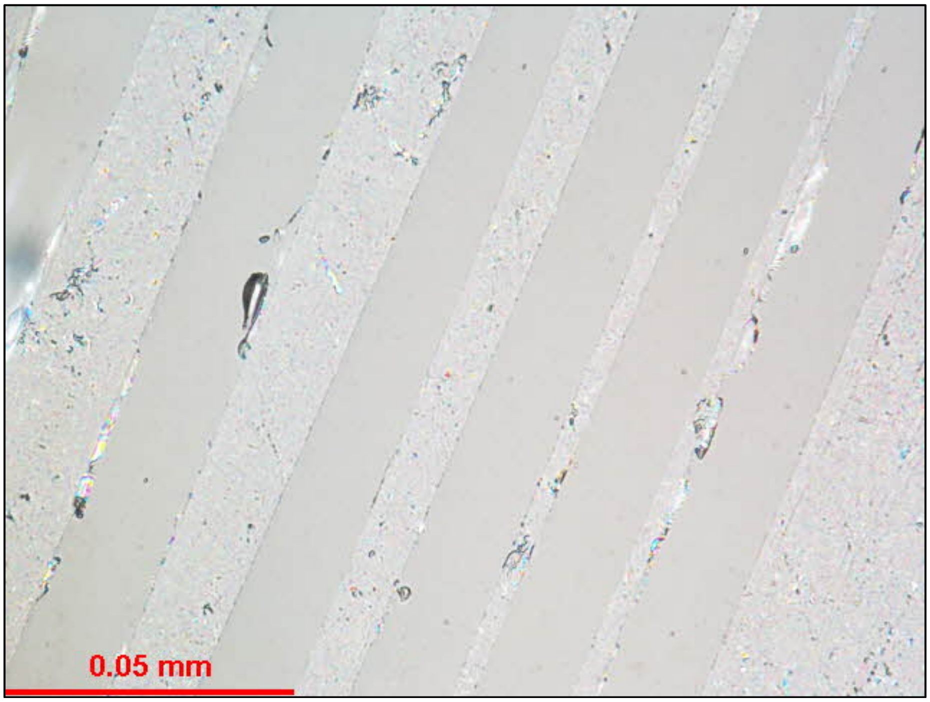

Figure 69 Fiber Matrix Interface (Longitudinal to fiber)

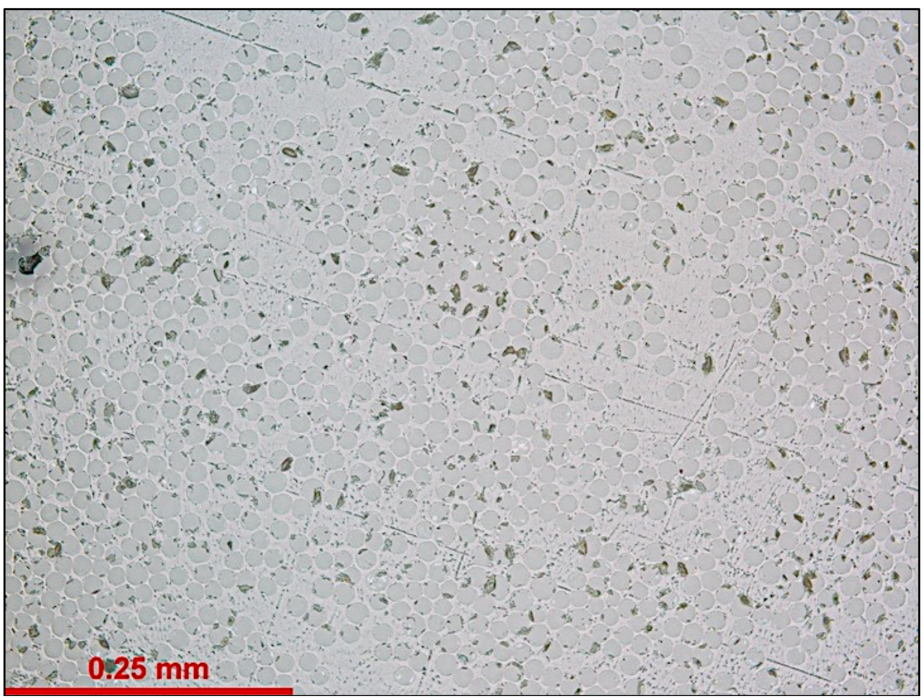

Figure 70 Fiber Matrix Wetting

Figure 71 illustrates a single ply fiber bundle embedded in the laminate stack up. Figure 72 depicts consolidation between multiple plies. As seen in the image, fiber banding of widths

0.25mm is observed. This is expected as the ply thickness of the TC940 is 0.26mm. The plies are separated by an intermediate resin rich area of PET.

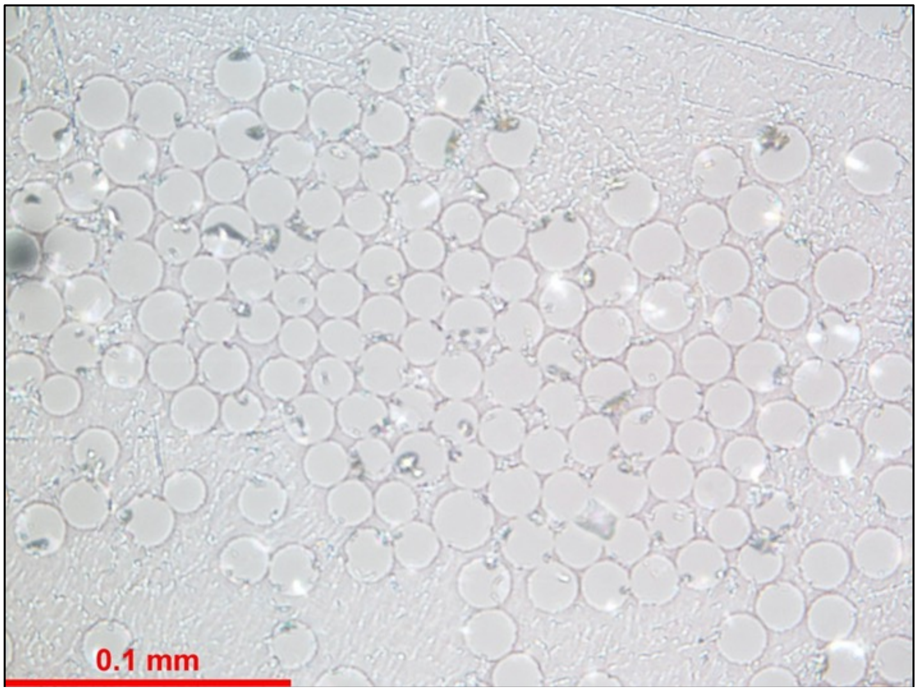

Figure 71 Individual Ply Bundle

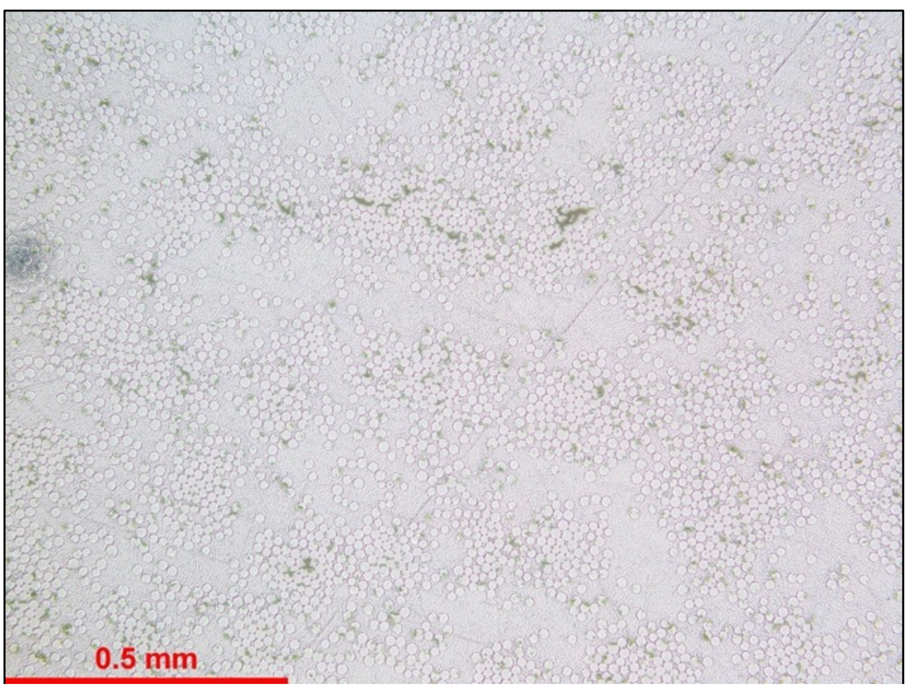

Figure 72 Ply Consolidation

Figure 73 is a higher magnification of the fiber diameter of the glass fiber for this particular composite. The TC940 had a fiber diameter of $19\mu m$ which is consistent with the sizing in industry [74].

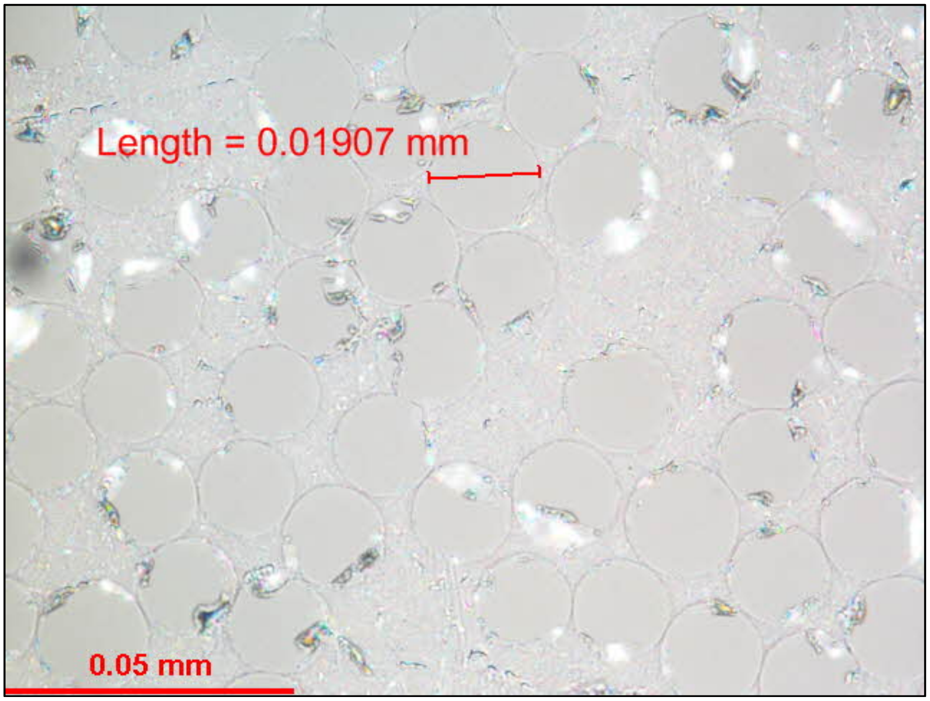

Figure 73 Fiber Dimension

6.2 Tensile Testing of Composite

Tensile testing for both the 0° and 90° TC940 composite laminates was conducted on an Instron 5984 universal testing system with a 150kN capacity load cell (0.5% tolerance) and a 150kN rated wedge action grips. An Instron 2663-901 video extensometer was used to track longitudinal strains in accordance with ASTM 3039 Standard Test Method for Tensile Properties of Polymer Matrix Composite Materials**.**

6.2.1 Tensile Specimen Manufacturing

Specimen dimensions for the 90° samples were 25.4mm wide by 2mm thick by 254mm long. Specimen dimensions for the 0° samples were 12.7mm wide by 1mm thick by 254mm long. Tabs were added to the ends of the specimens due to weak compressive strength. Previous work done by the author found that compressive failure in the grips was common leading to crushing and eventual shearing of the material.

With high tensile strength unidirectional composites, high compressive loads in the grip area are needed to anchor the specimen down under high tensile loadings. To avoid the composite material crushing under the grip compression, tabbing material is required to act as a stress transfer medium. To transfer the tensile stress to the tabs, high amounts of shear stress is generated at the composite-tab interface. A high shear strength adhesive is needed to act as a stress transfer medium here. However, adding a thick adhesive bond line and abrupt composite tabbing material, a stress concentration manifests at the front of the tab closest to the gauge length causing premature failure. Beveling of the composite tab aids in transferring the tensile load to the tabs for a proper tensile strength measurement. Finite element analysis was done in Abaqus CAE to estimate the shear strength needed at the tab-composite specimen interface and to analyze the effectiveness of a beveled tab. Micromechanics and existing manufacturing data [75] was used to approximate the strengths and stiffnesses of the TC940. The G-10 tabbing material properties used the findings from Ravi-Chandar et. al. [76]. A generic methacrylate adhesive property was used as a preliminary material for the tabbing adhesive. Figure 74 illustrates the planes of symmetry through the tensile coupon model for finite element evaluation.

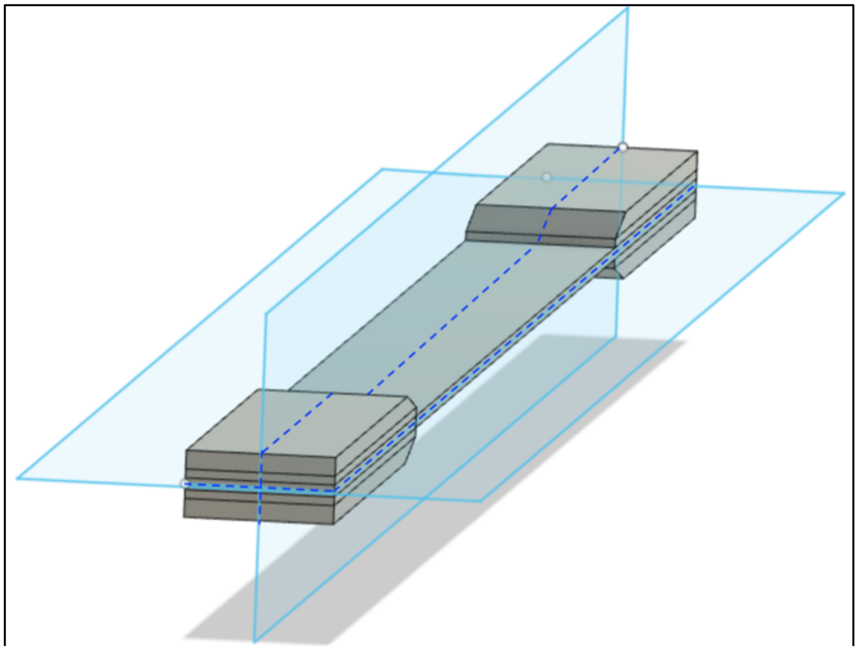

Figure 74 Finite Element Planes of Symmetry

A sacrificial 1.5mm thick and 57.15mm long G-10 fiberglass composite was used as the tabbing material. The 0/90 layup of the G-10 and relatively softer hardness provides a good load bearing material to cushion the compressive loads from the tensile grips. Figure 75 and Figure 76 are formulations demonstrating the need for beveled tabs. Figure 75 shows the through thickness composite and G-10 tabbing material stresses under peak tensile loading of the TC940 for the 12.5º beveled tabs. Figure 76 depicts the same experimental set up, aside from having no bevel on the grip tab. Clearly, a stress concentration develops at the adhesive bond area in the composite with the potential to prematurely rupture the specimen a lower tensile strength outside of the gauge length of the specimen.

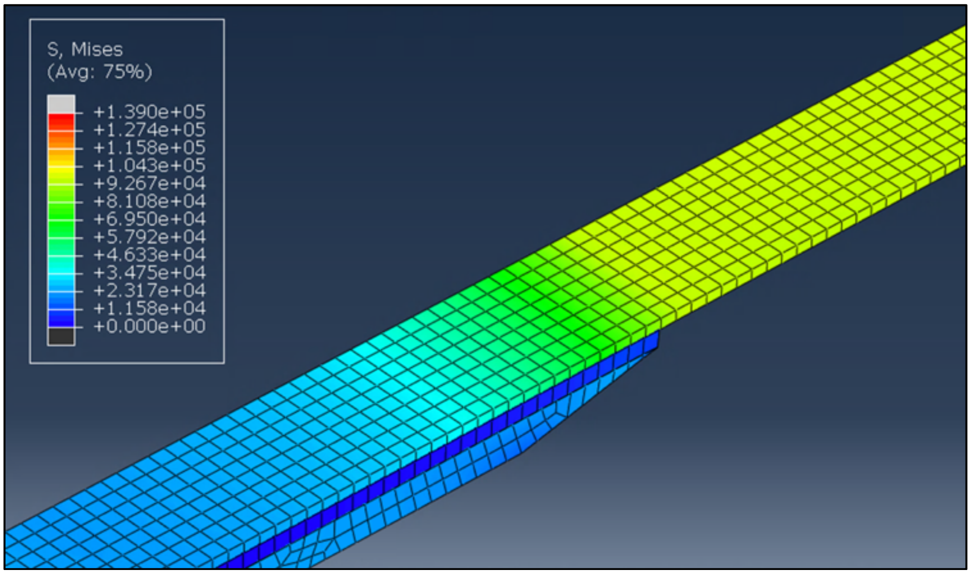

Figure 75 Stress Transition with 12.5º Bevel in Tabs

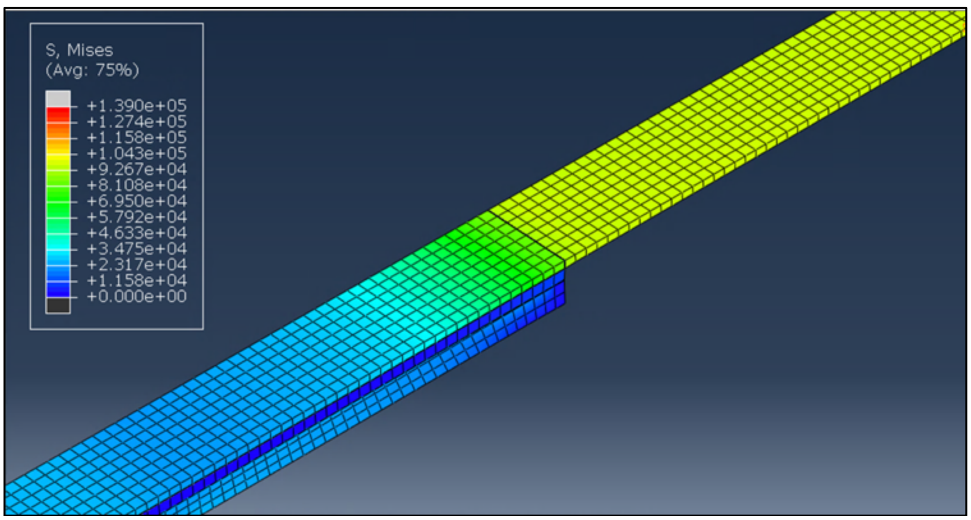

Figure 76 Stress Transition with 90º Bevel in Tabs

Two styles of grips were available for the tensile testing; a set of 150kN wedge action grips as well as 10kN rated screw driven grips. The wedge action grips have a 50.4mm grip depth compared to the 25.4mm grip depth of the screw driven grips. The wedge action grips have increasing compressive force with higher tensile loads. These grips self-tighten as the tensile load from the composite specimen pulls the wedge into the grip end (Figure 77). These grips have a deeper grip area allowing for a larger pressure distribution, but the compressive force acting on the composite was strictly dependent on how high the ultimate tensile load of the composite specimen is.

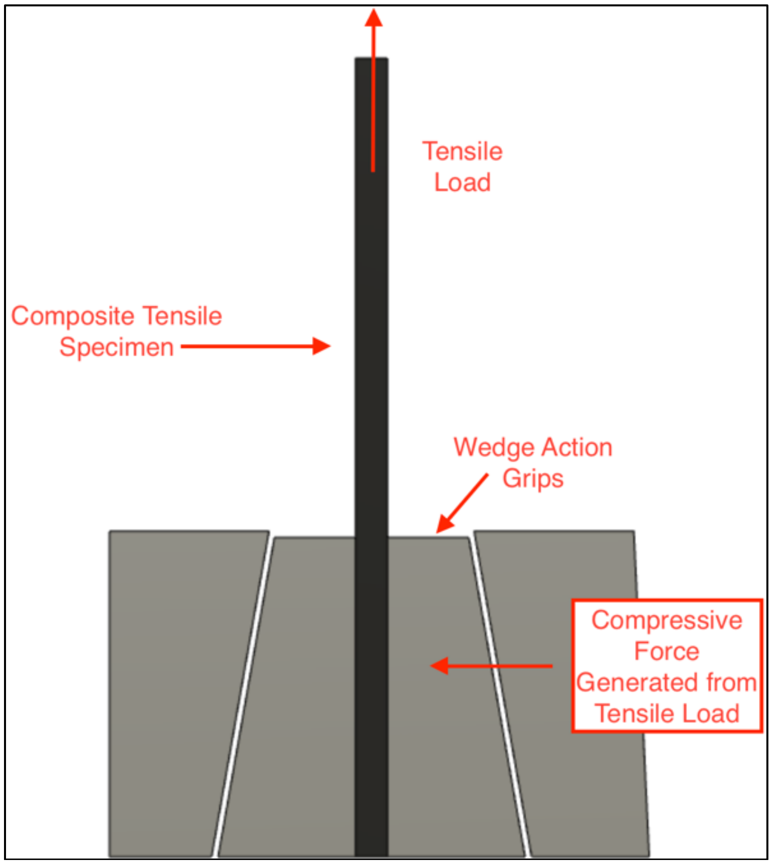

Figure 77 Wedge Action Grips

The screw driven grips have grip depth of 25.4mm. These grips allow for complete user control on the compressive force acting on the tensile specimen when a known torque is applied (Figure 78). This allows no additional compressive forces to build during a tensile test eliminating the risk of the sample crushing in the grips. However, since these grips have a smaller load bearing area than the wedge action grips, more force may need to be applied to prevent grip slippage under higher tensile loads.

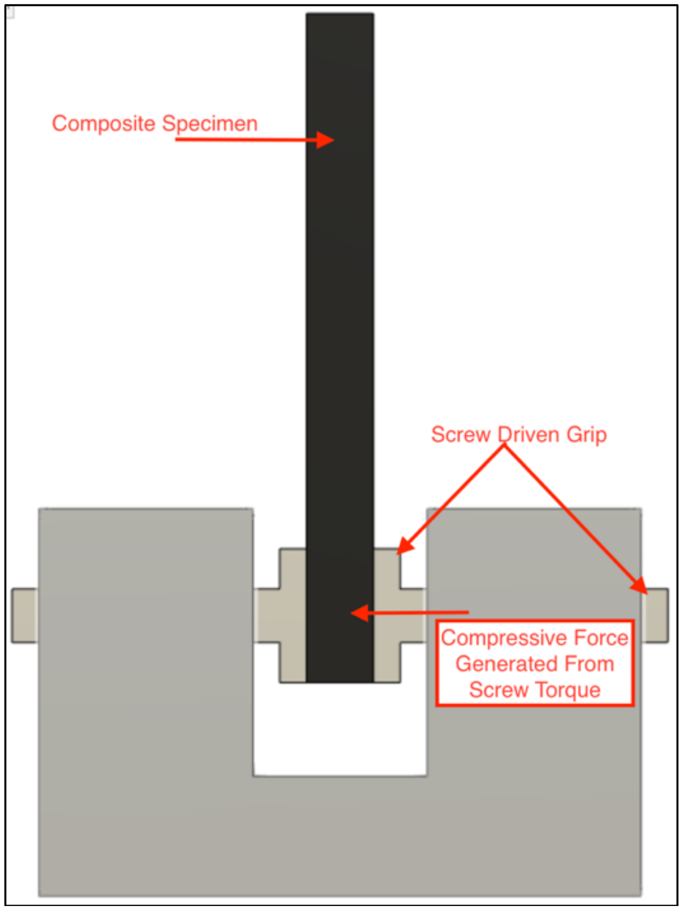

Figure 78 Screw Driven Grips

An approximation of the force used to tighten the screw driven grips was made by converting a tightening torque to an axial load on the 25.4mm square grip. It was estimated that around 19MPa (2750PSI) would be applied over the 12.7mm by 25.4mm grip area. The wedge action grips clamping force was estimated by following an industry white-paper by R-tech materials [77]. Using the projected tensile strength of the material, and assuming a 10º wedge angle, it was estimated that around 21MPa (3000PSI) was applied over the 12.7mm by 25.4mm grip area at peak load. Figure 79 and Figure 80 demonstrate the Tresca shear stresses in the tabbing adhesive with the two Instron grip in question for clamping the material. In the figures, the composite and the tabbing material are hidden from view to depict the stresses more clearly in the adhesive. The screw driven grips were found to reduce the Tresca shear stress in the adhesive when compared to the wedge action grips. The crushing force on the composite at peak loads for both the wedge action and screw driven grips was found to be satisfactory as both the adhesive and the G-10 composite was able to carry and distribute the loading onto the composite successfully. Compressive loads for each grip were below the 90º compressive strength found in compression testing.

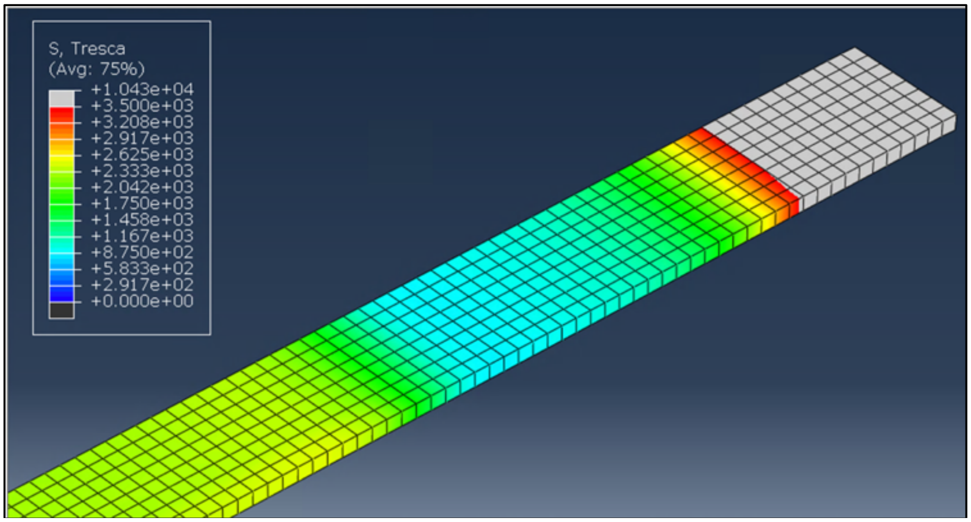

Figure 79 Tresca Maximum Shear Stress in Adhesive; Screw Driven Grips

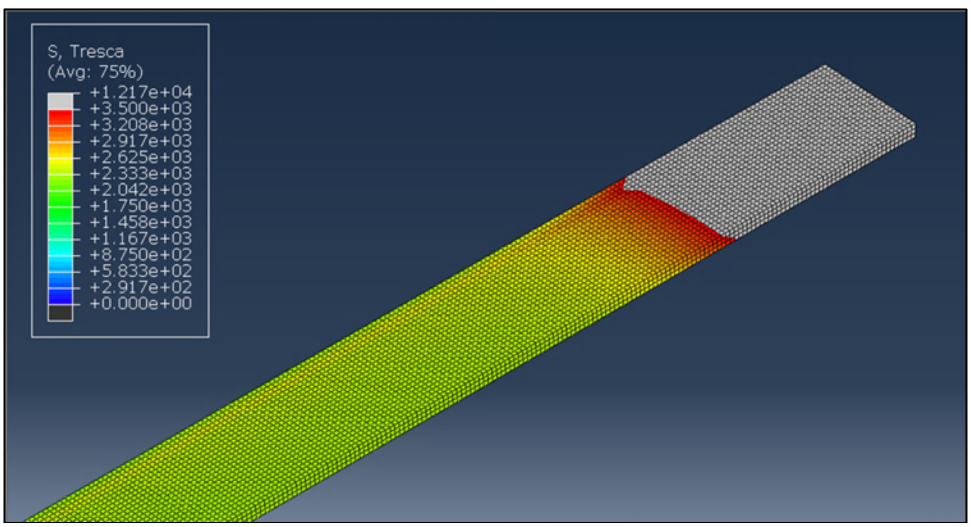

Figure 80 Tresca Maximum Shear Stress in Adhesive; Wedge Action Grips

Knowing the shear strength needed at the interface, Plexus MA310 methacrylate adhesive was used to bond the tabs to the TC940. Methacrylate adhesives give desirable elongations and better adhesion to thermoplastic type resin systems. A bevel angle of 12.5º was cut into the tabs to alleviate any stress concentrations at the grips. To bevel the angle into the composite tabs, a section of angle iron was cut so the back face of the angle iron made a 12.5º angle from horizontal. The fixture was then placed onto a magnetized surface grinder set up and the G-10 was fixed to the back of the fixture as seen in Figure 81. The bevel was then ground down into a proper finish with the final 12.5º angle. Finite element analysis was conducted to validate that the adhesive would not fail in shear as the composite specimen was pulled.

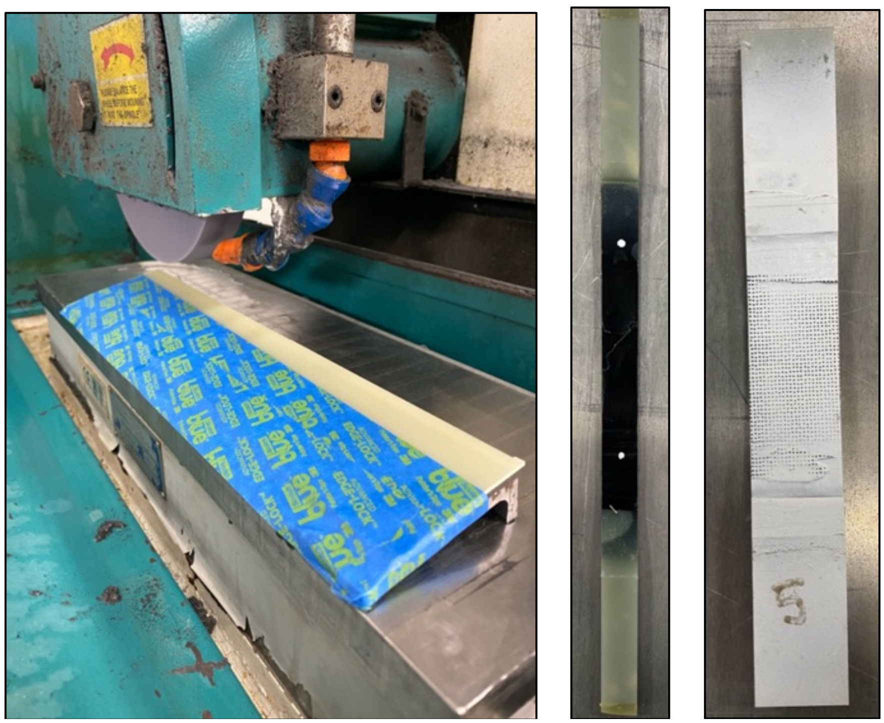

Figure 81 Left to right: Surface Grinding Beveled Tabs, 0º Tensile Bar, 90º Tensile Bar

6.2.2 Tensile Testing Results

Tensile testing for both the 0º and 90º unidirectional samples proved to be difficult due to the extraordinarily strong tensile strength and relatively weak compressive strength in the 90º orientation. Grip crushing, tab failure, and longitudinal splitting were all observed failures indicative of faulty tests at stress failure levels below a representative value for the tensile tests. The longitudinal splitting is suspected from eccentricities in the fiber straightness in the composite panel. As the thermoplastic matrix transitions into a molten state, fiber drift occurs with the now liquid resin flowing into void areas in the mold. Cutting the unprocessed plies to the exact width and length of the mold is crucial in obtaining straight unidirectional composites. Grip crushing and premature failure were all observed when testing the 90º test specimens. It is suspected there is microcracks within the composite causing premature failure in the matrix loading direction. Though premature failure occurred in both orientations of tensile testing, the linear elastic behavior of the composite was captured. Elastic moduli of the 0º and 90º were 35.3GPa and 6.5GPa respectively. The 90º laminate experienced low strength for the expected tensile strength with a failure stress of 15.4MPa and a failure strain of 0.235%. However, consistent failure limits were observed in different representative panels. It was thought that if a crack propagated throughout the length of the bulk material panel, one panel should not be a representative sample space for the test specimens. Therefore, the 90º tensile specimens were tested from different material panels and experienced failures all within the gauge length at similar failure limits. For that reason, it was assumed these properties were true to the composite and manufacturing set up.

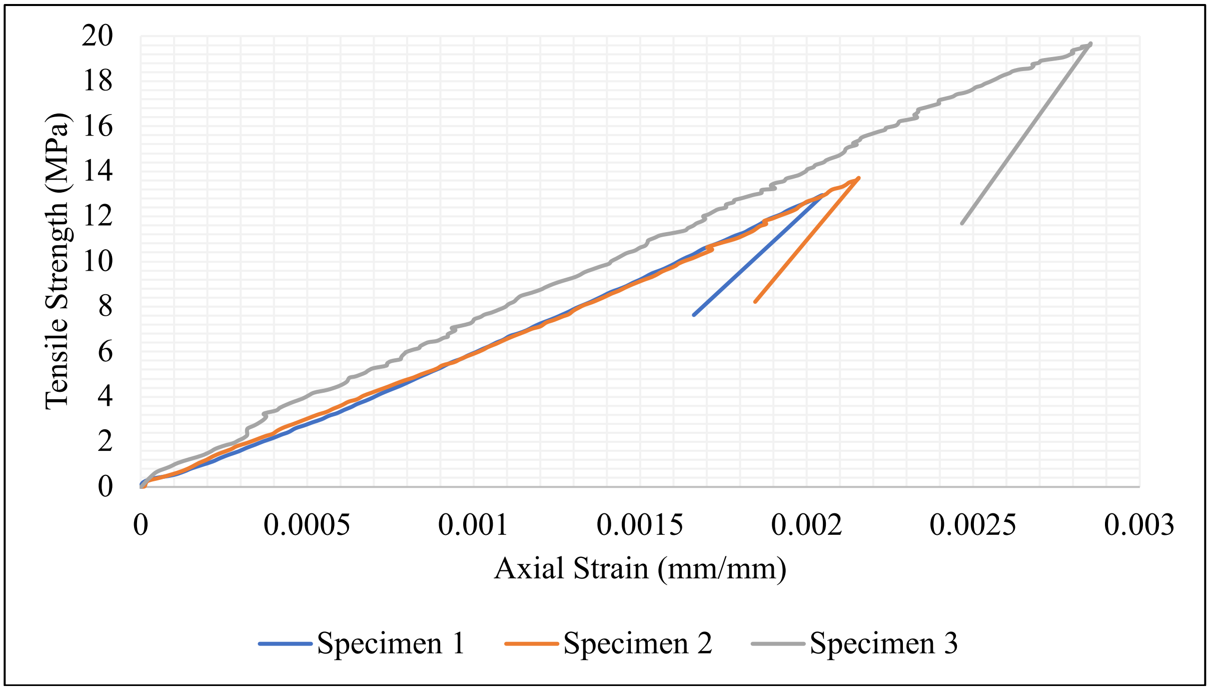

Figure 82 Stress-Strain 90º Laminate

Table 13 90º Unidirectional Tensile Data

Test Item ID #	**Thickness (mm)**	**Width (mm)**	**Tensile Stress (MPa)**	**Tensile Modulus (GPa)**	**Strain (%)**
T90-Sample 1	2.00	25.96	12.9121	6.871	0.205
T90-Sample 2	2.00	25.94	13.7106	6.298	0.216
T90-Sample 3	2.00	25.96	19.6742	6.393	0.285
Average	2.00	25.95	15.432	6.521	0.235
Std. Dev.	0.00	0.01	3.695	0.307	0.043

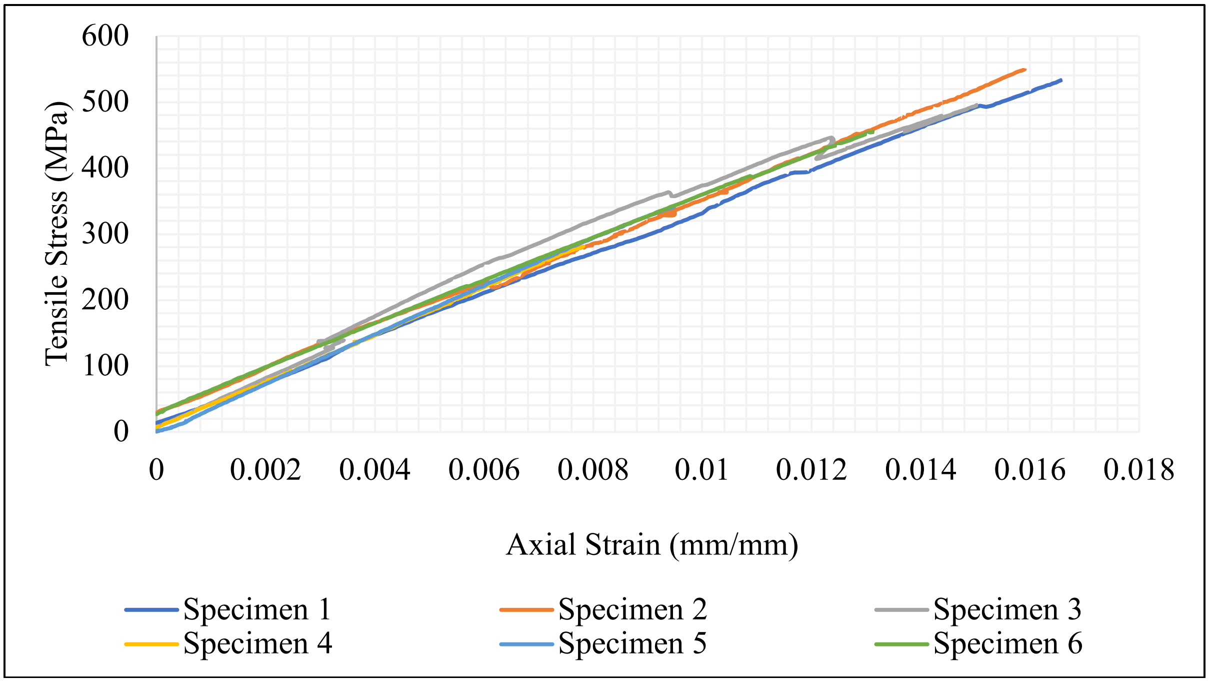

Figure 83 Tensile Testing 0º Direction Elastic Data Only

Table 14 0º Unidirectional Tensile data

Test Item ID #	Thickness (mm)	Width (mm)	Tensile Stress (MPa)	Tensile Modulus (GPa)
T0-Sample 1	1.24	11.03	535.468	33.728
T0-Sample 2	1.24	9.00	552.411	31.234
T0-Sample 3	1.24	13.80	517.507	39.697
T0-Sample 4	2.00	12.43	346.037	36.653
T0-Sample 5	1.22	13.61	346.000	37.731
T0-Sample 6	0.26	12.67	469.062	32.861
Average	1.20	12.09	N/A	35.317
Std. Dev.	0.55	1.81	N/A	3.226

To characterize the tensile strength at failure for the 0º laminate without longitudinal splitting, DIC software was utilized on a single ply laminate to obtain a localized strain at failure. A Instron 2663-901 video extensometer with Bluehill DIC Replay software was used to track longitudinal and transverse strains single ply composite samples. The DIC software was then used to map stress and strain contours throughout the entire gage length of the tensile sample. A 16mm lens with a 309.88mm field of view was used to obtain 2048x2048 pixel, 4 MP sequential images. The DIC speckle pattern was applied via roller and a used 0.33mm dot size for the resolution and field of view set up.

Knowing the crosshead displacement and assuming a failure strain of 0.02mm/mm, an estimated time to failure was around 3 minutes. Using a 4MP camera, it was estimated that a good image capture rate for DIC that lead to a manageable file size with good resolution would be about 2 images per second or a sampling rate of 0.5 seconds per image. The localized strain was then used to theoretically calculate a stress at break knowing the initial elastic properties of that exact tensile bar. Figure 84 depicts the location of a virtual extensometer just before longitudinal splitting was observed over the local area. The graph depicted gives the strain of the localized area of composite over time. It can be observed that around 2.9% strain, failure occurred within that area of composite. From here, utilizing the elastic modulus of the same tensile bar (32.86mpa) lead to a theoretical stress of 952 MPa at localized failure. This value was deemed credible as the manufacture properties listed a tensile strength of 960 MPa at failure. The procedure was repeated with consistent results and therefore, the listed manufacturing specification was utilized for the maximum tensile strength at failure for the 0^{o} laminate.

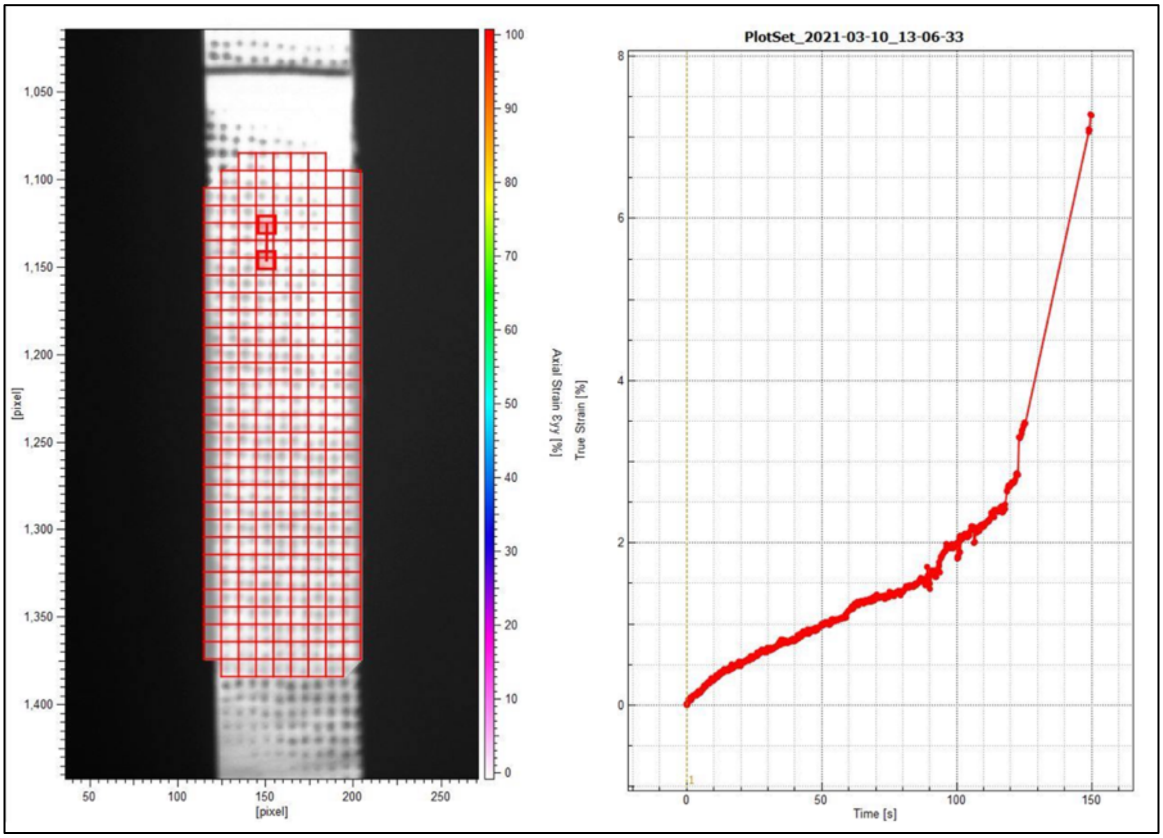

Figure 84 DIC localized strain at failure

6.3 Compression Testing of Composite

Compressive testing was performed on an Instron 5984 universal testing system with 150kN load cell (0.5% tolerance) and two spring assisted platens. Cylindrical samples of 12.7mm diameter and 25.4mm length were loaded in the center of the platen and preloaded so the specimen would not shift upon initial contact loading. A constant crosshead displacement of 1.3mm/min was implemented, and the samples were tested. Compression testing was conducted in accordance with ASTM D695 Standard Test Method for Compressive Properties of Rigid Plastics [78]. Composite moduli were found to be below the 41,370 MPa threshold, and therefore this testing procedure was deemed credible. Previous research done by the author found that using a modified Boeing fixture with a dog bone shaped specimen led to difficulties testing.

6.3.1 Compression Specimen Manufacturing

Proper edge quality was critical in obtaining representative data. It was found lab samples would have to be professionally finished without purchasing a sample preparation machine. For this reason, ASTM D695 was chosen as prismatic lab specimens were easily machinable. Rectangular specimens were avoided as highly precise cuts would be needed to ensure the lab specimen was completely parallel on each face. To avoid introducing any eccentricity in sample manufacturing, it was determined lathing a rectangular bar of the composite into a cylindrical lab specimen was best. The result was a consistent diameter rod that was faced to provide a flat, uniform compressive specimen. Cylindrical lab specimens were lathed to half inch diameter size and the surface finish quality was analyzed (Figure 85).

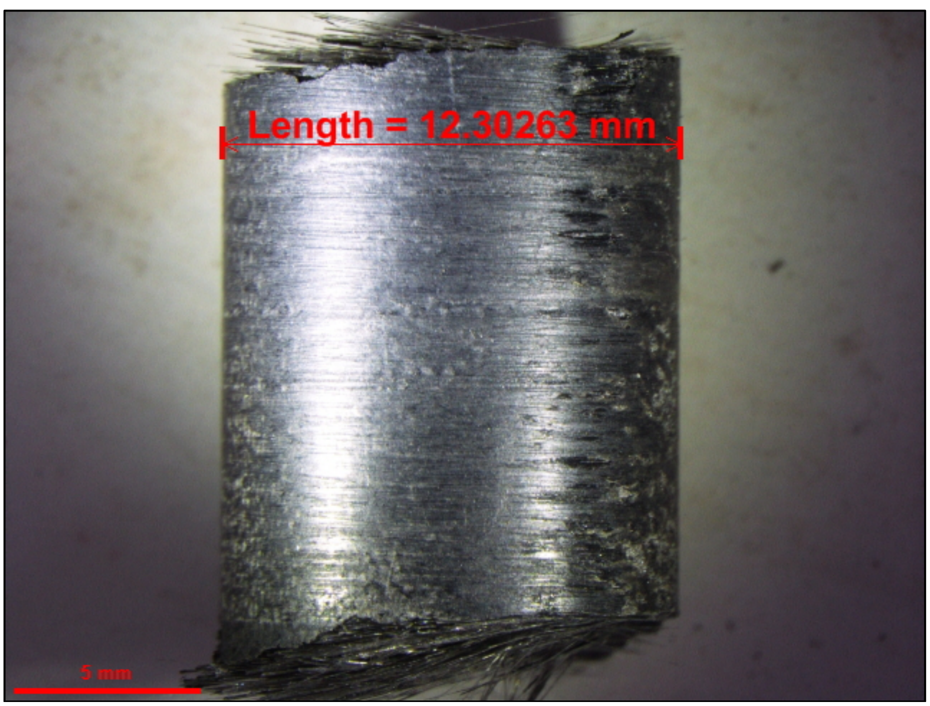

Figure 85 Lathed Section of Cylindrical Compression Specimen

6.3.2 Compression Testing Results

Compression testing in the 0º led to failure at consistent strain and stress. Under compression load, the composite behaved linear elastic until a somewhat brittle failure. The slight ductility experienced after failure can be attributed to the slight load bearing ability from a columnar failure mode (Figure 88). Under peak compressive load, the composite specimens experienced a somewhat explosive failure as splinters of composite fractured through the sample in fiber direction throughout the entire length. Since the fiber bundles has somewhat rigidity, they could bear weight until the sample began to mushroom and collapse. The compressive strength was nominally found to be 376MPa with an average failure strain of 0.021mm/mm and compressive modulus of 18.2GPa.

Table 15 0º Compression Data

Test Item ID #	Diameter (mm)	Height (mm)	Peak Load (kN)	Strain at Break (mm/mm)	Compressive Modulus (GPa)	Max Compressive Strength (MPa)
C0 Specimen 1	10.89	25.65	38.996	0.025	18.300	418.668
C0 Specimen 2	10.89	23.15	41.275	0.024	20.600	443.137
C0 Specimen 3	10.89	24.20	35.679	0.021	18.200	383.061
C0 Specimen 4	10.89	24.69	29.879	0.018	18.800	320.789
C0 Specimen 5	10.89	24.54	34.107	0.017	22.000	366.184
C0 Specimen 6	10.89	25.08	30.407	0.019	19.300	326.453
Average	10.89	24.552	35.057	0.021	19.533	376.382
Std. Dev.	0	0.847	4.559	0.004	1.491	48.942

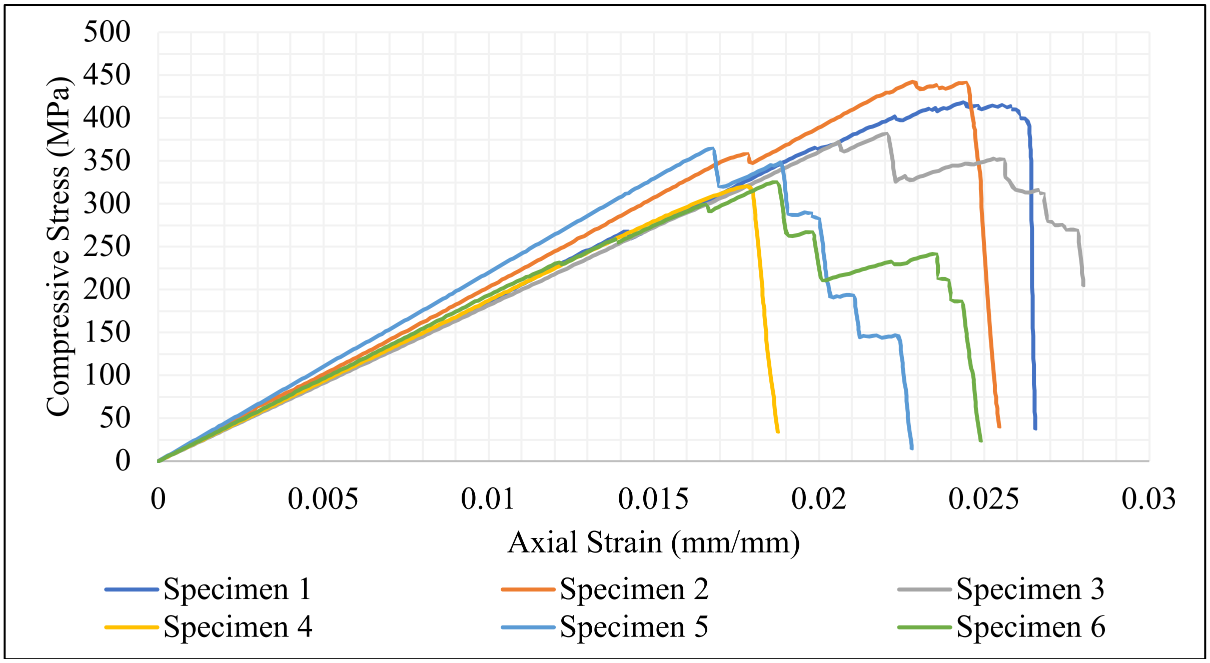

Figure 86 0º Compression Stress-Strain

Compression testing in the 90º led to failure at consistent strain and stress. Under compression load, the composite behaved linear elastic until a somewhat brittle failure. The slight ductility experienced after failure can be attributed to the slight load bearing ability from a cone/split failure mode (Figure 88). Here, the crack propagates axially from the center to the outermost sides and continues to crush until the crack reaches the side and collapses. The compressive strength was nominally found to be 68.6MPa with an average failure strain of 0-0.013mm/mm and compressive modulus of 5.7GPa.

Table 16 90º Compression Data

Test Item ID #	Diameter (mm)	Height (mm)	Peak Load (kN)	Strain at Break (mm/mm)	Compressive Modulus (GPa)	Max Compressive Strength (MPa)
C90 Specimen 1	13.420	24.080	8.150	0.011	5.182	57.621
C90 Specimen 2	13.420	22.490	10.616	0.014	5.637	75.053
C90 Specimen 3	12.500	30.710	7.503	0.014	5.687	61.143
C90 Specimen 4	12.500	30.970	9.891	0.013	6.485	80.598
Average	12.960	27.063	9.040	0.013	5.748	68.604
Std. Dev.	0.460	3.820	1.261	0.001	0.469	9.510

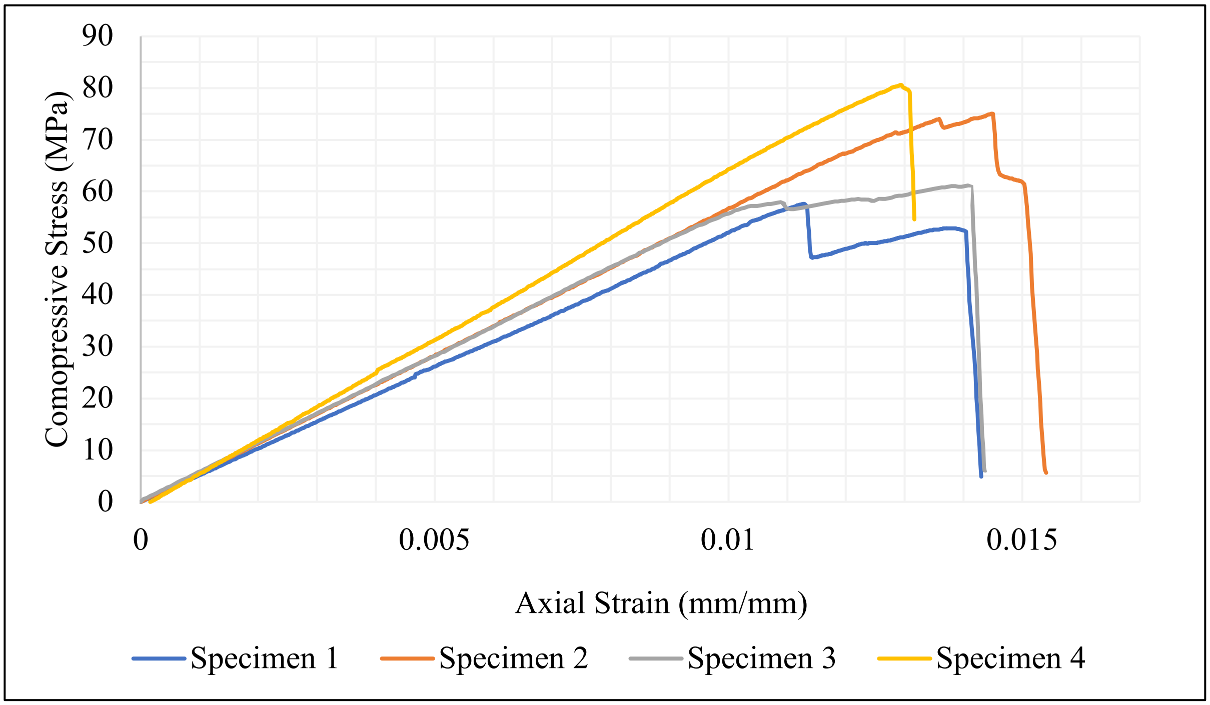

Figure 87 90º Compression Stress-Strain

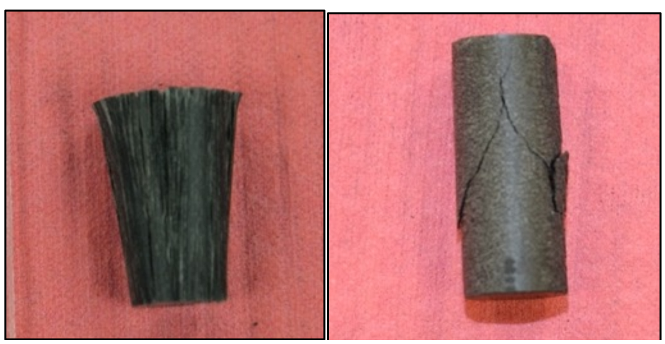

Figure 88 Typical Compression Failure Modes 0º (Left) and 90º (Right)

ASTM D695 does not define failure modes. However, it was observed that these compressive specimen failure modes were similar to that of concrete specimens under failure mode classification in ASTM C39-03 [79]. Seeing as concrete is a composite, parallel conclusions can be made when classifying failure modes. In Figure 88 two distinct failure modes can be observed. The left figure (0º fiber direction) depicts a columnar failure. The right figure (0º fiber direction) depicts cone and split failure modes. Both failure modes are recognized as complete failures with representative data for compression properties.

ASTM D695 defines a Hookean region where the initial start to the compression test begins with seating the platen on the specimen and crushes the eccentric faces. This is leads to a "toe" to the stress strain curve as seen in Figure 89. This behavior was observed and corrected per ASTM standard. The elastic region was extrapolated down to point B and the strains were adjusted so that point B was the start of the test and the point of zero strain. The result was a linear elastic response until ultimate failure.

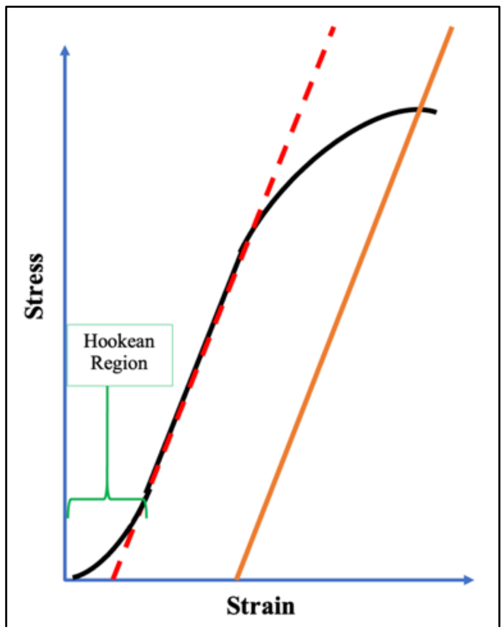

Figure 89 ASTM D659 Hookean Region

6.4 Shear Testing of Composite

Shear testing was conducted with a 45º tensile coupon per ASTM D3518 Standard Test Method for In-Plane Shear Response of Polymer Matrix Composite Materials by Tensile Test of a 45° Laminate[80] ASTM D3518 provides an easier alternative to shear testing when compared to an Iosipescu antiseptically loaded notched specimen test (ASTM D5379). An Iosipescu test requires specialty equipment to load the sample asymmetrically as well as demands near perfect specimen manufacturing.

6.4.1 Shear Specimen Manufacturing

Shear specimens were manufactured using a 0-90 laminate stack with a thickness of roughly 6mm. Specimens were cut from the bulk material panel at a 45-degree angle using an Axitom abrasive cutting saw into their desired ASTM specifications.

6.4.2 Shear Testing Results

ASTM D3518 calculates shear strength from tensile force by simply dividing the tensile stress by two. To obtain the shear modulus, the engineering shear strain was found. Since the testing apparatus could not obtain a strain in the y direction ($\boldsymbol{\varepsilon_y}$), a Poisson's ratio was assumed and $\boldsymbol{\varepsilon_y}$ was calculated. A Poisson's ratio of 0.25 was chosen for the TC940. From here, the shear modulus was calculated over a sampling window of $4000\mu\varepsilon$ from $1500\mu\varepsilon - 5500\mu\varepsilon$. It should be noted that due to the lower range of the engineering shear strain, tightening the sample before the test started induced microstrain in the sampling range before the test started. However, the full sampling window was still within the designated window of observation as specified by ASTM. The true longitudinal strain was then calculated, and the sample window was adjusted to satisfy ASTM standard. The shear stress and engineering shear strain was plotted in Figure 91 and the shear data can be seen in Table 17.

The shear samples experienced a nonlinear elastic stress strain relationship with a ductile failure. When under higher loads, edge fibers and plies began to straighten and delaminate through the thickness. Near peak shear stress, delamination occurred at nearly every ply and tensile failure began radiation though the thickness. The shear strength was found to be 27MPa with a shear modulus of 2.3GPa and strain to failure of 0.0457mm/mm.

Table 17 45º Shear Data

Test Item ID #	Thickness (mm)	Width (mm)	Length (mm)	Shear Modulus (GPa)	Tensile Strength (MPa)	Elongation (%)
S45 Specimen 1	5.910	25.600	76.551	2.467	52.028	4.602
S45 Specimen 2	5.860	25.000	76.699	2.083	52.990	4.641
S45 Specimen 3	5.930	25.530	76.736	2.379	54.681	2.459
S45 Specimen 4	5.870	25.550	76.695	2.070	55.932	6.747
S45 Specimen 5	6.050	25.520	77.195	2.155	53.502	5.226
S45 Specimen 6	5.970	25.600	76.772	2.735	54.749	3.774
Average	5.932	25.467	76.775	2.315	53.980	4.575
Std. Dev.	0.071	0.231	0.219	0.261	1.407	1.432

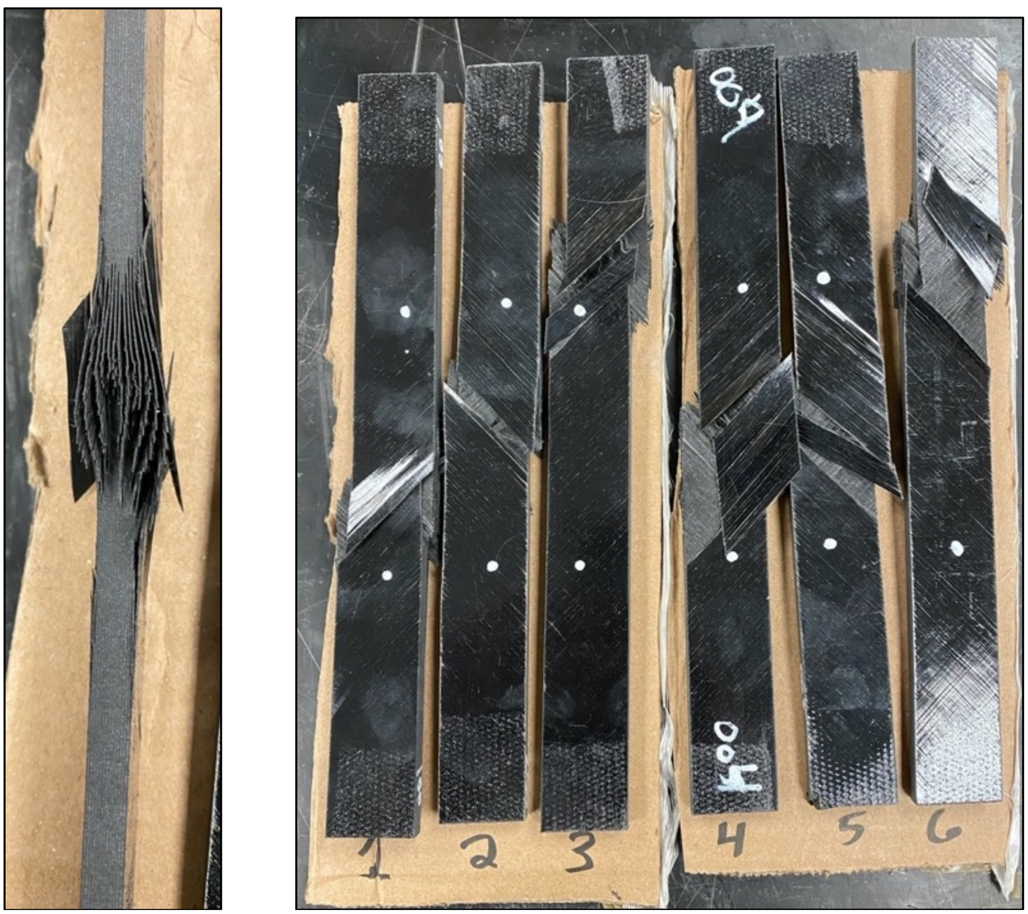

Figure 90 Shear Sample Failures

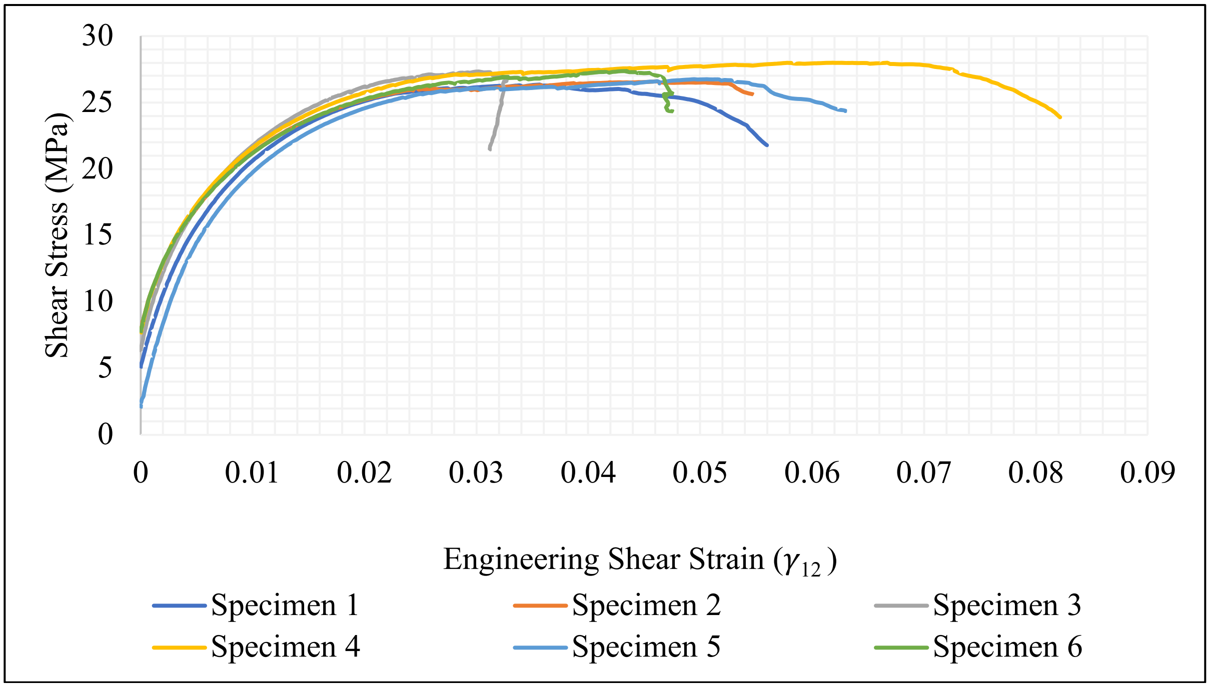

Figure 91 ASTM D3518 Shear Stress Data

6.4 Final Composite Material Card for MAT_054

The quasistatic material characterization data was compiled into a card model (Table 18). MAT_054 allows the utilization of quasistatic mechanical data as damage parameters are used to account for strain-rate effects in high loading rate applications. A guide for the meaning of these parameters can be found in (Table 32 in appendix).

Table 18 LS Dyna MAT_054 Material Card TC940 Thermoplastic (Units of g, MPa, mm, ms)

MID	RO	EA*	EB*	(EC)	PRBA	PRCA	PRCB
	0.00189	3.53e4	6530	6530	0.0185		.5
GAB*	GBC	GCA	(KF)	AOPT	2WAY	TI	
2320	2122	2320					
XP	YP	ZP	A1	A2	A3	MANGLE	
						0.0	
V1	V2	V3	D1	D2	D3	DFAILM	DFAILS
					0	0	0
TFAIL	ALPH	SOFT	FBRT	YCFAC	DFAILT	DFAILC	EFS
1e-7	0	.57	0	2	0	0	.55
XC**	XT**	YC**	YT**	SC**	CRIT	BETA	
378	960	68.2	15.4	70	54.0	0	

Table 18 (cont'd)

PFL	EPSF	EPSR	TSMD	SOFT2			
100.0	0	0	.9	1.0			
SLIMT1	SLIMC1	SLIMT2	SLIMC2	SLIMS	NCYRED	SOFTG	
0.001	0.200	0.001	0.200	1.000	10.000	1.000	

6.5 Interface Characterization

6.5.1 Normal Stress at Failure Characterization

To characterize the maximum normal stress at failure of the interface, a butt joint was made and tested under ASTM 2095 Test Method for Tensile Strength of Adhesives by Means of Bar and Rod [81]. One-half inch 7075-T6 aluminum rod was cut into 50.8mm lengths and grit blasted for surface preparation of the aluminum-to-aluminum samples. 12.7mm thick PET/GF composite unidirectional rod was lathed to 12.7mm and cut into 50.8mm lengths in a similar process to the compression samples. A 3D printed fixture was used to allow concentric adherence between butt joints. The original length of the 3D printed fixture was measured with the adherend rods directly in contact. A 0.76mm bond line thickness was then added to the found measurement. The adhesive was then applied in the joint and the butt joint fixture was tightened to the final measurement accounting for the bond line thickness. After curing, the butt joints were sanded on the sides exposing only the axial bond line thickness and verification measurements were made.

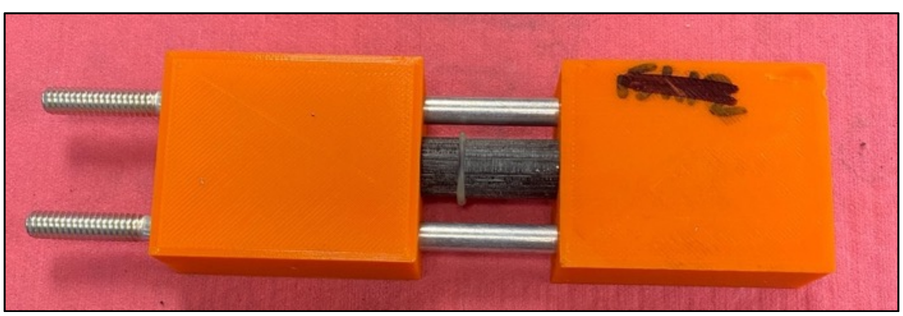

Figure 92 Butt Joint Fixture

6.5.2 Normal Stress at Failure Results

Both aluminum and composite butt joint testing was performed on an Instron 5984 universal testing system with 150kN load cell (0.5% tolerance) and 150kN wedge action grips with 0-12.7mm cylindrical rod jaw inserts. It should be noted ASTM D2095 specifies a speed of testing that is load rate dependent of 16.5MPa-19.3MPa of bond area per minute. However, the Instron machine was determined to be unable to perform that load rate specification. Instead, the specimens were pulled at a crosshead displacement of 1.27mm/min until failure and the displacement, force and normal stress was recorded. After fracture, failure modes were observed and recorded. The aluminum to aluminum joint experienced adhesive failure and the composite to composite was a substrate failure. Both failure mechanisms were deemed satisfactory as it pertains to the limiting strength at the interface.

Table 19 Aluminum-Aluminum Butt Joint Testing

Test Item ID #	**Diameter (mm)**	**Max Displacement (mm)**	**Max Force (kN)**	**Tensile Stress at Break (MPa)**
AlBJ Specimen 1	12.700	0.644	3.236	25.542
AlBJ Specimen 2	12.700	0.374	2.599	20.514
AlBJ Specimen 3	12.700	0.449	2.927	23.104
AlBJ Specimen 4	12.700	0.490	2.543	20.072
AlBJ Specimen 5	12.700	0.416	3.192	25.194
AlBJ Specimen 6	12.700	0.384	2.883	22.756
AlBJ Specimen 7	12.700	0.237	2.815	22.222
Average	12.700	0.428	2.885	22.772
Std. Dev.	0.00	0.124	0.265	2.095

Table 20 Composite-Composite Butt Joint Testing

Test Item ID #	**Diameter (mm)**	**Max Displacement (mm)**	**Max Force (kN)**	**Tensile Stress at Break (Mpa)**
CBJ Specimen 1	12.750	0.099	1.417	11.094

Table 20 (cont'd)

CBJ Specimen 2	12.750	0.781	1.432	11.214
CBJ Specimen 3	12.580	1.473	1.599	12.867
CBJ Specimen 4	12.350	0.907	1.556	12.985
CBJ Specimen 5	12.660	0.633	1.616	12.838
Average	12.618	0.815	1.501	12.040
Std. Dev.	0.166	0.496	0.094	0.957

Figure 93 Butt Joints Right: Aluminum Interface, Left: Composite Interface

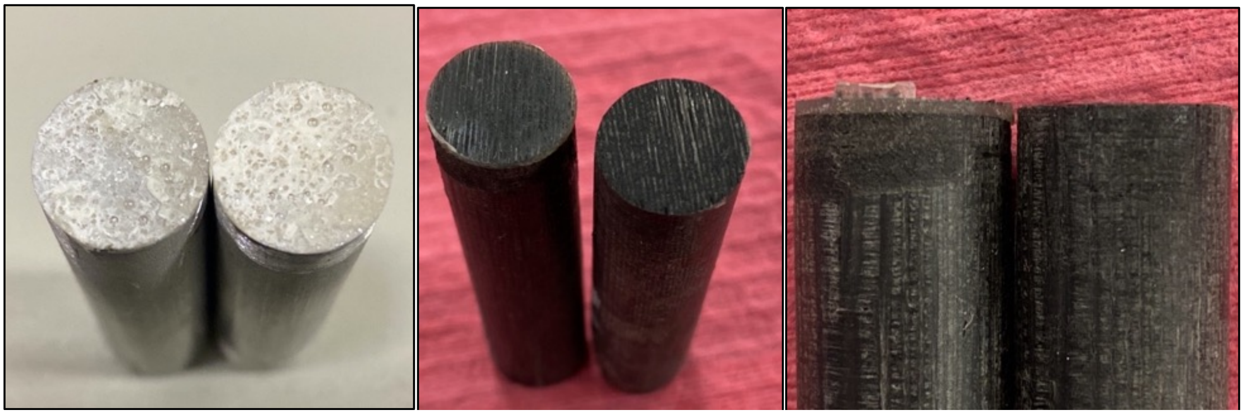

Figure 94 Failure Modes Left: Aluminum Interface, Right Composite Interface

6.5.3 Shear Stress at Failure Characterization

To characterize the maximum shear stress at failure, lap shear specimens were manufactured in accordance with ASTM D1002 Standard Test Method for Apparent Shear Strength of Single-Lap-Joint Adhesively Bonded Metal Specimens by Tension Loading [82] and US Army Research Laboratory's (ARL's) ARL-ADHES-QA-001.00 rev 2.2 [83] standard for evaluating adhesives.

For the aluminum-aluminum interface, a sheet of 2024-T3 of 1.62mm thickness was wire electrical discharge machined into template sheets of coupons still rigidly linked. The aluminum coupons were then grit blasted on both sides and wiped clean with isopropyl alcohol. The specimens were then manufactured using the ARL defined single lap shear fixture for a final bond area of 25.4mm wide by 12.7mm long with a bond line thickness of 0.76mm. A single coupon plate was placed within the pins on the bottom half of the fixture. A spacer plate of the thickness of the coupon plate (1.62mm) and the desired bond line thickness (0.76mm) was placed in the pins on the other side of the bottom half of the fixture. From here, another spacer plate was added on top of the coupon plate to of the same thickness (2.38mm) as the spacer plate. The adhesive was then applied to the coupon sheet ensuring no air entrainment in the half inch wide adherence area. The final coupon plate was then placed within the pins on the opposite side of the coupon with the applied adhesive. The top fixture component was then placed within all the pins and gently placed onto the lap shear set up allowing proper consolidation. The adhesive was left within the fixture for 48 hours and removed. An Axitom abrasive saw was then used to cut the ridged links to each lap shear specimen. Excess adhesive was removed, and the specimens were analyzed for manufacturing defects and proper bond line thicknesses.

6.5.4 Shear Stress at Failure Results

Aluminum lap shear testing was performed on an Instron 5984 universal testing system with 150kN load cell (0.5% tolerance) and 150kN wedge action grips. The specimens were pulled at a crosshead displacement of 1.27mm/min until failure and the displacement, force and shear stress were recorded. After fracture, failure modes were observed and recorded. Failure was seen as an interfacial failure. Normally, this would lead to inconclusive data on the adhesive strength, since the material model requires interfacial shear strength, this failure is acceptable.

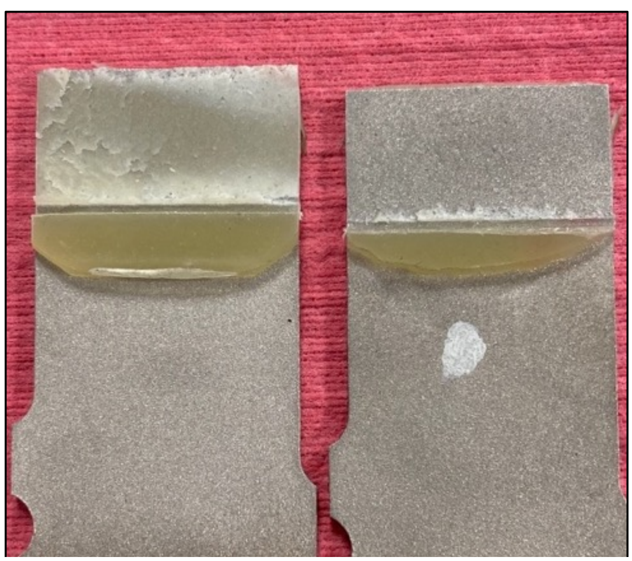

Figure 95 Aluminum Lap Shear Failure Mode

Table 21 Aluminum-Aluminum Lap Shear Data

Test Item ID#	Joint Width (mm)	Joint Length (mm)	Displacement (mm)	Force (kN)	Shear Stress (MPa)
ALS Specimen 1	25.40	12.70	1.8088	7.5642	23.4490
ALS Specimen 2	25.40	12.70	1.4910	7.0757	21.9348
ALS Specimen 3	25.40	12.70	1.4615	7.7611	24.0596
ALS Specimen 4	25.40	12.70	1.5773	7.5844	23.5117
ALS Specimen 5	25.40	12.70	1.6449	7.9462	24.6332
Average	25.40	12.70	1.5967	7.5863	23.5176
Std. Dev.	0.00	0.00	0.1388	0.3245	1.0060

For the composite-composite interface, a plate of $[0_5/90/0/90/90/0/90/0_5]$ TC940 was manufactured. The ply bias for the 0° direction was needed due to shear lag causing ply rupture in preliminary testing. In a [0/90] stack up, the adhesive fractured the 90° ply and caused the now ruptured ply to break away from the underlying 0° ply. The bias ply stack up allowed for the 0° plies to be completely loaded with the shear strength reducing premature rupture. The 4.25mm panel was cut in half transversely across the 0° fibers. Surface preparation for the composite consisted of light sanding with 400 grit sandpaper. When sanding, mindful consideration was considered to not excessively damage the underlying glass fibers. A matte finish was obtained and deemed suitable for better adhesion. In a similar set up to the ARL aluminum lap shear joints, spacer plates of identical thickness to the composite substrate (4.25mm) and the desired bond line thickness (0.76mm) were used to align the two composite components into a single lap shear joint. Due to the increased thickness of the sample, it was determined that grip tabs were needed to reduce any specimen torquing under asymmetric tensile loading. The included tabs allowed pure axial loading onto the shear interface. However, ASTM D5868 Standard Test Method for Lap Shear Adhesion for Fiber Reinforced Plastic Bonding was followed for test specimen dimensions and construction. ASTM D5868 specifies a 25.4mm square bond area, over the 12.7mm by 25.4mm bond area for metallic substrates in the ARL standard. Adhesive was applied to the matte finished area and the plates were pressed and consolidated with weight. The adhesive was left for 48 hours of curing and then removed. An Axitom abrasive cutting saw was used to cut the lap shear panel into 25.4mm strips. The samples were analyzed for manufacturing defects and the bond line thickness was verified.

Figure 96 Manufactured Composite Lap Shear Specimen

Composite lap shear testing was performed on an Instron 5984 universal testing system with 150kN load cell (0.5% tolerance) and 150kN wedge action grips. The specimens were pulled at a crosshead displacement of 13mm/min until failure and the displacement, force and shear stress were recorded. After fracture, failure modes were observed and recorded. Failure was observed to be within the ply of composite. ASTM D5573 Standard Practice for Classifying

Failure Modes in Fiber-Reinforced-Plastic (FRP) Joints specifies light fiber tear (LFT) as an acceptable mode of failure when characterizing composite single lap joints. Since the failure occurred within the composite, the composite-composite interlaminar shear strength was obtained.

Figure 97 Composite Lap Shear Light-Fiber-Tear Failure

Table 22 Composite-Composite Lap Shear Data

Test Item ID#	Joint Width (mm)	Joint Length (mm)	Displacement (mm)	Force (kN)	Shear Stress (MPa)
CLS Specimen 1	27.36	26.75	3.0381	3.2624	4.4576
CLS Specimen 2	27.12	27.12	1.1647	3.9189	5.3283
CLS Specimen 3	27.8	27.47	1.6121	3.6357	4.7608
CLS Specimen 4	27.32	26.29	1.3629	3.2335	4.502
Average	27.40	26.91	1.7945	3.5126	4.7622
Std. Dev.	0.29	0.51	0.8491	0.3270	0.4004

At this point the adhesive interfaces were well characterized and the contact cards were created for the tie break constraints at the composite and aluminum interfaces. (Table 23 and 24).

Table 23 LS Dyna Contact_Tiebreak Material Card Composite Interface (Units of MPa)

NFLS	SFLS	TBLCID	THKOFF
12.040	4.76	0	0

Table 24 LS Dyna Contact_Tiebreak Material Card Aluminum Interface (Units of MPa)

NFLS	SFLS	TBLCID	THKOFF
22.772	23.517599	0	0

Chapter 7 Model Validations

Two finite element models were created using LS Dyna for the monolithic 7075-T6 plates as well as the composite-metal hybrid panels. The material was modeled with the simulated ALE shock tube model in the same experimental set up as the shock tube experiments. The models served to validate deflection measurements as well as help explain damage characteristics in each material panel.

7.1 Johnson-Cook Model Validation

Figure 98 shows the aluminum deformation over time. The aluminum initially experienced localized deflection where the initial high-pressure area impinged the plate as shown in the pressure films. As the panel continued to deform, the deflection profile broadened until reaching peak deflection. At peak deflection, the cross-sectional profile led to a smooth and consistent curve. After rebound and elastic attenuation, the localized deflection bulge is seen as the material retreats into its final position.

Utilizing the effective strain-time history in LS Dyna an approximate strain rate of $145s^{-1}$ was calculated. This strain rate regime is considered a high strain rate and is within the approximate strain rate of a blast event.

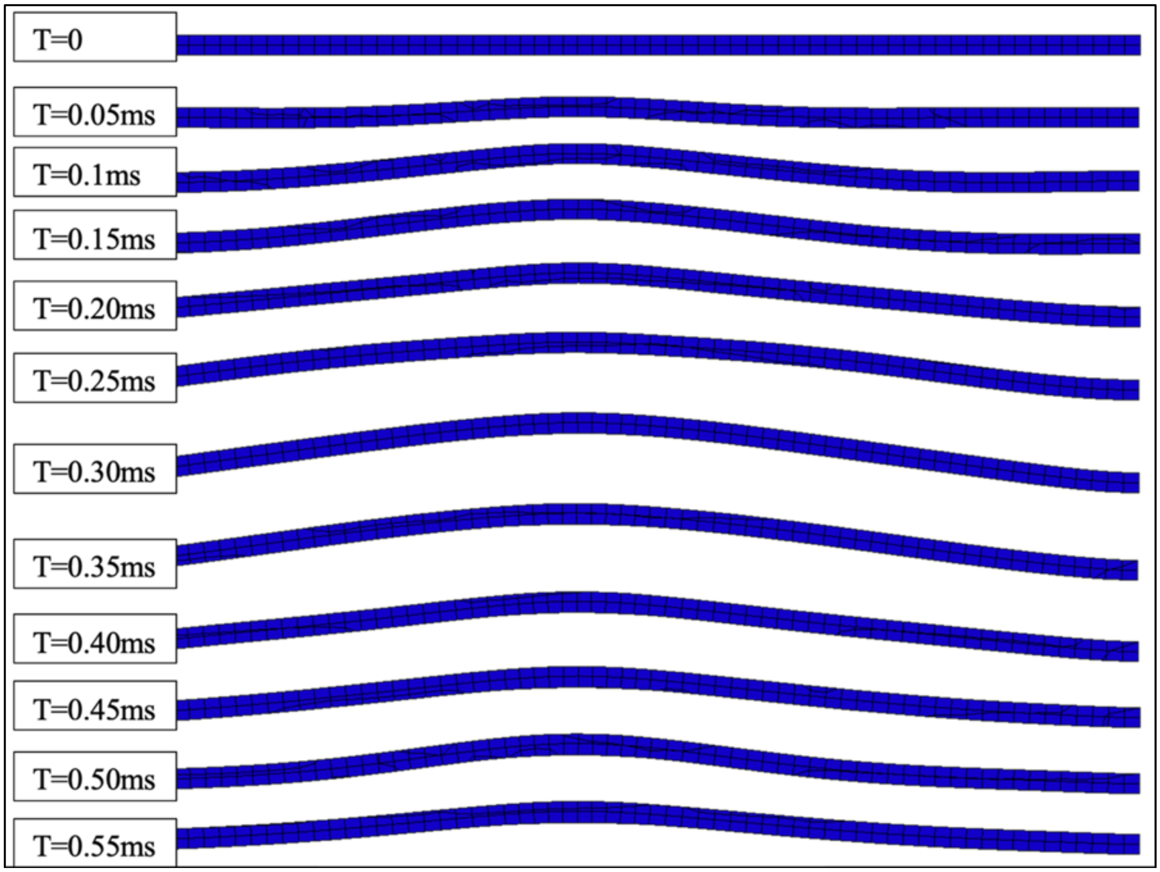

Figure 98 Cross Sectional View of Deflection over Time

The LS Dyna model of the 3.175mm monolithic plate matched the dynamic and permanent deflection recorded in the experiments well. The Johnson-Cook model predicted a dynamic deflection of 10.15mm compared to the average of 9.89mm an error of 2.63% and permanent deflection of 5.31mm and compared to the average recorded 4.96mm, an error of 7.06%. However, from the cross-sectional displacement profile across the center of both peak and permanent deflections when compared to fringe projection measurements shows tighter agreeance toward the outside and edges.

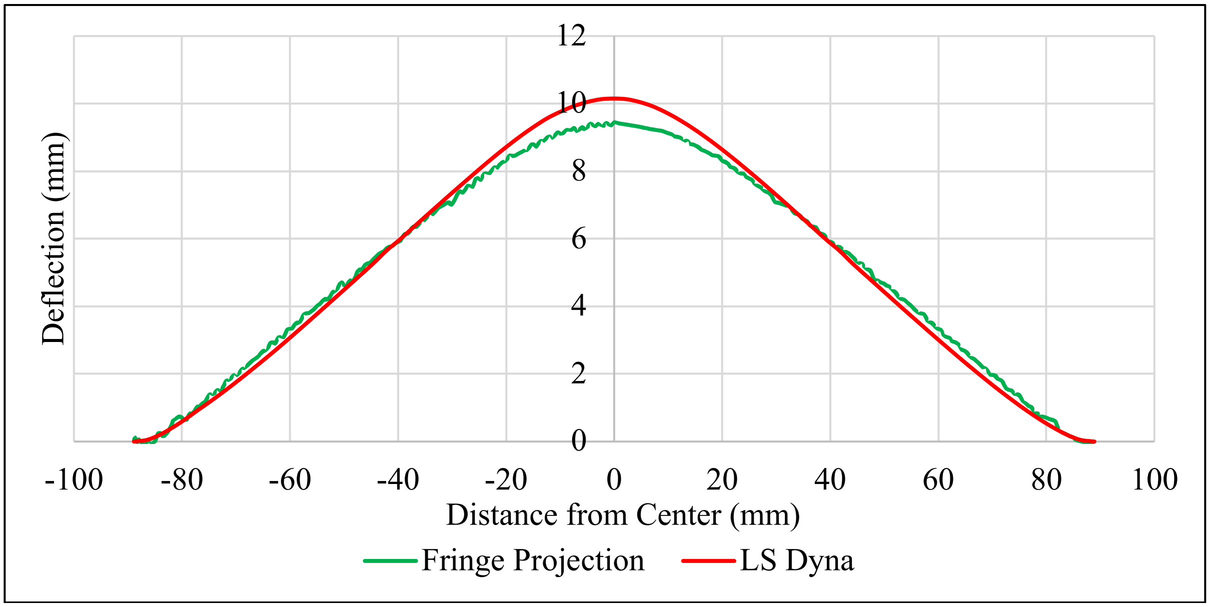

Figure 99 Fringe Projection Vs. LS Dyna Cross Sectional Displacement for Monolithic Aluminum Plate 4 at Peak Deflection

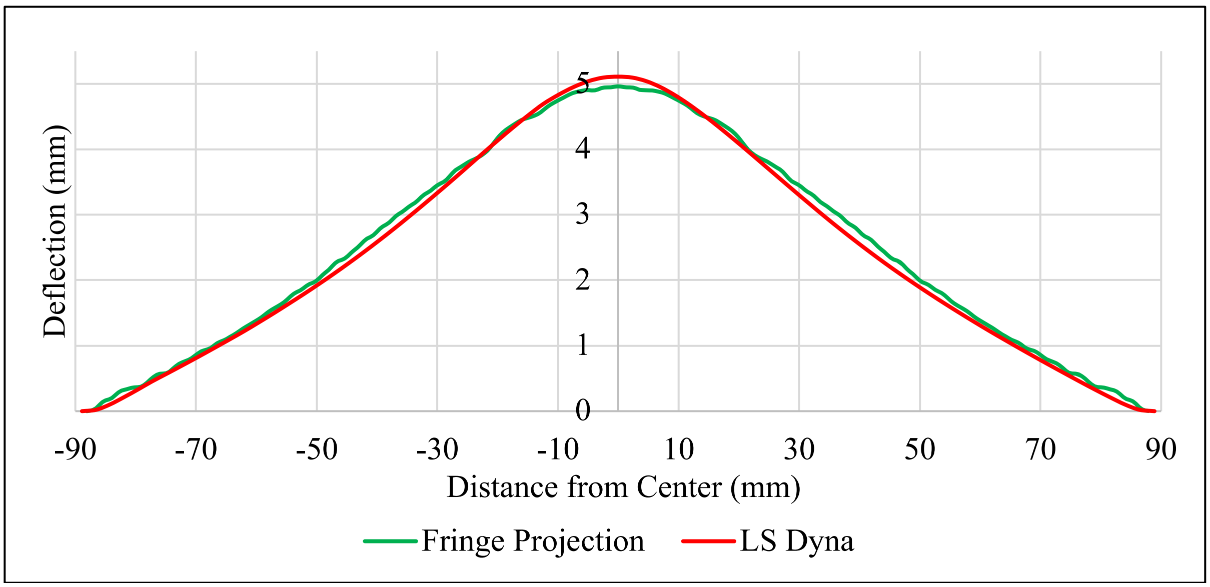

Figure 100 Fringe Projection Vs. LS Dyna Cross Sectional Displacement for Monolithic Aluminum Plate 4 at Permanent Deflection

The permanent deflection portrays the plastic strain accumulated within the aluminum plate throughout the experiment. From initial yielding to maximum dynamic deflection, the aluminum panel accumulated the entirety of its effective plastic strain. After this point, all deflection reverberations were due to elastic rebounding. Figure 101 shows the effective plastic strain accumulated in the material after peak deflection. As previously described in the experimental profiles, the localized area of higher deflection toward the center of loading is due to a higher amount of plastic strain leading to an inconsistent increase in deflection in the permanent deformation profile seen in Figure 100.

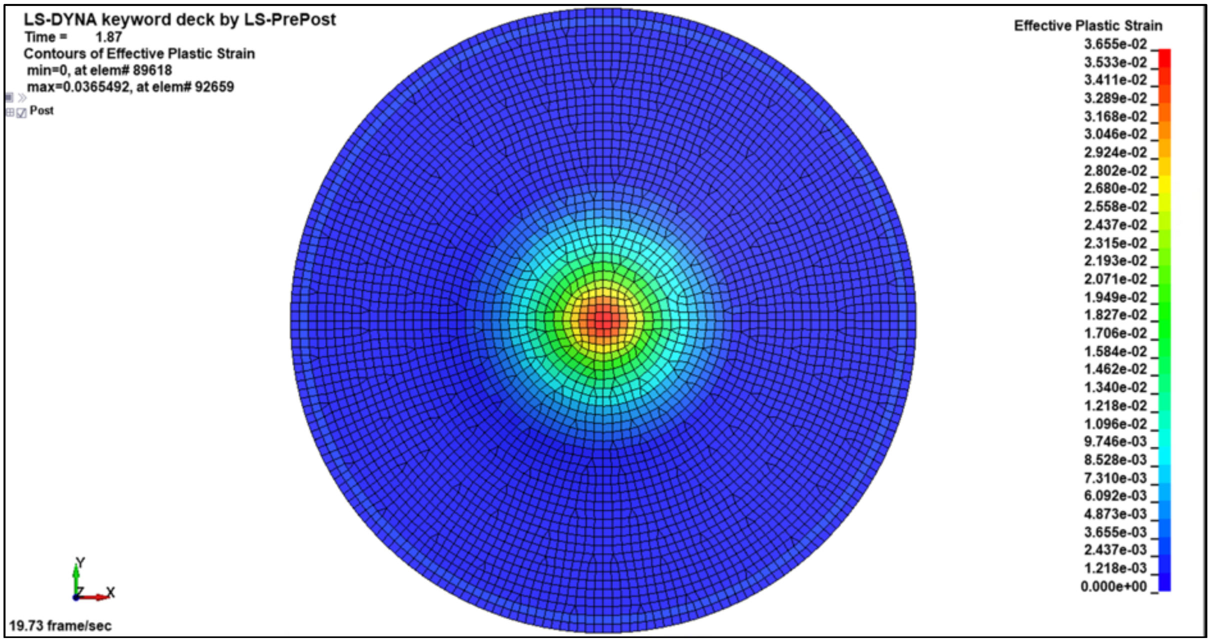

Figure 101 Effective Plastic Strain in Monolithic Aluminum

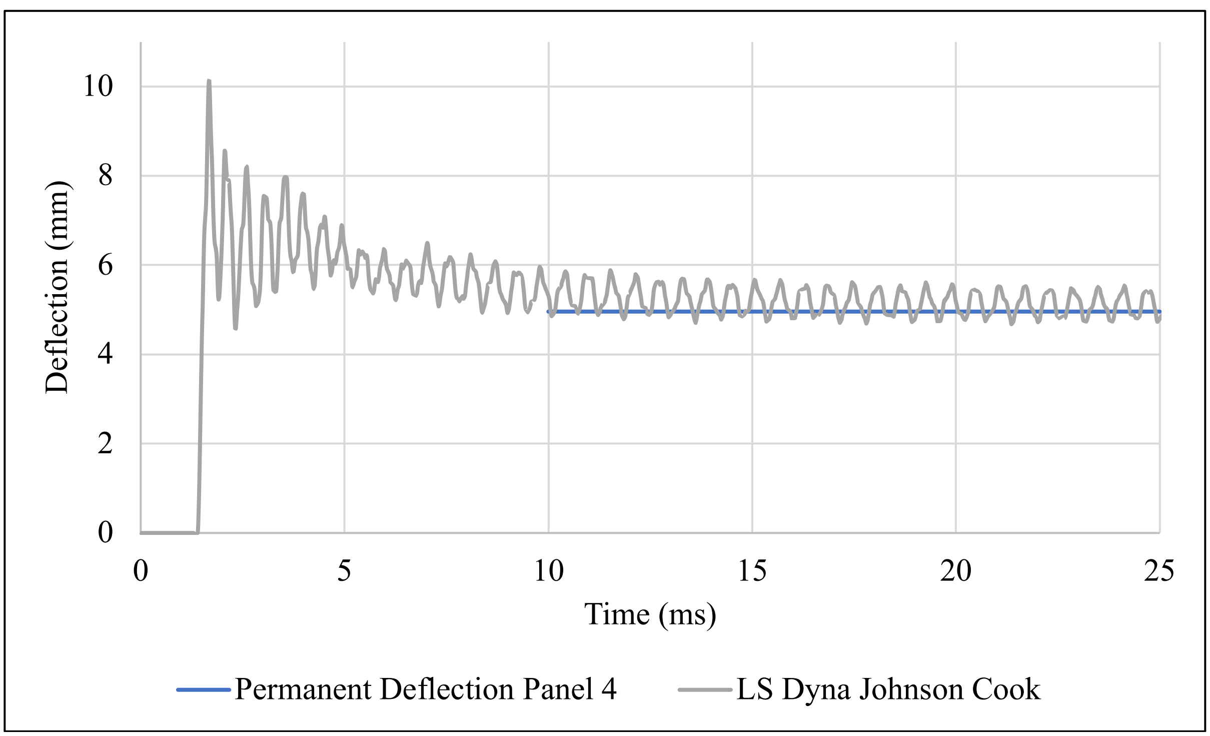

Figure 102 Time-Deflection History LS Dyna Johnson-Cook

7.2 Hybrid Panel Model Validation

When assessing the MAT_054 model, multiple observations can be drawn from the simulation calculated by the model. The MAT_054 model was calibrated and designed to capture delamination, deflection, and damage. The model was analyzed through the cross section in both the 0° and 90° directions. The sequential images (Figure 103) taken from the simulation illustrate the deformation characteristics over time.

Almost instantly, delamination began to in the 1st and 2nd ply interface upon initial plate bending before peak deflection (Figure 108). This delamination was driven by shear failure within the ply. As the paneled continued to deform under load, the extent of delamination between the 1st and 2nd interfaces propagated along the entire cross-section of the panel and delamination began to occur in all remaining intact plies (2-13). This behavior was observed in the characterization in the lap-shear tests for the shear failure at the interface. In every lap shear specimen, the first ply remained completely adhered to the underlying adhesive and led to substrate failure (Figure 97). It is no coincidence that these behaviors are seen in both applications. The adhesive has a stronger adherence to the composite as the composite does to itself leading to consistent failure within the composite rather the interface. Carrying on, the composite shear failure dictated all delamination in the composite. Upon complete separation of the 1st and 2nd plies, the composite plies consisting of intact plies 2-13 was trusted upwards as the underlying intact layers consisting of aluminum, adhesive and composite ply 1 began to rebound. Now independent, the aluminum experienced a *local* maximum deflection as the composite continued to deform until abruptly being stopped at the panels *global* peak deflection (i.e., governed by the delaminated block of composite plies). The composite plies then rebounded where the extent of delamination was easily observed as the layers began to physically separate in space. During the composites descent, the aluminum panel of material started its second ascent causing the aluminum and composites to collide. The composite plies were then trusted upwards and the process repeated until the material system was attenuated.

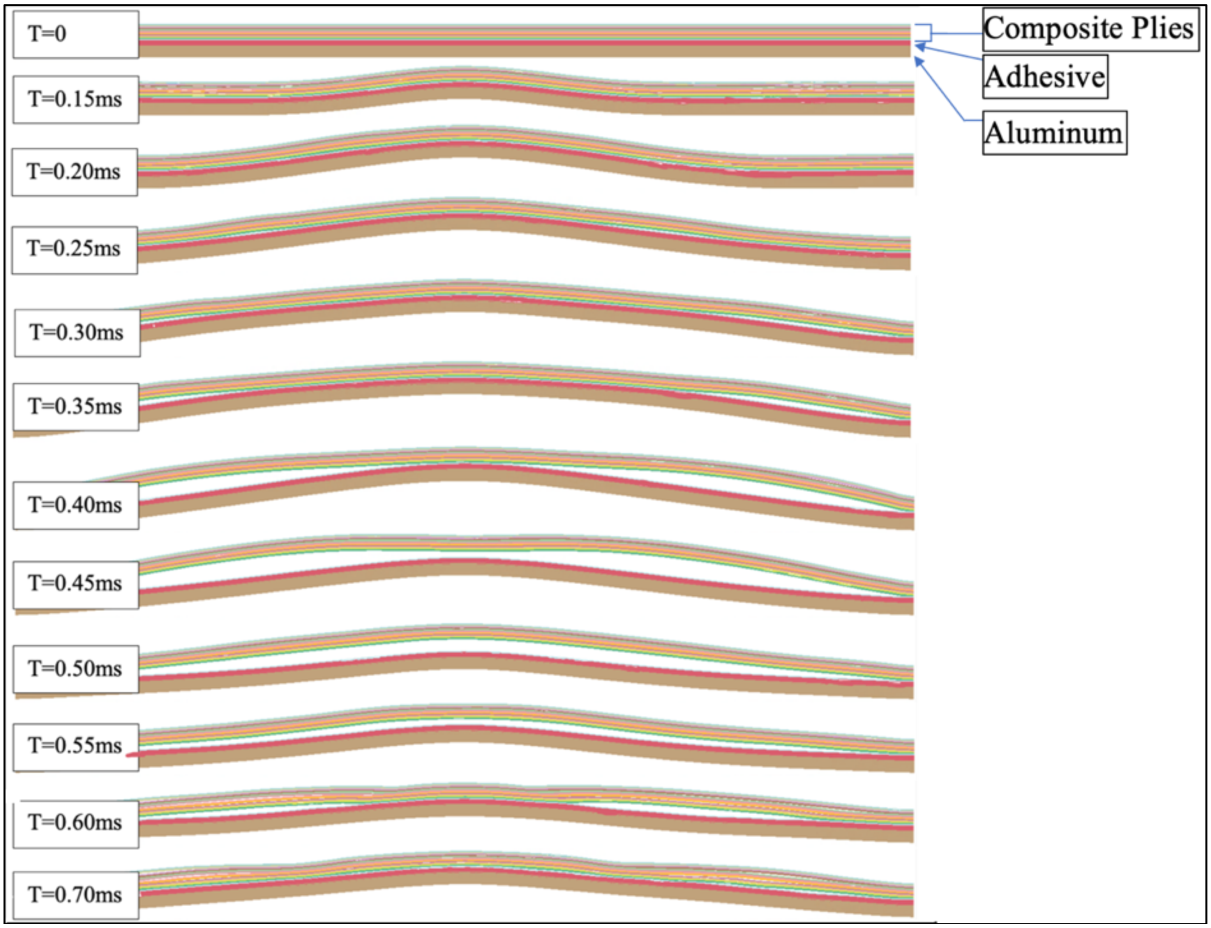

Figure 103 Cross Sectional View of Deformation and Delamination Over Time

As the material dampens, the aluminum dictates the permanent deflection. Due to the accumulation of plastic strain within the aluminum (Figure 104), it permanently remains deformed. Though delaminated, the individual composite plies never reach their failure limit. With no complete failure observed in the model and experiments, the composite then settled into the aluminum. However, the delamination throughout the composite caused "fluff" as the composite plies settled in an unconsolidated manner. The extent of delamination seen in the LS

Dyna model (Figure 108, 109, 110 and 111) correlates with the C-Scans and the delamination seen in figure 56 and 57. The composite backing had a role in reducing the plastic stain accumulation within the aluminum. Even though the composite was severely delaminated near peak deflection, it provided enough structural support to reduce the plastic accumulation for the front plate of aluminum which was thinner than that of the monolithic plate. In total the maximum accumulated plastic strain within the monolithic plate was 0.0365 whereas the accumulated strain within the hybrid panel aluminum plate was 0.0278, a 27% reduction.

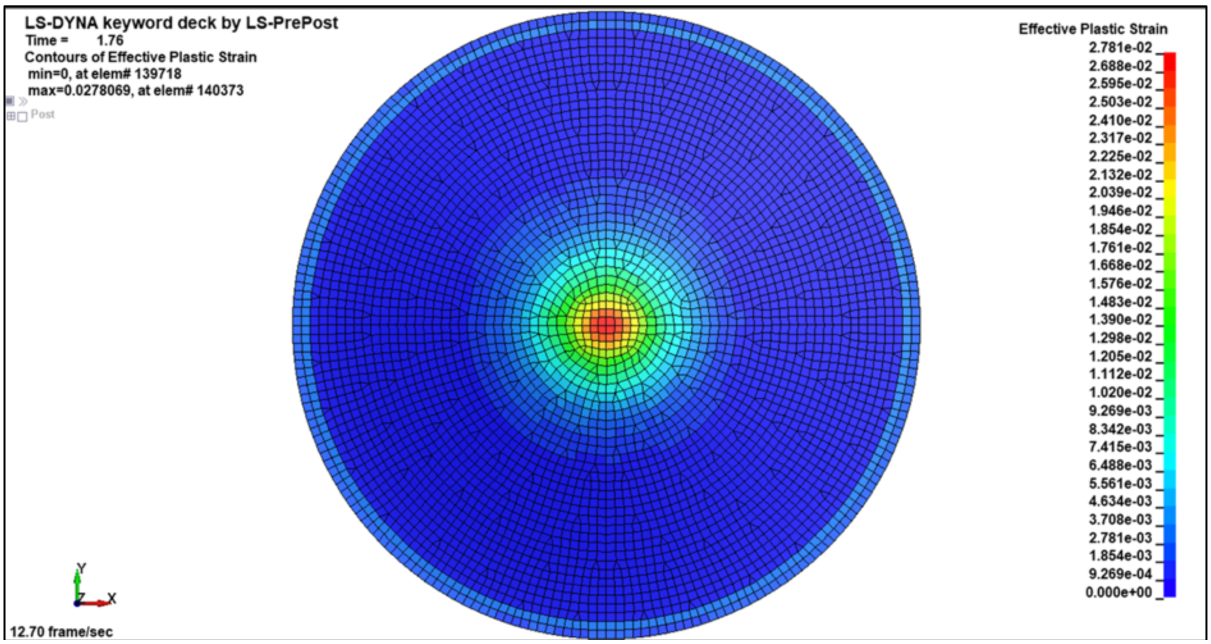

Figure 104 Total Effective Plastic Strain in Aluminum

LS Dyna predicted a peak displacement of 9.93mm, compared to the averaged 10.95mm of deflection recorded via fringe projection methods, a 9.3% deviation at the peak. However, like the monolithic aluminum, the model strongly correlates to the deflection profile 30mm away from the center to the clamped edge. LS Dyna predicted a permanent deflection of 5.00mm compared to the averaged 4.71mm, a 5.8% deviation. Furthermore, the prediction correlates strongly through the entire cross section.

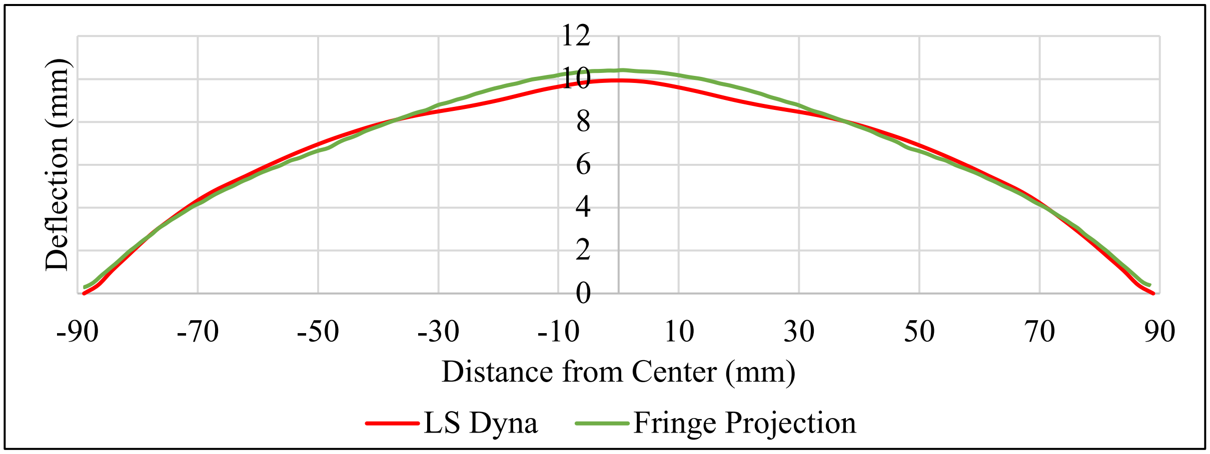

Figure 105 Fringe Projection Vs. LS Dyna Cross Sectional Displacement for HP5 4 at Peak Deflection

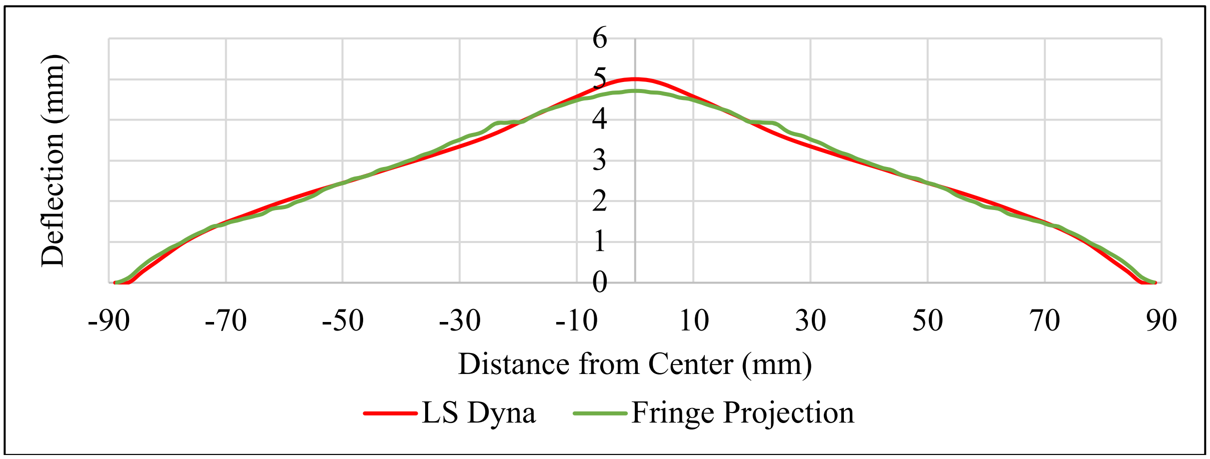

Figure 106 Fringe Projection Vs. LS Dyna Cross Sectional Displacement for HP5 at Permanent Deflection

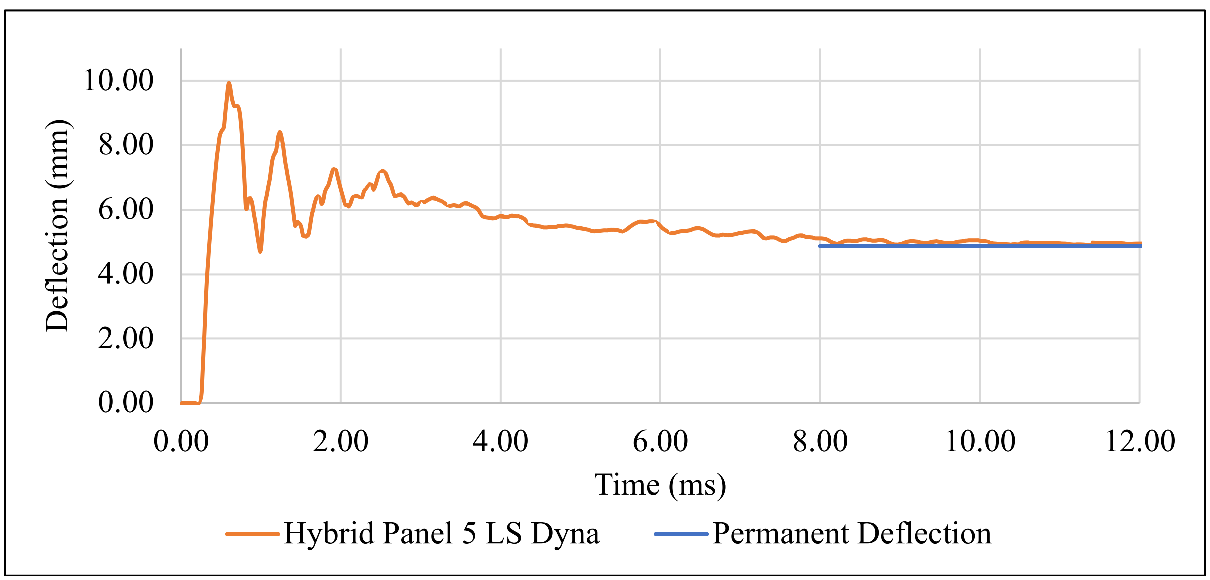

Figure 107 LS Dyna Deflection-Time History

Figure 110 and Figure 111 depict the area LS Dyna flagged as delaminated. Recalling the failure criterion:

$$\left(\frac{\sigma_n}{NFLS}\right)^2 + \left(\frac{\sigma_s}{SFLS}\right)^2 > 1$$

all elements whose failure envelope was calculated to be less than a value of one were considered intact and assigned a blue fringe. All surface segments over one were considered failed and assigned the red fringe. Failed interfaces were considered independent by the model and allowed to freely move and slide with friction.

As observed in the experimental panels, the modeled interfaces between the aluminum and adhesive, and adhesive to the first composite ply remained 100% intact. However, the interface between the 1st and 2nd composite plies was 100% delaminated within the unclamped section and loaded section. Plies 2-13 show delamination characteristics consistent with the cross-sectional view of the deflection-time history shown in Figure 103, Figure 108 and 109. The delamination patterns for the 0° and 90° plies shown in Dyna are classic of those of impacted unidirectional [0/90] composites [84]. The failed areas follow a “peanut” shape as lobes of intact material span in the direction of the fibers. Both 0° and 90° plies experience this directional behavior as shown in Figure 110 and 111 where red depicts delamination and blue depicts areas of the interface which remain intact.

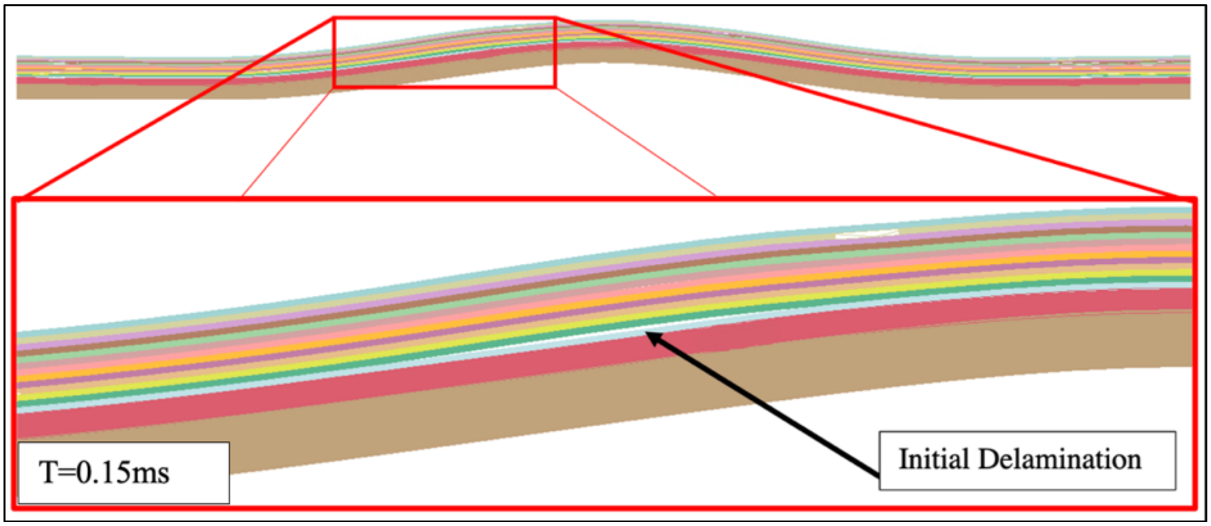

Figure 108 Initial Site of Delamination

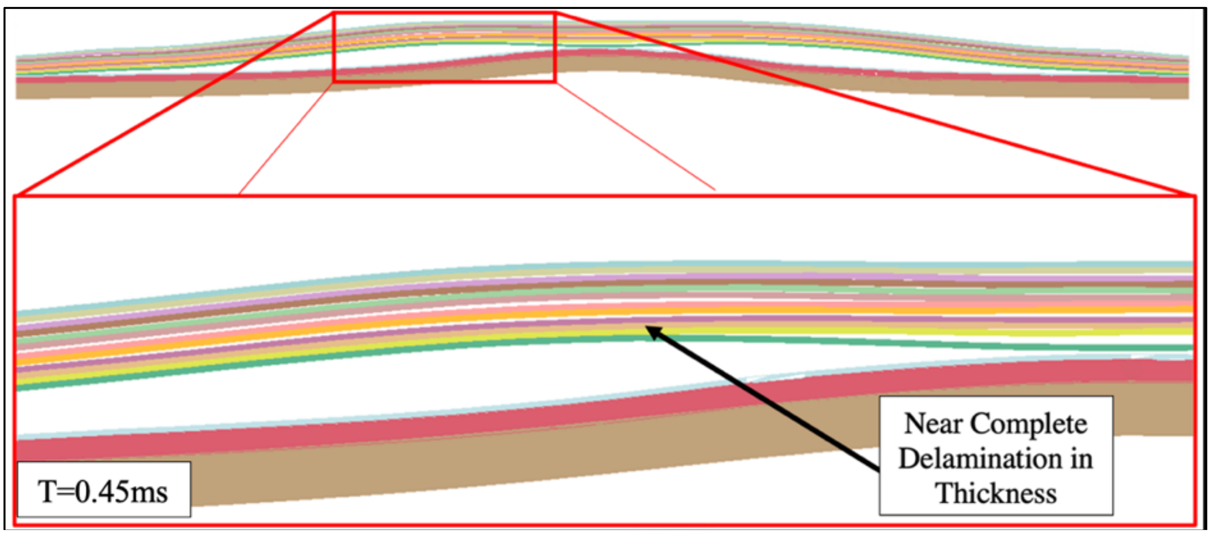

Figure 109 Extent of Delamination

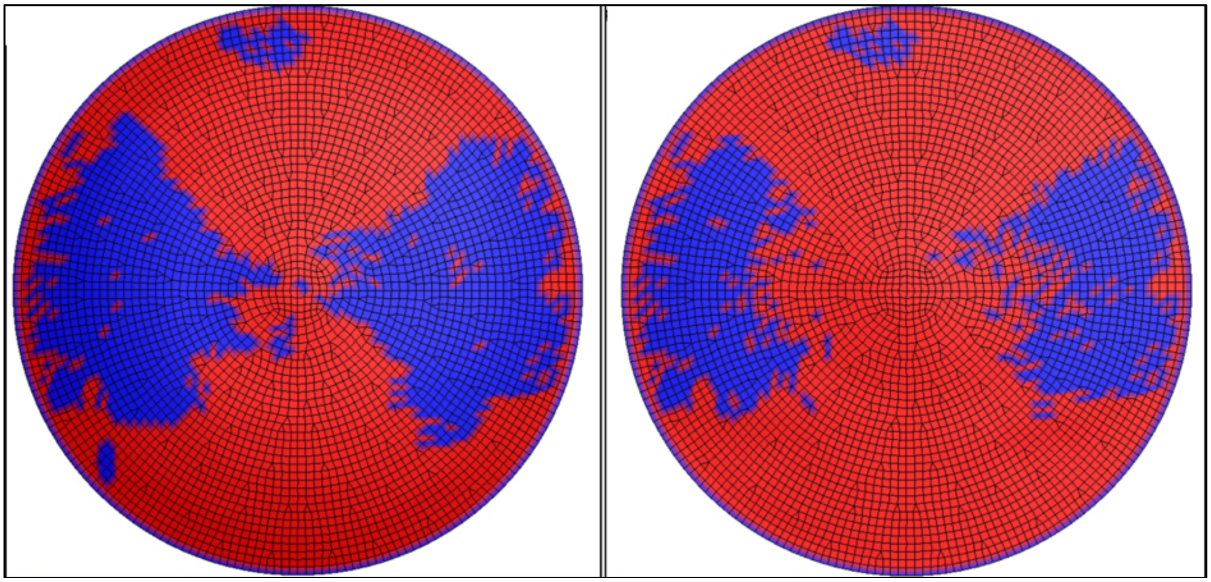

Figure 110 Delamination in a 90° Ply at Permanent Deformed State Left: Peak Right: Permanent

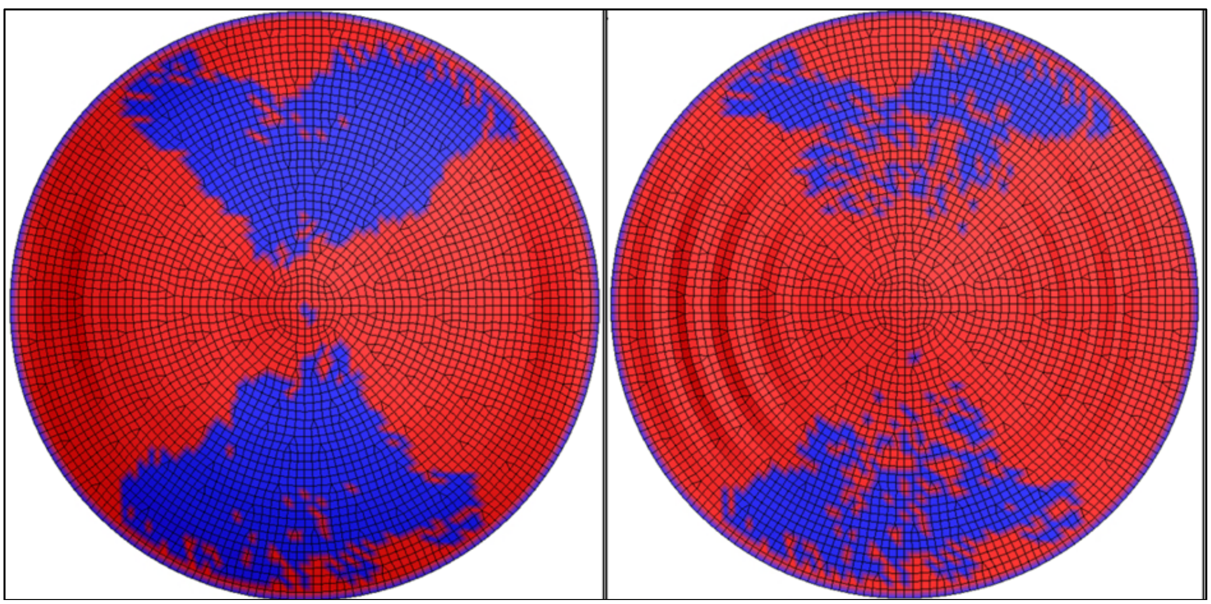

Figure 111 Delamination for 0° Ply at Permanent Deformed State Left: Peak Right: Permanent

Table 25 shows the percentage of delamination by area throughout the thickness as given by the at rest LS Dyna model.

Table 25 Final Delamination Area Per Ply

Interface	Percent Delaminated
Aluminum-Adhesive	0
Adhesive-Ply 1	0
Ply 1 – Ply 2	100
Ply 2 – Ply 3	78
Ply 3 – Ply 4	78
Ply 4 – Ply 5	61
Ply 5 – Ply 6	91
Ply 6 – Ply 7	52
Ply 7 – Ply 8	69
Ply 8 – Ply 9	59
Ply 9 – Ply 10	64
Ply 10 – Ply 11	64
Ply 11 – Ply 12	92
Ply 12 – Ply 13	18

Chapter 8 Summary of Work

This work looked to characterize a single bonded interfaced composite metal hybrid panel under high pressure loadings. Experimental characterizations on a Stalker type tube were made, tailoring the resultant pressure loading to a Friedlander like blast profile using set initial pressures, piston weight, nozzle diameter and diaphragm rupture strengths. The initial pressure loading profile was improved by understanding the mechanics of the Stalker type tube. The final obtained pressure profile was representative of a Friedlander profile. An LS Dyna was made to capture the kinematics of the shock tube. By assuming the conditions near diaphragm rupture, and characterizing the compression piston motion, a representative pressure profile was developed to later load the material models and simulate the entire experiment.

The pressure time history and the peak pressure distribution over the plate were captured and validated with a piezoelectric sensor and pressure sensitive film. A manufacturing process was detailed on the hot press consolidation of a PET thermoplastic glass fiber reinforced composite. Furthermore, a detailed process of the manufacturing of the single interfaced composite metal hybrid panel was created. The composite metal hybrid panels and monolithic baseline plates were experimentally tested with the obtained pressure profile. Fringe projection analysis was conducted and quantified the peak dynamic deflections of both the hybrid and monolithic plates.

Post load observations were made on the damage imposed by both material systems. The monolithic plate experienced permanent plastic deformation of 4.96mm and a dynamic deflection of 9.89mm. The hybrid panels experienced permanent deflections of 4.87mm and a dynamic deflection of 10.95mm. The hybrid panels experienced plastic deformation in the aluminum front plate and delamination throughout the entire composite.

A LS Dyna finite element model for the monolithic and hybrid panels was created. The monolithic plate Johnson-Cook model described the base plate very well. The permanent deflection had an error of 7.08% of the experimentally measured permanent deflection, and 2.63% error when compared to the dynamic deflection however, the entire cross-sectional displacement shows good agreement. Overall, the Johnson-Cook model validated the in-situ and post pressure loaded samples remarkably well. The Johnson-Cook model was then implemented in the hybrid panel model for further material system validations.

Modeling the hybrid panels required multiple material cards. LS Dyna material card MAT_054 was created to illustrate and better explain phenomena happening in the composite during the pressure loading. To develop the MAT_054 material card, an extensive material characterization was needed to quantify the PET/GF under tensile, compressive and shear loading. To model the adhesive interface, a generic MAT_001 elastic model was used with the material properties of the adhesive given from Plexus. As previously mentioned, the validated LS Dyna MAT_098 Simplified Johnson-Cook card implemented to capture the behavior of the 7075-T6 aluminum front plate. Values obtained in literature were implemented in both the hybrid panel model, as well as the monolithic plate model. Delamination was experienced in the experimental tests and thus, needed to be modeled in LS Dyna. Contact_Tie_Break cards were implemented at each interface of the hybrid model and failure criteria was implemented with experimentally derived normal and shear stresses at failure values.

The MAT_054 model was calibrated to depict the damage mechanisms seen in the composite both visually and by c-scan. The model showed that the composite delamination was attributed to the collision of a composite block of intact plies and the adhesive and aluminum underlying material. Due to an initial delamination, and mismatching stiffnesses, the composite was delaminated at the first ply and thrusted away from the underlying material. As the underlying material rebounded back and experienced its second oscillation of backwards deflection, the composite was still on its initial forward rebound when both materials systems, collided. The composite instantly and completely delaminated and the underlying aluminum and adhesive, immediately began another cycle of forward displacement. The process repeated until the system was dampened to the point of no further deflection. Due to the complete delamination of every composite ply, “fluff” was experienced within the composite and thus lead to a slightly higher deflection that the baseline monolithic material. The composite backing dictated the deflection panel and was driven by the aluminum within the experiment. Overall, the model agreed with delamination and deflection data. LS Dyna predicted a peak deflection of 9.93mm compared to the experimentally averaged 10.95mm, a 9.3% deviation from the calculated average. The permanent deflection predicted by the model was 5.00mm, compared to the experimentally derived average of 4.71mm, a 5.8% deviation. However, the deviations at the peak are misleading as the entire cross sectional behavior nearly matched the experimentally derived results. When assessing the delamination extent, both C-Scans and destructive analysis revealed heavy delamination throughout the entire composite. However, in the model as well as the destructive analysis, delamination was not experienced in the first composite ply alluding to the assumption shear was the main driver for delamination within the composite.

The composite behavior was purely driven by shear. The LS Dyna model depicts the higher peak deformation was caused by a large delamination between the 1st and 2nd plies. However, even though the composite experienced extensive delamination, the individual plies remained intact when visually inspecting the panels. The composite backing had a role in reducing the plastic stain accumulation within the aluminum. Interestingly enough, even though the composite was severely delaminated near peak deflection, it provided enough structural support to reduce the plastic accumulation in the hybrid aluminum by 27% compared to the thicker monolithic plate.

Chapter 9 Future Research and Application

Though the CVRC shock tube is able to test material under blast like conditions, i.e. high strain rates, the system still lacks the ability to shock the material like a blast wave. Causing the pressure in the shock tube is the expelled compressed gas and not a single shock wave. Future work for this material system and others alike could be a great addition for the Engineering Research Complex (ERC) Advanced Blast Chamber (ABC) which uses a logarithmic spiral in a large cross sectional blast chamber to focus the energies of a high explosive. The result is a near idealistic Friedlander pressure form that is purely shock driven.

Though the CVRC lacks certain abilities to cause a shock wave outside of the tube is not to take away from the inside kinematics of how the tube functions. Containing the pressurized air and running the experiments without venting the air through a nozzle could very likely cause traditional shock wave behaviors like a simple shock tube would perform, though this is dependent on the incorporation the piston.

The CVRC Shock tube can also be explored for hypersonic by simple incorporations of converging diverging nozzles at the end in replacement of the blast tube. As typical with a Stalker type shock tube, piston driven shock tubes can be calculated to yield sustained high-pressure loadings similar to that of re-entrant space vehicles. Further work could be implemented to see how particular scaled space materials/geometries would behave in a reentry event. Furthermore, nozzle geometries can be characterized as internal and exit pressures can be taken before and after the nozzle, as well as assess the expansion characteristics outside of the nozzle exit.

From a hybrid material standpoint, implementing a composite material with stronger interlaminar shear strength under the same loading conditions would illustrate the exact role of the composite backing and would be beneficial to compare these findings. Another step into completely understanding the interactions, it would be very contributive to dive further on what contributions the stiffnesses of the two materials have on the material system. Knowing more about how the mechanical properties effect the overall system, it would then be unique to test different matrix systems, i.e. thermoset vs. thermoplastic. From there, more complex material designs could be made in regard to ply angles, woven fabrics, reinforcing fiber compositions, thicknesses and variations could be explored.

APPENDIX

APPENDIX

Table 26 Series Temper Code Designations (HX)

H Series Code	Alloy fabrication
H1	Stain hardened only
H2	Strain hardened and partially annealed
H3	Strain hardened and stabilized
H4	Strain hardened and coated

Table 27 H Series Temper Code Designation (HxX)

H Series Code	Degree of Strain Hardening
HX2	Quarter hard
HX4	Half hard
HX6	Three-quarters hard
HX8	Full hard
HX9	Extra hard

Table 28 T Series Temper Code Designation

T Series Code	Alloy Fabrication
T1	Natural aging after cooling from elevated temperature
T2	Cold worked after cooling after cooling from elevated temperature
T3	Solution heat treated, cold worked and naturally aged
T4	Solution heat treated and naturally aged
T5	Artificially aged after cooling from an elevated temperature shaping process.
T6	Solution heat treated and artificially aged.
T7	Solution heat treated and stabilized (overaged)
T8	Solution heat treated, cold worked and artificially aged.
T9	Solution heat treated, artificially aged and cold worked.
T10	Cold worked after cooling from an elevated temperature shaping process and then artificially aged.

Table 29 Toray TC940 Neat Resin Characteristics [85]

Density	1.3 g/cc
Tensile Strength	79 MPa (11.5.ksi)
Tensile Modulus	0.7 GPa (0.1 Msi)
Elongation at Break	70%
Strain at Yield	15%
UL94 Flammability	HB
Melt Temp	254°C (490°F)
Heat Deflection Temperature	0.46 MPa (66 psi) @ 70°C (158°F)

Table 30 Toray TC940 Manufactured Mechanical Data [85]

Mechanical Properties	**Method**	**Typical Results**	
Tensile Strength 0°	ASTM D 3039	960 MPa	139 ksi
Tensile Modulus 0°	ASTM D 3039	32 GPa	4.6 Msi
Flexural Strength 0°	ASTM D 790	1215 MPa	176 ksi
Flexural Modulus 0°	ASTM D 790	32.2 GPa	4.7 Msi
Compressive Strength 0°	ASTM D 3410	329 MPa	48 ksi
Short Beam Shear ILSS	ASTM D 2344	41 MPa	6 ksi

Table 31 UL94 Horizontal Burn Rating [86]

Test Criteria	Burning Rate In V	Flammability Rating
Thickness 3-13mm	$\leq 40 \frac{mm}{min}$	HB
Thickness > 3mm	$\leq 75 \frac{mm}{min}$	HB
Flame is extinguished before first mark	$= 0 \frac{mm}{min}$	HB

Table 32 MAT_054 Parameter Definitions

Parameter	Meaning	Notes
MID	Material ID	
RO	Density	
EA/EB/EC	Youngs modulus	A,B,C Depict Direction
PRBA/PRCA/PRCB	Poisson's ratio	A,B,C Depict Direction
GAB/GBC/GCA	Shear modulus	A,B,C depict direction
AOPT	Material axes option	Dictates local material coordinate
2WAY	2 way fiber action	Unidirectional/Woven Fabric Behavior
XP/YP/ZP A1/A2/A3 V1/V2/V3 D1/D2/D3	Vectors to assign local material coordinate system	Dependent on selection of AOPT
MANGLE	Material angle	
DFAILM	Max strain for matrix in tension or compression	
DFAIL2	Max shear strain	
TFAIL	Time step criteria for element deletion	
ALPH	Shear stress term for nonlinear	0-0.5, relevance is hard to distinguish
SOFT/SOFTG/SOFT2	Softening reduction factor for material strength in crashfront	
FBRT	Softening for fiber tension	
YCFAC	Reduction factor for compressive fiber strength after matrix failure	
DAILT	Max strain fiber tension	
DFAILC	Max strain fiber compression	
EPS	Effective failure strain	
XC/YC/XT/YT/SC	Stress failure limits (Tensile, Compressive and Shear)	X and Y depict local material direction
BETA	Weighting factor for shear term in tensile fiber mode	0-1, relevance is hard to distinguish
PFL	Percent layers failed before crashfront initiated	
EPSF	Damage initiation shear	
EPSR	Damage failure shear	
TSMD	Transverse shear damage	
SLIMT1/SLIMC1 SLIMT2/SLIMS	Factor minimum stress limit	
NCYRED	Number of cycles for stress reduction	

BIBLIOGRAPHY

BIBLIOGRAPHY

[1] G. Guglielmi, “Why Beirut’s ammonium nitrate blast was so devastating,” *Nature*, 2020.

[2] M. Y. Yahya, W. J. Cantwell, G. S. Langdon, and G. N. Nurick, “The Blast Behavior of Fiber Reinforced Thermoplastic Laminates,” *J. Compos. Mater.*, vol. 42, no. 21, pp. 2275–2297, 2008.

[3] T. P. Vo, Z. W. Guan, W. J. Cantwell, and G. K. Schleyer, “Modelling of the low-impulse blast behaviour of fibre-metal laminates based on different aluminium alloys,” *Compos. Part B Eng.*, vol. 44, no. 1, pp. 141–151, 2013, doi: 10.1016/j.compositesb.2012.06.013.

[4] G. S. Langdon, W. J. Cantwell, and G. N. Nurick, “The blast response of novel thermoplastic-based fibre-metal laminates – some preliminary results and observations,” vol. 65, pp. 861–872, 2005, doi: 10.1016/j.compscitech.2004.09.025.

[5] S. L. Lemanski, G. N. Nurick, G. S. Langdon, and M. C. Simmons, “Behaviour of fibre metal laminates subjected to localised blast loading — Part II : Quantitative analysis,” vol. 34, pp. 1223–1245, 2007, doi: 10.1016/j.ijimpeng.2006.05.009.

[6] R. F. Gibson, *Principles of Composite Material Mechanics*. McGraw-Hill, 1994.

[7] M. Loos, *Carbon Nanotube Reinforced Composites*. William Andrew Applied Science Publishers, 2015.

[8] S. Bard, F. Schönl, M. Demleitner, and V. Altstädt, “Copper and nickel coating of carbon fiber for thermally and electrically conductive fiber reinforced composites,” *Polymers (Basel).*, vol. 11, no. 5, 2019, doi: 10.3390/polym11050823.

[9] J. W. Martin, *Materials for Engineering 3rd Edition*, 3rd ed. Woodhead Publishing, 2006.

[10] C. Kassapoglou, *Design and Analysis of Composite Structures With Applications To Aerospace Structures 2nd Edition*. John Wiley & Sons, 2013.

[11] U. Gedde and M. Hedenqvist, *Fundamental Polymer Science*. Springer, 2019.

[12] M. Biron, *Plastic Design Library: Thermoplastics and Thermoplastic Composites*, 3rd ed. William Andrew Applied Science Publishers, 2018.

[13] F. W. Collins, E. A., Bares, J., Billmeyer, *Expirements in Polymer Science*. John Wiley & Sons, 1973.

[14] G. Groeninckx, G., Berghmans, H., Overbergh, N., Smets, "Crystallization of poly(ethylene terephthalate) induced by inorganic compounds. I. crystallization behavior from the glassy state in a low-temperature region," *J. Polym. Sci.*, vol. 12, pp. 303–316, 1974.

[15] W. Post, A. Susa, R. Blaauw, K. Molenveld, and R. J. I. Knoop, "A Review on the Potential and Limitations of Recyclable Thermosets for Structural Applications," *Polym. Rev.*, vol. 60, no. 2, pp. 359–388, 2020, doi: 10.1080/15583724.2019.1673406.

[16] S. J. Pickering, "Recycling technologies for thermoset composite materials—current status," *Compos. Part A*, vol. 37, no. 8, pp. 1206–1215, 2006.

[17] H. Nishida, V. Carvelli, T. Fujii, and K. Okubo, "Thermoplastic vs. Thermoset Epoxy Carbob Textile Comosites," in *13th International Confrence on Textile Composites*, 2018, p. 406.

[18] G. J. Kaufman, *Introduction to Aluminum Alloys and Tempers*. ASM International, 2000.

[19] J. Weritz, "The Aluminum Association Alloy and Temper System." .

[20] C. A. J. R. Vermeerren, "An Historic Overview of the Development of Fiber Metal Laminates," *Appl. Compos. Mater.*, vol. 10, pp. 189–205, 2003.

[21] J. Sinke, "Manufacturing principles for fiber metal laminates," *ICCM Int. Conf. Compos. Mater.*, 2009.

[22] G. V Reyes and W. J. Cantwell, "The mechanical properties of fibre-metal laminates based on glass fibre reinforced polypropylene," vol. 60, pp. 2–6, 2000.

[23] *Blast Protection of Buildings*, ASCE/SEI 5. American Society of Civil Engineers, 2011.

[24] P. W. Cooper, "Comments on TNT equivalence," *20th Int. Pyrotech. Semin.*, pp. 215–226, 1994.

[25] F. G. FRIEDLANDER, "The diffraction of sound pulses; diffraction by a semi-infinite plane," *Proc. R. Soc. Lond. A. Math. Phys. Sci.*, vol. 186, no. 1006, pp. 322–344, 1946, doi: 10.1098/rspa.1946.0046.

[26] K. Long, "BLAST SIMULATION WITH SHOCK TUBE TESTING AND COMPUTATIONAL FLUID DYNAMICS ANALYSIS," 2008.

[27] R. Gilsanz, R. Hamburger, D. Barker, J. L. Smith, and A. Rahimian, *AISC Design Guide 26. Design of Blast Resistant Structures*. 2013.

[28] J. A. Rodríguez-Martínez, A. Rusinek, and A. Arias, “Thermo-viscoplastic behaviour of 2024-T3 aluminium sheets subjected to low velocity perforation at different temperatures,” *Thin-Walled Struct.*, vol. 49, no. 7, pp. 819–832, 2011, doi: 10.1016/j.tws.2011.02.007.

[29] A. M. Rajendran and J. M. Lee, “Blast Loaded Plates,” *Mar. Struct. Des. Constr. Saf.*, vol. 22, pp. 99–127, 2009.

[30] G. N. Nurick and J. B. Martin, “Deformation of Thin Plates Subjected To Impulsive Loading- A Review Part 2: Expiremental Studies,” *Int. J. Impact Eng.*, vol. 8, no. 2, pp. 171–186, 1989.

[31] *UL Standards: Tests for Flammability of Plastic Materials for Parts in Devices and Appliances*. .

[32] J. L. R. Comtois, M. R. Edwards, and M. C. Oakes, “The Effect of Explosives on Polymer Matrix Composite Laminates,” *Compos. Part A*, vol. 30, no. 3, pp. 181–190, 1999.

[33] A. P. Mouritz, D. S. Saunders, and S. Buckley, “The Damage and Failure of GRP Laminates by Underwater Explosion Shock Loading,” *Composites*, vol. 25, no. 6, pp. 431–437, 1994.

[34] W. Zhang, “Toughening and Failure Mechanism of Composite Materials for Impact and Damage Tolerance,” MIchigan State University, 2015.

[35] S. B. Baştürk and M. Tanoğlu, “Development and mechanical behavior of FML/Aluminium foam sandwiches,” *Appl. Compos. Mater.*, vol. 20, no. 5, pp. 789–802, 2013, doi: 10.1007/s10443-012-9306-3.

[36] X. Liang, Z. Wang, and R. Wang, “Deformation model and performance optimization research of composite blast resistant wall subjected to blast loading,” *J. Loss Prev. Process Ind.*, vol. 49, pp. 326–341, 2017, doi: 10.1016/j.jlp.2017.07.010.

[37] M. Smith *et al.*, “The quasi-static and blast response of steel lattice structures,” *J. Sandw. Struct. Mater.*, vol. 13, no. 4, pp. 479–501, 2011, doi: 10.1177/1099636210388983.

[38] D. N. Zhang, Q. Q. Shangguan, C. J. Xie, and F. Liu, “A modified Johnson-Cook model of dynamic tensile behaviors for 7075-T6 aluminum alloy,” *J. Alloys Compd.*, vol. 619, pp. 186–194, 2015, doi: 10.1016/j.jallcom.2014.09.002.

[39] R. Yamada, S. Ishizawa, G. Itoh, A. Kurumada, and M. Nakai, *Effects of environment on fatigue crack growth behavior of 2000 and 7000 series aluminum alloys*, vol. 3, no. 1. Woodhead Publishing Limited, 2014.

[40] G. FitzGerald, “Corrosion of Aluminium and Its Alloys,” *Anti-Corrosion Methods Mater.*, vol. 6, no. 6, pp. 185–188, 1959, doi: 10.1108/eb019594.

[41] G. S. E. Bikakis, C. D. Dimou, and E. P. Sideridis, “Ballistic impact response of fiber–metal laminates and monolithic metal plates consisting of different aluminum alloys,” *Aerosp. Sci. Technol.*, vol. 69, pp. 201–208, 2017, doi: 10.1016/j.ast.2017.06.028.

[42] G. S. Langdon, S. L. Lemanski, G. N. Nurick, and M. C. Simmons, “Behaviour of fibre – metal laminates subjected to localised blast loading : Part I — Experimental observations,” vol. 34, pp. 1202–1222, 2007, doi: 10.1016/j.ijimpeng.2006.05.008.

[43] D. Schleh, “FRINGE PROJECTION IN THE DYNAMIC TESTING OF COMPOSITE MATERIALS,” Michigan State University, 2013.

[44] S. Avachat and M. Zhou, “High-speed Digital Imaging and Computational Modeling of Hybrid Metal-Composite Plates Subjected to Water-based Impulsive Loading,” *Exp. Mech.*, vol. 56, no. 4, pp. 545–567, 2016, doi: 10.1007/s11340-015-0038-9.

[45] D. Schleh, G. Li, and D. Liu, “Response of Material Under Blast Loading,” vol. 1, pp. 185–190, 2016, doi: 10.1007/978-3-319-22452-7.

[46] G. Li and D. Liu, “Laboratory blast simulator for composite materials characterization,” in *Conference Proceedings of the Society for Experimental Mechanics Series*, 2011, vol. 1, pp. 233–238, doi: 10.1007/978-1-4419-8228-5_32.

[47] P. T. Ngo, P. Mendis, A. Gupta, and J. Ramsay, “Blast Loading and Blast Effects on Structures – An Overview,” *eJSE*, 2007, doi: 10.1016/j.proeng.2017.09.432.

[48] R. Mejia-Alvarez, J. Kerwin, S. Vidhate, P. Sandherr, E. Patton, and D. Bianca, “Large Cross-Section Blast Chamber : Design and Experimental Characterization,” pp. 1–25.

[49] B. E. Milton and R. D. Archer, “Generation of Implosions by Area Change in a Shock tube,” *AIAA J.*, vol. 7, no. 4, pp. 779–780, 1968.

[50] B. E. Milton, “The Focusing of Shock Waves in Two-Dimensional and Axi-symmetric Ducts,” *Int. Work. Shock Wave Focus.*, vol. 5079, no. 6, pp. 63–80, 1989.

[51] G. Li, T. Ukai, and K. Kontis, “Characterization of a novel open-ended shock tube facility based on detonation transmission tubing,” *Aerosp. Sci. Technol.*, vol. 94, p. 105388, 2019, doi: 10.1016/j.ast.2019.105388.

[52] H. D. Kim, Y. H. Kweon, T. Setoguchi, and T. Aoki, “Weak shock reflection from an open end of a tube with a baffle plate,” *Proc. Inst. Mech. Eng. Part C J. Mech. Eng. Sci.*, vol. 217, no. 6, pp. 651–660, 2003, doi: 10.1243/095440603321919572.

[53] B. Medhi, G. M. Hegde, and K. J. Reddy, “Time-resolved quantitative visualization of complex flow field emitted from an open ended shock tube using a wavefront measuring camera,” *Opt. Lasers Eng.*, vol. 122, no. May, pp. 354–360, 2019, doi: 10.1016/j.optlaseng.2019.06.002.

[54] M. Heredia Ortiz and E. A. Patterson, "Location and shape measurement using a portable fringe projection system," *Exp. Mech.*, vol. 45, no. 3, pp. 197–204, 2005, doi: 10.1177/0014485105053801.

[55] E. A. Campo, *Thermal Properties of Polymeric Materials*. William Andrew Applied Science Publishers, 2008.

[56] F. Polymers, "Phosphonates in PET Applications."

[57] G. S. Langdon, Y. Chi, G. N. Nurick, and P. Haupt, "Response of GLARE © panels to blast loading," *Eng. Struct.*, vol. 31, no. 12, pp. 3116–3120, 2009, doi: 10.1016/j.engstruct.2009.07.010.

[58] T. Kotzakolios, D. E. Vlachos, V. Kostopoulos, T. Kotzakolios, D. E. Vlachos, and V. Kostopoulos, "Investigation of blast response of GLARE laminates : comparison against experimental results Investigation of blast response of GLARE laminates : comparison against experimental results," vol. 8011, 2013, doi: 10.1179/1743289810Y.0000000024.

[59] C. Soutis, G. Mohamed, and A. Hodzic, "Modelling the structural response of GLARE panels to blast load," *Compos. Struct.*, vol. 94, no. 1, pp. 267–276, 2011, doi: 10.1016/j.compstruct.2011.06.014.

[60] E. G. Patton, R. J. Hart, and A. Q. Smail, "Manufacturing and Characterization of PET/GF Thermoplastic Composites," 2021.

[61] G. Ghate and S. Saify, "Shock Tube Simulation in LS-DYNA for Material Failure Characterization," 2014, doi: 10.4271/2014-01-0937.Copyright.

[62] N. S. Brar, V. S. Joshi, and B. W. Harris, "Constitutive model constants for Al7075-T651 and Al7075-T6," *AIP Conf. Proc.*, vol. 1195, no. 1, pp. 945–948, 2009, doi: 10.1063/1.3295300.

[63] F.-K. Chang and K.-Y. Chang, "A Progressive Damage Model for Laminated Composites Containing Stress Concentrations," *J. Compos. Mater.*, 1987.

[64] S. W. Tsai and E. M. Wu, "A General Theory of Strength for Anisotropic Materials," *J. Compos. Mater.*, 1971.

[65] LS Dyna, *LS-Dyna Keyword User's Manual Volume 2: Material Models R12*. .

[66] A. Matzenmiller, J. Lubliner, and R. L. Taylor, "A Constitutive Model for Anisotropic Damage in Fiber Composites," *Mech. Mater.*, vol. 20, no. 125–152, 1995.

[67] E. L. Fasanella, K. E. Jackson, J. D. Littell, and M. D. Seal, "Simulating the Impact Response of Full-Scale Composite Airframe Structures," *13th Int. LS-DYNA Users Conf.*, pp. 1–20, 2014.

[68] A. Gulli, A. Ozdemir, and E. Ozdemir, “Experimental Investigation of the Effect of Glass Fibers on the Mechanical Properties of Polypropylene and Polyamide 6 Plastics,” *Mater. Des.*, 2004.

[69] A. Yudhanto *et al.*, “Monotonic and cyclic responses of impact polypropylene and continuous glass fiber-reinforced impact polypropylene composites at different strain rates,” *Polym. Test.*, vol. 51, pp. 93–100, 2016, doi: 10.1016/j.polymertesting.2016.03.008.

[70] P. Ma, L. Jiang, B. Sun, and B. Gu, “Characterization of the tensile behaviour of a co-woven-knitted composite in the continuous and discrete frequency domain,” *Philos. Mag.*, vol. 92, no. 15, pp. 1966–1997, 2012, doi: 10.1080/14786435.2012.657707.

[71] R. Hart, B. Khatib-Shahidi, E. G. Patton, and A. Q. Smail, “Modeling Dynamic Failure of Woven Carbon Fiber Thermoplastic Composites Using Empirical- and Multiscale-Based Material Cards in LS-DYNA MAT054,” *SAE Int. J. Mater. Manuf.*, vol. 13, no. 3, pp. 5–13, 2020, doi: 10.4271/05-13-03-0020.

[72] National Highway Traffic Safety Administration, “High-Performance Computing Studies,” 2017.

[73] G. S. Dhaliwal and G. M. Newaz, “Experimental and numerical investigation of flexural behavior of carbon fiber reinforced aluminum laminates,” *J. Reinf. Plast. Compos.*, vol. 35, no. 12, pp. 945–956, 2016, doi: 10.1177/0731684416632606.

[74] M. Loos, *Carbon Nanotube Reinforced Composites*. William Andrew Applied Science Publishers, 2015.

[75] T. Cetex and T. C. Pet, “Toray Cetex ® TC940 PET,” vol. 44, no. 0, pp. 0–1, 2019, [Online]. Available: www.toraytac.com.

[76] S. Satapathy, “Mechanical Properties of G-10 Glass – Epoxy Composite The University of Texas at Austin Institute for Advanced Technology.”

[77] R.-T. Materials, “End tabbing of composite test specimens – Theory,” 2020. .

[78] ASTM D695, “Standard Test Method for Compressive Properties of Rigid Plastics,” *ASTM Int.*, pp. 1–8, 2010, doi: 10.1520/D0695-15.2.

[79] ASTM C39-03, “Standard Test Method for Compressive Strength of Cylindrical Concrete Specimens,” 2017.

[80] ASTM, “ASTM D3518: Standard Test Method for In-Plane Shear Response of Polymer Matrix Composite Materials by Tensile Test of a 45 ° Laminate,” *Annual Book of ASTM Standards*, vol. 94, no. Reapproved. pp. 1–7, 2007, doi: 10.1520/D3518.

[81] ASTM International, "ASTM D2095 Standard Test Method for Tensile Strength of Adhesives by Means of Bar and Rod," *Current*, vol. 15, no. Reapproved. pp. 1–3, 2002, doi: 10.1520/D2095-96R15.2.

[82] ASTM International, "Standard Test Method for Apparent Shear Strength of Single-Lap-Joint Adhesively Bonded Metal Specimens by Tension Loading," vol. 01, no. 74302, pp. 10–15, 2010, doi: 10.1520/D1002-10R19.1.2.

[83] R. Jensen *et al.*, "Adhesives : Test Method , Group Assignment , and Categorization Guide for High-Loading-Rate Applications," no. June, 2014.

[84] M. O. Bozkurt, L. Parnas, and D. Coker, "Simulation of Drop-Weight Impact Test on Composite Laminates using Finite Element Method," *Procedia Struct. Integr.*, vol. 21, pp. 206–214, 2019, doi: 10.1016/j.prostr.2019.12.103.

[85] "Toray Cetex TC940 PET Product Data Sheet."

[86] Universal Laboratories, "Flammability UL94 HB." https://www.ulttc.com/en/industries/electrical-and-electronic/combustion-fire/flammability/flammability-ul-94-hb.html.